Department of Mechanical Engineering

University of Southampton

The Steady State Characteristics of the Tilting-pad Gas-journal Bearing

by

Geoffrey Pitts

March 1967

Presented for the Degree of Doctor of Philosophy.

Acknowledgements.

The work reported in this thesis, was carried out as part of an S.R.C. research contract placed with the Department of Mechanical Engineering.

The author would like to thank his supervisor, Dr. N. S. Grassam for his continuous encouragement and helpful guidance throughout this work. The author is also indebted to his colleague Mr. A. J. Munday for the many hours spent in discussion, and for his useful criticism of the work.

Appreciation is also due to Mr. A. Baird for his work in constructing the rig, and to Mrs. J. Wells for typing the script, and the mathematical equations.

SUMMARY.

This thesis is concerned with an analytical approximation to the steady-state solution of Reynold's equation, which makes possible the separation of axial and circumferential characteristics existing in the lubricating film of a tilting-pad gas-journal bearing.

An introduction to gas-bearings is followed by a consideration of the particular aspects of the single pad bearing. It is shown how the basic equations of fluid flow may be reduced to Reynold's equation for a compressible lubricant.

At this stage, an analytical approximation to the solution of the equation is developed, leading to expressions for load capacity and pivot position. The validity of the solution is tested against numerical results.

The test-rig constructed for the experiments, is described in detail, and the experimental results of pressure distribution, viscous losses, and pivot stiffness are tabulated and discussed.

Finally, design curves are presented for a 120° pad, in a dimensionless form, which is independent of bearing length; the use of these design curves, for complete bearing assemblies, being illustrated by a set of worked examples.

Index.

Section No.	Title	Page
	Nomenclature	1
1.0	Introduction	4
1.1	Hydrostatic Bearings	5
1.2	Hybrid Bearings	6
1.3	Hydrodynamic Bearings	6
1.4	Squeeze Film Bearings	8
1.5	Tilting Pad Bearings	8
2.0	The Objectives of This Study	11
3.0	Basic Equations of Fluid Flow	12
3.1	Solutions to Reynold's Equation	17
3.2	The Linearised 'ph' Solution	19
4.0	Properties of the Tilting-pad Bearing	21
4.1	Tilting-pad Bearing Solution	22
4.2	Load Capacity and Pivot Location	28
5.0	Validity of the Linearised 'ph' Analysis	34
5.1	The Numerical Solution of Reynold's Equation	35
5.2	Evaluation of B_1	37
6.0	Numerical Study	38
6.1	Finite Difference Solution	38
6.2	The Runge-Kutta Method	39

Section No.	Title	Page
6.3	Numerical Evaluation of the Analysis for the Infinite Pad	40
6.4	Numerical Stability	41
6.5	Construction of Design Curves	43
7.0	Approximations in Linearising	46
7.1	Study of the Group $p_a c_1^2$	46
7.2	The Quantity P_1	47
8.0	Comparison of Theoretical Pressure Profiles	49
9.0	The Test Apparatus	52
9.1	The Experimental Rig	52
9.2	Loading System	53
9.3	The Test Shaft	54
9.4	The Rotor Drive	56
9.5	The Tilting Pads	57
9.6	Pressure Jacking	59
9.7	Measuring Techniques	59
10.0	Accuracy of Displacement Measurements	62
11.0	Actual Pressure Distributions	64
11.1	Experimental Procedure	64
11.2	Experimental Results	65
11.3	Discussion of Results	68

Section No.	Title	Page
12.0	Bearing Losses	73
12.1	Viscous Loss	73
12.2	Experimental Investigation of Viscous Losses	74
12.3	Discussion of Results	78
12.4	Pressure Loss	79
12.5	Radial Position of the Pivot	81
13.0	Pivot Stiffness	83
13.1	Obtaining Values of Stiffness from Design Curves	83
13.2	Experimental Investigation	84
13.3	Discussion of Results	87
14.0	Pitch Stability	91
15.0	Use of Design Curves	93
15.1	Load Capacity when $\Lambda c \rightarrow \infty$	94
15.2	Selection of H_m	94
15.3	Optimum Conditions	95
15.4	Distortion	95
15.5	Examples	96
16.0	Conclusions	109
16.1	Suggestions for further work	111

Section No.	Title	Page
	Appendix (1)	113
	Appendix (2)	115
	Appendix (3)	120
	Appendix (4)	124
	Appendix (5)	126
	Appendix (6)	132
	References	133
	List of Figures	136

Nomenclature.

A – $\frac{R\beta}{c} = 1 - H_m$

B – constant of integration for the infinite bearing

C – constant

F – PH

F_∞ – the value of F for the infinite bearing,

$\bar{F}$ – $\bar{P}H$

H – h/c

H_m – hm/c dimensionless minimum clearance

$\bar{H}$ – defined in section 7.1

I – integral

I_Y – integral due to end flow correction

K – constant of separation

K_1 – defined by equation (27)

L – bearing length

N – shaft speed (r.p.m.)

N_1 – shaft speed (r.p.s.)

P – dimensionless gauge pressure

P_1 – $\bar{P}_1 - 1$

P_∞ – P for an infinite bearing

$\bar{P}$ – p/p_a dimensionless absolute pressure

$\bar{P}_1$ – p_1/p_a

R – journal radius

U - relative surface velocity

W - applied load

W_1 - component of applied load

W_2 - component of applied load

$\bar{W}$ - dimensionless load, equation (40)

X - dimensionless arc coordinate of pad

X_p - dimensionless pivot position

Y - dimensionless axial coordinate

Z - defined by equation (17)

c - machined in radial clearance

c_1 - mean geometric clearance

f - ph

g - defined in appendix (1)

h - film thickness

h_m - minimum film thickness

k - coefficient defined in equation (45)

n - finite mesh position

p - absolute pressure

p_1 - mean film pressure

p_a - ambient pressure

u -)
) velocities at a point in the fluid film, defined in
v -)
) figure (2)
w -)

x -)
y -) coordinates defined in figure (2)
z -)

β - angle of tilt of the pad about the θ datum

ϕ - position of pad leading edge

Λ - $\dfrac{6\mu\omega R^2}{p_a c_1^{\,2}}$

Λc - $\dfrac{6\mu\omega R^2}{p_a c^2}$

μ - coefficient of viscosity

ρ - density

ψ - position of pad trailing edge

Θ - defined by equation (17)

θ - angular coordinate

θ_1 - angular position of the pivot

$\left[\ \right]_{\phi}^{\psi}$ - limits of integration

1.0. Introduction.

The gas bearing which was once the toy of a few creative researchers, is now taking its place in modern engineering as a practical proposition.

The earliest reported observation of gas as a lubricant, seems to be that made by Hirn[1] in 1854, who remarked that a shaft running in a "dry" bearing appeared to be supported on a fluid film, which he rightly suggested to be air. Kingsbury[2] in 1897 carried out a number of ingenious experiments with a plain journal bearing supporting its own rotor mass. For his studies he evolved a somewhat crude, but very effective system of film thickness measurement.

The years that followed saw a number of isolated attempts to exploit this new found phenomenon, one notable example being its application to spinning machines by Dr. Ferranti[3] in 1904, but this project was abandoned due to other mechanical limitations on the machines. It was not until the widespread development of nuclear power that these bearings became a commercial reality.

It had been found that if oil was used to lubricate the cooling circulators of a reactor, it had to be changed at frequent intervals due to polymerisation. This not only represented a regular maintenance problem, but also one in the disposal of radioactive waste. The major attraction of gas bearings in this particular application, is their ability to use the cooling gas as a

lubricant, linked with the advantages of unlimited life, and their unchanged characteristics over a wide temperature range.

The advantages of long bearing life, made them particularly attractive to the designers of gyroscopes. Previously the wear on ball or roller bearings led to the frequent replacement of those instruments, and to some extent hindered the progress of inertial navigation. Under steady running conditions the life of gas bearings is unlimited, but under practical gyro conditions, it is necessary to stop and start from time to time, resulting in the development of materials with good dry rubbing properties and an ability to maintain a gas film.

Recently they have found uses in many fields of engineering. Their low noise level and high speeds made them ideally suited for use in dental drills, and their operational cleanliness offers an attractive proposition in food processing. The machine tool industry too has found numerous uses for them, such as grinding and drilling spindles, small hand tools, rotating work tables and experimental machine slides to mention but a few.

The various forms of bearing will now be outlined.

1.1. Hydrostatic Bearings.

These bearings rely on the creation of a gas film by some external compressing means, the pressurised gas being fed to the film through small holes in the bearing surface. The viscous or

"creep" flow of the gas from the point of entry to exhaust, maintains a pressure gradient in the film, which in turn enables an applied load to be supported. As the clearance decreases the resistance to flow increases, giving a higher load capacity.

The obvious advantage of this type of bearing is that a load may be supported without relative surface movement. In theory the size of load is only limited by the supply pressure available.

When the efficiency of this bearing, operating at low surface velocities, is compared with simple boundary lubrication, the pumping effort required is generally more than offset by the frictional saving.

1.2. Hybrid Bearings.

When hydrostatic bearings are operating at low clearances and high speeds a substantial hydrodynamic effect can be experienced, which contributes to the load capacity. This bearing is known as a hybrid bearing and is becoming very common in gas-bearing practice.

1.3. Hydrodynamic Bearings.

The hydrodynamic bearing relies on the relative movement of the two bearing surfaces to "drag" gas into the film, and to maintain the film pressure. This is usually achieved by creating a convergent passage in the film, such as that occurring in journal bearings. In the case of a hydrodynamic thrust bearing the two

surfaces may be parallel, and one method of producing the film is to machine spiral grooves in the surface, in such a way that they terminate before reaching the bearing centre. The action of these grooves is to pump the gas radially inwards from the edge.

The bearing is a self-contained unit, and requires no external gas supply. Under starting conditions however, the surfaces rub together, and it is essential to use either low friction materials, or make available some form of external jacking. It is therefore preferable to install them where stopping and starting is at a minimum.

Their greatest manufacturing handicap is the high degree of precision required to achieve a small operating clearance. This is further aggravated by the need for large bearing surfaces if sizeable loads are to be supported. It is often mistakenly implied that gas bearings have better frictional properties than their liquid counterparts, which is not strictly so. Although gas viscosities are lower than those of liquids, it must be remembered that to support the same load, the bearing must either be larger, have a smaller clearance, or operate at a higher speed. Usually, where a frictional saving does occur, it is either because the bearing must operate over a wide range of speeds and at different ambient pressures, gas having the advantage of steady characteristics, or in the case of lightly loaded bearings, where

the liquid theory calls for designs impractically small, the gas bearing theory requires a bearing of a size which can be easily manufactured thus obviating over design.

In hybrid, and particularly in hydrodynamic journal bearings, a phenomenon experienced is whirl instability. Although this condition can be serious, it is now possible to predict whirl onset speeds for a number of bearing geometries, in order that bearings may be designed to operate in a stable region.

1.4. Squeeze Film Bearings.

The squeeze film bearing relies on the high frequency "squeezing" motion of the two bearing surfaces to maintain the gas pressure. One way of creating this mechanism is by feeding a high frequency signal to a bearing manufactured from a piezo-electric crystal. The bearing is probably most suitably applied as a small low friction bearing in scientific instruments.

1.5. Tilting Pad Bearings.

The idea of a tilting pad bearing, using oil as a lubricant, was conceived independently by both Michell and Kingsbury at the turn of the century. Michell who had demonstrated the load carrying advantages of this bearing over the simple viscosity thrust collars, was convinced that similar advantages could be gained in applying the same principle to journal bearings. This is certainly not the case with gas bearings, as the absence of a negative

pressure zone in the bearing, and the ambient pressures existing between pads, can lead to lower capacities than those attained in plain journal bearings. The bearings did however find a use where problems of bearing misalignment occurred, such as in marine propeller shafts, but with the increase in shaft speeds, whirl instabilities became a major problem, and these bearings took on a new rôle as anti-whirl bearings.

It was this anti-whirl property which attracted the designers of gas circulators to apply them in the field of gas lubrication. They had found that when the circulator rotors were supported in plain journal bearings they experienced whirl. As a result, pad bearings were designed on the simplified theory of Snell[5], and a programme of research and development initiated. Moreover hydrodynamic gas bearings have a tendency towards large length to diameter ratios, which present serious alignment problems, giving an added advantage in the use of pad bearings.

The tilting pad bearing consists of a number of curved segments, which maintain the shaft in its running position figure (1). The lubricating film is usually generated by hydrodynamic action between the pads and the shaft, although some attempts have been made at external pressurisation.

As already stated, the pad bearing possesses good anti-whirl properties which the author has previously suggested[4] may be due

to the movement of the pads. Marsh[6] has shown that whirl is a function of bearing geometry, and it is likely that when conditions are such that a pad bearing begins to whirl, the bearing geometry is changed by the movement of the pads, due to the small rotating pressure field. The pads moving in such a manner as to stabilise the running conditions. Although the pad may return to its original position and the whirl recommence, the whirl is never allowed to reach measurable proportions.

The work carried out by Snell, was based on the assumption that the fluid was incompressible; this yields a good approximation to a gas film, when the specific loading on the pad is low, but is in error for heavy loading and high speeds.

Research by the Franklin Institute, was based on the direct numerical solution of Reynold's equation, and is presented in the form of design curves. Unfortunately, the parameters chosen are not truly dimensionless, and a set of curves is required for each length to diameter ratio, for a particular compressibility number, and for every span of pad. Although these curves are very useful for the limited range they cover, they would be expensive to extend in terms of computation time, and in certain regions, numerical instabilities occur.

2.0. The Objectives of This Study.

At the outset, an attempt was made to find an analytical solution to Reynold's equation, so that suitable nondimensional parameters could be selected, to effectively include as many variables as possible. The theoretical and experimental investigations, were then studied in terms of these parameters, with a view to producing comprehensive design curves with a minimum of computation time.

3.0. Basic Equations of Fluid Flow.

In classical fluid dynamics, the fluid is considered to be inviscid, which simplifies considerably the mathematical treatment of the equations of state. Practically however, the regions of greatest interest are those involving large velocity gradients and occurring near solid boundaries. It is these regions which are of direct importance to the understanding of fluid film lubrication.

For a gas, the conditions at any point in it, may be defined by six basic equations, together with certain supplementary ones, such as that relating the coefficient of viscosity to temperature. These equations are: the continuity equation, the three Navier-Stokes momentum equations, the energy equation, and finally in the case of a perfect gas, the gas law. Although a mathematically correct solution could be obtained for conditions existing anywhere in the film, it would be a very laborious process, which in general, is not justified. The usual approach is to simplify the basic equations, by neglecting terms, which in relation to the rest of the equation are small.

To apply the necessary basic equations we must assume that the lubricating film behaves as a Newtonian fluid. Burgdorfer[7] shows that this is a reasonable assumption provided that the separation between the two bounding surfaces is greater than one

hundred times the molecular mean free path of the gas. In general, for lubricating films, this condition is satisfied, but special consideration must be given to certain gases at low pressures, such as helium. For example air at standard conditions, has a mean free path of about 2.7×10^{-6} ins., and helium at 3 Lb/in^2 (absolute) and 32°F, about 36×10^{-6} ins.

A further simplifying assumption is that the viscosity of the gas remains substantially constant. This may be justified since viscosity varies only slightly with the temperature and a number of experimenters have shown the film conditions to be of an isothermal nature, ref. (8).

Applying these assumptions the three time independent Navier-Stokes equations (1) become:-

$$\rho\left(u\frac{\partial u}{\partial x} + v\frac{\partial u}{\partial y} + w\frac{\partial u}{\partial z}\right) = X - \frac{\partial p}{\partial x}$$
$$- \frac{2}{3}\frac{\partial}{\partial x}\left[\mu\left(\frac{\partial u}{\partial x} + \frac{\partial v}{\partial y} + \frac{\partial w}{\partial z}\right)\right] + 2\frac{\partial}{\partial x}\left[\mu\frac{\partial u}{\partial x}\right]$$
$$+ \frac{\partial}{\partial y}\left[\mu\left(\frac{\partial u}{\partial y} + \frac{\partial v}{\partial x}\right)\right] + \frac{\partial}{\partial z}\left[\mu\left(\frac{\partial u}{\partial z} + \frac{\partial w}{\partial x}\right)\right]$$

$$\rho\left(u\frac{\partial v}{\partial x} + v\frac{\partial v}{\partial y} + w\frac{\partial v}{\partial z}\right) = Y - \frac{\partial p}{\partial y}$$
$$- \frac{2}{3}\frac{\partial}{\partial y}\left[\mu\left(\frac{\partial u}{\partial x} + \frac{\partial v}{\partial y} + \frac{\partial w}{\partial z}\right)\right] + 2\frac{\partial}{\partial y}\left[\mu\frac{\partial v}{\partial y}\right]$$
$$+ \frac{\partial}{\partial z}\left[\mu\left(\frac{\partial v}{\partial z} + \frac{\partial w}{\partial y}\right)\right] + \frac{\partial}{\partial x}\left[\mu\left(\frac{\partial v}{\partial x} + \frac{\partial u}{\partial y}\right)\right]$$

$$\rho\left(u\frac{\partial w}{\partial x} + v\frac{\partial w}{\partial y} + w\frac{\partial w}{\partial z}\right) = Z - \frac{\partial p}{\partial z}$$

$$- \frac{2}{3}\frac{\partial}{\partial z}\left[\mu\left(\frac{\partial u}{\partial x} + \frac{\partial v}{\partial y} + \frac{\partial w}{\partial z}\right)\right] + 2\frac{\partial}{\partial z}\left[\mu\frac{\partial w}{\partial z}\right]$$

$$+ \frac{\partial}{\partial x}\left[\mu\left(\frac{\partial w}{\partial x} + \frac{\partial u}{\partial z}\right)\right] + \frac{\partial}{\partial y}\left[\mu\left(\frac{\partial w}{\partial y} + \frac{\partial v}{\partial z}\right)\right]$$

The three quantities X Y and Z are known as body forces, and in the case of a hydrodynamic lubricating film consist of gravity on the film, and any centrifugal components due to film curvature. Clearly the former can be neglected, and a simple calculation will show that centrifugal forces acting on the film are very small compared with the load capacity generated, resulting in these terms being neglected.

The fourth equation required in the lubrication analysis is that for continuity:-

$$\frac{\partial}{\partial x}(\rho u) + \frac{\partial}{\partial y}(\rho v) + \frac{\partial}{\partial z}(\rho w) = 0 \qquad \ldots\ldots(2)$$

Figure (2) shows the coordinate system for a slider moving with velocity U over a plane surface, the lubricating film thickness being h. If h is very small

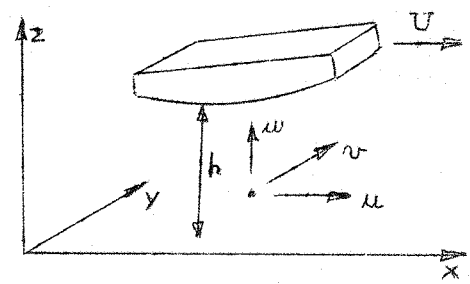

fig (2)

compared with typical distances in the x and y directions of x_o and y_o, and the fluid flow is laminar, then the velocity w is shown by

Curle[9] to be of the order of $u\frac{h}{x_o}$ or $v\frac{h}{y_o}$, and hence may be neglected by comparison with the other velocity components. Furthermore, he has shown that the derivative of any function Φ say with respect to y will be of the order of $\frac{\Phi}{h}$, whereas the derivatives of the same function with respect to y and x, will be of the order of $\frac{\Phi}{y_o}$ and $\frac{\Phi}{x_o}$. These derivatives are much smaller than the y derivative and may be neglected.

The terms on the left hand side of equations (1) are due to gas inertia and have been shown by Brand[10] to be very small within the present operating regime of gas bearings.

Applying the above criteria, equations (1) reduce to:-

$$\frac{\partial p}{\partial x} \simeq \frac{\partial}{\partial z}\left[\mu \frac{\partial u}{\partial z}\right]$$

$$\frac{\partial p}{\partial y} \simeq \frac{\partial}{\partial z}\left[\mu \frac{\partial v}{\partial z}\right] \qquad \text{.....(3)}$$

$$\frac{\partial p}{\partial z} \simeq 0$$

The third of the above equations indicates that across the film, the pressure is substantially constant.

The other two equations may now be integrated with respect to z, the boundary conditions from fig (2) being:-

$u = U$ at $z = h$

$u = 0$ at $z = 0$

$v = 0$ at $z = 0$ and $z = h$

giving:-

$$u = \frac{1}{2\mu}\frac{\partial p}{\partial x} z(z-h) + \frac{z}{h} U \qquad \text{.....(a)}$$

.....(4)

and $$v = \frac{1}{2\mu}\frac{\partial p}{\partial y} z(z-h) \qquad \text{.....(b)}$$

Substituting (4) into (2) and integrating with respect to z between the limits of 0 and h, yields:-

$$\frac{\partial}{\partial x}\left(\rho h^3 \frac{\partial p}{\partial x}\right) + \frac{\partial}{\partial y}\left(\rho h^3 \frac{\partial p}{\partial y}\right) = 6\mu U \frac{\partial}{\partial x}(\rho h) \qquad \text{.....(5)}$$

Since the fluid flow is assumed to be laminar, the mass flow normal to the surfaces, is small compared with that in the other two directions, and the third term in the continuity equation is therefore neglected.

Powell[8] found experimentally that the conditions in the film were approximately isothermal, i.e. ρ is directly proportional to the pressure p. Hence (5) becomes

$$\frac{\partial}{\partial x}\left(ph^3 \frac{\partial p}{\partial x}\right) + \frac{\partial}{\partial y}\left(ph^3 \frac{\partial p}{\partial y}\right) = 6\mu U \frac{\partial}{\partial x}(ph) \qquad \text{.....(6)}$$

The above equation is known as Reynold's equation for a compressible fluid film, and is the basic equation of dynamic gas film lubrication.

3.1. Solutions to Reynold's Equation.

A major obstacle in the solution of (6) is its nonlinearity. Although exact analytical solutions may be found for a few simple geometries, it is in the main, necessary to make certain approximations, or to seek a numerical solution.

The two most common analytical approximations for finite plain journal bearings, are due to J. S. Ausman. In the first[11], the pressure is expressed as a power series of eccentricity, yielding an infinite group of linear differential equations which are more readily solved. A good approximation for small eccentricities may be attained by considering only the first of these linear equations, and is known as the first order pertubation solution. In practical operation however, bearing eccentricities tend to be large, and this technique is now more often employed in the studies of stability criteria, such as those made by Marsh[6]. Ausman then made a further approach to the solution by introducing the product of the pressure and the radial clearance as a variable group[12]. This substitution allows certain approximations to be made in linearising the resulting differential equation. The philosophy behind this method is similar to that for the first order pertubation solution, except that the group 'ph' is used in the series in place of 'p', and is explained fully in reference [13], and its adaptation by the author for use on tilting pad journal bearings will be given in the

following chapters.

Numerical solutions require the construction of a two dimensional mesh system over the bearing surface. A finite difference equation being set up for the pressure at each grid point in terms of the pressure at neighbouring points. The result is a set of simultaneous equations involving 'p' which may be solved between the given boundary conditions.

A particular case of Reynold's equation is that for an infinitely long bearing, where the end flow is zero.

Equation (6) then reduces to :-

$$\frac{\partial}{\partial x}\left(ph^3\frac{\partial p}{\partial x}\right) = 6\mu U\frac{\partial}{\partial x}(ph) \qquad \ldots\ldots\ldots(7)$$

(7) may be integrated with respect to 'x' yielding a first order differential equation:-

$$\frac{dp}{dx} = \frac{6\mu U(ph+B)}{ph^3} \qquad \ldots\ldots\ldots(8)$$

A solution to (8) was given by Katto and Soda[14], but is only applicable to the continuous film of a plain journal bearing, and as a consequence is not suitable for tilting pad analyses.

Equation (8) can also be solved numerically, by using the finite difference technique, but with a unidimensional mesh system, or by using the Runge-Kutta method outlined in this thesis.

3.2. The Linearised 'ph' Solution.

Making the substitution $f = ph$, (6) becomes:-

$$hf\left[\frac{\partial^2 f}{\partial x^2} + \frac{\partial^2 f}{\partial y^2}\right] - f^2\left[\frac{\partial^2 h}{\partial x^2} + \frac{\partial^2 h}{\partial y^2}\right] - 6\mu U\frac{\partial f}{\partial x}$$

$$= f\left[\frac{\partial h}{\partial x}\frac{\partial f}{\partial x} + \frac{\partial h}{\partial y}\frac{\partial f}{\partial y}\right] - h\left[\left(\frac{\partial f}{\partial x}\right)^2 + \left(\frac{\partial f}{\partial y}\right)^2\right] \qquad \ldots\ldots\ldots(9)$$

Ausman shows that as $U \to \infty$ and $U \to 0$ the right hand side of (9) tends to zero. He therefore assumes the right hand side to be everywhere zero. This has been shown experimentally to give a good approximation for plain journal bearings. This, however, must be used with discretion. Contained in this study is a comparison between this method of approach, and a direct numerical one, to establish its validity for pad bearings.

Thus (9) becomes

$$hf\left[\frac{\partial^2 f}{\partial x^2} + \frac{\partial^2 f}{\partial y^2}\right] - 6\mu U\frac{\partial f}{\partial x} = f^2\left[\frac{\partial^2 h}{\partial x^2} + \frac{\partial^2 h}{\partial y^2}\right] \qquad \ldots\ldots\ldots(10)$$

or

$$\frac{\partial^2 f}{\partial x^2} + \frac{\partial^2 f}{\partial y^2} - \frac{6\mu U}{ph^2}\frac{\partial f}{\partial x} = p\left[\frac{\partial^2 h}{\partial x^2} + \frac{\partial^2 h}{\partial y^2}\right]$$

The above equation is still nonlinear, but could be linearised by approximating the coefficient p to some constant p_1, and the

group ph^2 to a constant $p_a c_1^2$.

Ausman assumed that $p_1 = p_a$, which for a plain journal bearing is of similar magnitude to the mean pressure around the bearing, and gives favourable agreement with experimental findings. For a pad bearing however the mean film pressure is above ambient. The value taken for p_1 will be discussed later in this report, (Section 7.2).

Again Ausman assumed that $c_1 = c$, which for a plain journal bearing would be the mean radial clearance, but for a pad, c_1 must be some constant clearance within the film, (Section 7.1).

Applying these approximations

$$\frac{\partial^2 f}{\partial x^2} + \frac{\partial^2 f}{\partial y^2} - \frac{6\mu U}{p_a c_1^2} \frac{\partial f}{\partial x} = p_1 \left(\frac{\partial^2 h}{\partial x^2} + \frac{\partial^2 h}{\partial y^2}\right) \qquad \text{.....(11)}$$

4.0. Properties of the Tilting-pad Bearing.

Before making a mathematical analysis of a tilting pad bearing, it is necessary to have some understanding of the basic requirements.

Probably the most important condition to be satisfied, is that the centre of the fluid film pressure must act through the pivot position. In arriving at the position, it must be borne in mind that the centre of pressure for a curved surface, is not the same as the one for a development of that surface, since we are interested in the chord length rather than the circumferential length.

A source of error in finding the pivot position is the use of approximations to the pressure profile. Although these profiles may have the same integration values as the true distribution, to be a useful representation of the pressure, their centre of pressure must also correspond.

Finite difference solutions require very small mesh sizes when used on pad bearings, otherwise large second derivatives of the pressure profile produce inaccurate results. Ideally one would like a small mesh in the circumferential direction, where these derivatives are likely to be high, and a larger one in the axial direction where they are low, but this can result in a numerical instability reference (15).

The pad bearing differs from the plain journal, in that the boundary conditions for the journal bearing, are ambient at either end, and have a pressure distribution which must be periodic in 2π. The pad bearing although having a repetition of the pressure every 2π, cannot be said to be periodic in 2π, because of the discontinuities existing between the pads. The boundary conditions are therefore taken to be ambient around the edges of the pad. For an analytical solution, this adds a complication since nonperiodic terms in the pressure distribution cannot be neglected, which would have resulted in simplified integration for load capacity.

4.1. Tilting-pad Bearing Solution.

In the case of a pad bearing with the pad parallel to the shaft in the axial direction $\frac{\partial^2 h}{\partial y^2} = 0$

In the circumferential direction from fig (3)

$$h = c - R\beta\sin\theta$$

or nondimensional clearance H is:-

$$H = \frac{h}{c} = 1 - \frac{R\beta}{c}\sin\theta \qquad \ldots\ldots\ldots\ldots(12)$$

Substituting into equation (11), nondimensionalising and changing the coordinate system to that of fig (4) we have:-

$$\frac{\partial^2 \overline{F}}{\partial\theta^2} + \frac{\partial^2 \overline{F}}{\partial Y^2} - \Lambda\frac{\partial \overline{F}}{\partial\theta} = \overline{P}_1 A\sin\theta \qquad \ldots\ldots\ldots\ldots(13)$$

where $A = \frac{R\beta}{c}$ and $\Lambda = \frac{6\mu\omega R^2}{p_a c_1^{\,2}}$

The coordinate system has been selected in order that values may be stated in terms of the nondimensional minimum clearance H_m. A good approximation to H_m is found from fig (4) where:-

$$H_m = 1 - A \qquad \text{.....(14)}$$

$\overline{F}$ in equation (13) is a function of the nondimensional absolute pressure. Therefore the boundary conditions for (13) will be $\overline{F} = H$ along the edges of the pad. If however nondimensional gauge pressure P is used, in place of absolute pressure $\overline{P}$, the boundary conditions become $F = 0$, where $F = PH$, which simplifies the evaluation of the constants in the solution. A further advantage is that P may be integrated directly to obtain the load capacity, without considering the ambient conditions existing on the reverse side of the pad.

Now $\overline{F} = \overline{P}H$

but if we replace $\overline{P}$ by $\overline{P}_a + P$ or $1 + P$ since $\overline{P}_a = 1$ then $\overline{F} = (1 + P)H = F + H$, (13) becomes:-

$$\frac{\partial^2 F}{\partial \theta^2} + \frac{\partial^2 F}{\partial Y^2} - \Lambda \frac{\partial F}{\partial \theta} = A(P_1 \sin\theta - \Lambda\cos\theta) \qquad \text{.....(15)}$$

A particular solution of this equation is that for an infinitely long pad, where $\frac{\partial^2 F}{\partial Y^2} = 0$ and the equation becomes

$$\frac{\partial^2 F}{\partial \theta^2} - \Lambda \frac{\partial F}{\partial \theta} = A(P_1 \sin\theta - \Lambda\cos\theta) \qquad \text{.....(16)}$$

If the solution to (16) is $F = F_\infty$ we may seek a general solution to (15) of the form

$$F = F_\infty + \Theta Z \qquad \text{.....(17)}$$

where Θ is a function of θ only, and Z a function of Y only.

The general solution to (16) is:-

$$F_\infty = \frac{\Lambda}{(1+\Lambda^2)} \{C_1 e^{\Lambda\theta} + C_2 + \Lambda(1+P_1)\cos\theta + (\Lambda^2 - P_1)\sin\theta\} \qquad \text{.....(18)}$$

The boundary conditions for equation (15) are ambient i.e. $P = 0$ at the leading and trailing edges,

or when $\theta = \psi$ $F_\infty = 0$

$\theta = \phi$ $F_\infty = 0$

Hence:-

$$C_1 = \frac{1}{(e^{\Lambda\phi} - e^{\Lambda\psi})} \left[(\Lambda^2 - P_1)\sin\theta + \Lambda(1+P_1)\cos\theta\right]_\phi^\psi \qquad \text{.....(19)}$$

$$C_2 = \frac{1}{(e^{\Lambda\psi} - e^{\Lambda\phi})} \left[e^{\Lambda\phi}\{(\Lambda^2 - P_1)\sin\psi + \Lambda(1+P_1)\cos\psi\} - e^{\Lambda\psi}\{(\Lambda^2 - P_1)\sin\phi + \Lambda(1+P_1)\cos\phi\}\right] \qquad \text{.....(20)}$$

or

$$C_2 = \frac{e^{\Lambda(\phi+\psi)}}{(e^{\Lambda\psi} - e^{\Lambda\phi})} \left[\frac{\Lambda(1+P_1)\cos\theta + (\Lambda^2 - P_1)\sin\theta}{e^{\Lambda\theta}}\right]_\phi^\psi$$

Equation (18) gives the value of F for the infinite bearing, and the pressure profile may be found from

$$P_\infty = \frac{F_\infty}{H} \qquad \text{.....(21)}$$

In the case where P_1 is assumed to be ambient ref (16), then P_1 simply becomes zero in the above equations.

Substituting (17) into (15) and eliminating F_∞ by subtracting (16) we have:-

$$\Theta''Z + \Theta Z'' - \Lambda\Theta'Z = 0 \qquad \text{.....(22)}$$

Rearranging

$$-\frac{Z''}{Z} = \frac{\Theta''}{\Theta} - \Lambda\frac{\Theta'}{\Theta} = -K^2 \quad \text{(say)}$$

Where K is the constant of separation; since Z and Θ are independent of one another K can only be a constant.

Considering Z:-

$$Z'' - K^2Z = 0$$

A solution is:-

$$Z = C_3 \cosh KY \qquad \text{.....(23)}$$

Since ΘZ is in effect a correction to the case of an infinite bearing, we require the maximum correction to the pressure profile at the bearing edge, fig (5); furthermore, Z must be an even function, these conditions are satisfied by solution (23)

Considering Θ:-

$$\Theta'' - \Lambda\Theta' + K^2\Theta = 0 \qquad \text{.....(24)}$$

which has the indicial equation

$$D^2 - \Lambda D + K^2 = 0$$

$$D = \frac{\Lambda \pm \sqrt{\Lambda^2 - 4K^2}}{2} \qquad \ldots\ldots\ldots(25)$$

Again the boundary conditions are ambient at the leading and trailing edges, which are only satisfied if (16) has complex roots. Giving the solution:-

$$\Theta = C_4 e^{\frac{\Lambda}{2}\theta} \sin K_1(\theta - \phi) \qquad \ldots\ldots\ldots(26)$$

$$\text{where} \quad K_1 = \frac{\sqrt{4K^2 - \Lambda^2}}{2} \qquad \ldots\ldots\ldots(27)$$

Once again when $\theta = \phi \quad \Theta = 0$

and $\theta = \psi \quad \Theta = 0$

$$\text{thus} \qquad K_1(\psi - \phi) = n\pi \qquad \ldots\ldots\ldots(28)$$

Considering only the first harmonic:-

$$\Theta = C_4 e^{\frac{\Lambda}{2}\theta} \sin \pi \frac{(\theta - \phi)}{(\psi - \phi)}$$

$$\text{Thus} \quad F = F_\infty + C_5 e^{\frac{\Lambda}{2}\theta} \sin \pi \frac{(\theta - \phi)}{(\psi - \phi)} \cosh KY \qquad \ldots\ldots\ldots(29)$$

From equations (27) and (28)

$$K = \left[\left(\frac{\pi}{\psi - \phi} \right)^2 + \left(\frac{\Lambda}{2} \right)^2 \right]^{\frac{1}{2}} \qquad \ldots\ldots\ldots(30)$$

Originally, the author assumed, (reference 16), that since C_5 is a product of C_3 and C_4, then C_5 could be an arbitrary function of θ; this however contradicts the assumptions used for obtaining equation (17). It is shown in appendix (1), that if C_5 is a constant, then equation (29) is a solution to equation (15). If, however, the assumption is made that C_5 is a function of θ, then it is possible to separate the axial and circumferential flow conditions. A study of this approximation is made in appendix (2). Applying this assumption gives the following:-

$$\text{at } Y = \pm \frac{L}{2R} \quad F = 0$$

Equation (30) becomes:-

$$F = F_\infty \left(1 - \frac{\cosh KY}{\cosh \frac{K}{2}\frac{L}{R}}\right) \qquad \ldots\ldots\ldots\ldots\ldots(31)$$

$$\text{or } P = P_\infty \left(1 - \frac{\cosh KY}{\cosh \frac{K}{2}\frac{L}{R}}\right) \qquad \ldots\ldots\ldots\ldots\ldots(32)$$

Hence the pressure distribution for a finite bearing is given as the product of the pressure for an infinite bearing, and a correction factor in terms of the longitudinal coordinate.

The shape of the correction factor in the axial direction, i.e. a 'cosh' form, satisfies equation (29) and K is defined mathematically by equation (30). Since the axial pressure distribution must be ambient at the pad edges, then the errors may be considered in

terms of the pressure profile at the pad centre, which will be compared with the findings of reference (17) in section (8.0).

4.2. Load Capacity and Pivot Location.

If the pressure forces on the pad are resolved into two components, one parallel to the θ datum and the other perpendicular to it, then after summation, a resultant can be obtained making an angle θ_1 with the datum. The pivot position due to pressure forces, i.e. neglecting pad weight, friction, etc., is thus given by the angle θ_1.

Resolving parallel to the datum:-

$$W_1 = R^2 p_a \int_{-\frac{L}{2R}}^{\frac{L}{2R}} \int_{\phi}^{\psi} P\cos\theta \, d\theta \, dY$$

$$= R^2 p_a \int_{\phi}^{\psi} P_\infty \cos\theta \, d\theta \int_{-\frac{L}{2R}}^{\frac{L}{2R}} \left(1 - \frac{\cosh KY}{\cosh \frac{KL}{2R}}\right) dY \qquad \text{.....(33)}$$

Resolving perpendicular to the datum:-

$$W_2 = R^2 p_a \int_{\phi}^{\psi} P_\infty \sin\theta \, d\theta \int_{-\frac{L}{2R}}^{\frac{L}{2R}} \left(1 - \frac{\cosh KY}{\cosh \frac{KL}{2R}}\right) dY \qquad \text{.....(34)}$$

The integration with respect to Y is:-

$$I_Y = \frac{L}{R} - \frac{2}{K}\tanh\frac{KL}{2R} \qquad \text{.....(35)}$$

I_Y is a factor which takes into account the length of the bearing. Similar end flow factors were determined by Ausman[12] for journal bearings, but are far more complex in form than I_Y.

The pivot position is given by:-

$$\tan\theta_1 = \frac{W_2}{W_1} = \frac{\int_\phi^\psi P_\infty \sin\theta d\theta}{\int_\phi^\psi P_\infty \cos\theta d\theta} \qquad \text{.....(36)}$$

It is interesting to note that with this approximation, the pivot position is independent of bearing length, and can be calculated on the basis of an infinite bearing for simplicity.

Equations (34) and (35) now become:-

$$W_1 = I_Y R^2 p_a \int_\phi^\psi \frac{A}{(1+\Lambda^2)} \{C_1 e^{\Lambda\theta} + C_2 \Lambda(1+P_1)\cos\theta + (\Lambda^2 - P_1)\sin\theta\} \frac{\cos\theta d\theta}{1-A\sin\theta}$$

$$= R^2 p_a A \frac{(I_1 + I_2 + I_3 + (\Lambda^2 - P_1)\, I_4)}{(1+\Lambda^2)}\, I_Y$$

$$= R^2 p_a\, I_a\, I_Y \qquad \text{.....(37)}$$

$$\text{and } W_2 = R^2 p_a A \frac{(I_5 + I_6 + \Lambda(1+P_1)\, I_4 + I_7)}{(1+\Lambda^2)}\, I_Y$$

$$= R^2 p_a\, I_b\, I_Y \qquad \text{.....(38)}$$

The total load W is given by,

$$W = (W_1^2 + W_2^2)^{\frac{1}{2}} \qquad \text{.....(39)}$$

or the nondimensional load $\overline{W}$ by,

$$\overline{W} = \frac{W}{p_a R^2 I_Y} = (I_a^2 + I_b^2)^{\frac{1}{2}} \qquad \text{.....(40)}$$

It is possible to consider three limiting conditions to equation (35):-

(i) $\Lambda \to \infty$, then $I_Y \to {}^{L}/_{R}$.

This means that the load capacity of the pad is directly proportional to the bearing length, a condition which is only satisfied if there is no pressure gradient in the axial direction, figure (5). $\overline{W}$ then becomes a dimensionless load per unit length of the pad.

(ii) ${}^{L}/_{R} \to \infty$, then $I_Y \to \infty$

Again there is no pressure gradient in the axial direction; and $\overline{W}$ is in effect the nondimensional load per unit length, but since ${}^{L}/_{R}$ is infinite, W is also infinite.

(iii) ${}^{L}/_{R} \to 0$ then $I_Y \to 0$

As may be expected a pad of zero length produces zero load capacity. It should be noted however, that $\overline{W}$ may still have a positive value other than zero.

As already indicated in section (4.0) the solution for a plain journal bearing contains only periodic terms, whereas the solution

to a pad bearing may also have nonperiodic ones. In this solution the nonperiodic terms are contained in I_1 and I_5. Although an exact integration is not available for I_1 and I_5, it is possible to make a series expansion of these groups. The approximation made here, is a binomial expansion of the denominator, which was selected in preference to a power series, since it remains reasonably accurate when θ becomes very large. The number of terms has been taken such that the integration may be valid down to values of $H_m = .2$.

Hence:-

$$I_1 \simeq C_1 \left[e^{\Lambda\theta} \left\{ \frac{A_1}{\Lambda^2+1} (\Lambda\cos\theta+\sin\theta) + \frac{A_2}{\Lambda^2+4} (\Lambda\sin2\theta-2\cos2\theta) - \frac{\Lambda_3}{\Lambda^2+9} (\Lambda\cos3\theta+3\sin3\theta) - \frac{A_4}{\Lambda^2+16} (\Lambda\sin4\theta-4\cos4\theta) + \frac{A_5}{\Lambda^2+25} (\Lambda\cos5\theta+5\sin5\theta) \right\} \right]_{\phi}^{\psi}$$

$$A_1 = 1 + \frac{A^2}{4} + \frac{\Lambda^4}{8} \qquad A_2 = \frac{A}{2} + \frac{\Lambda^3}{4}$$

$$A_3 = \frac{\Lambda^2}{4} + \frac{3\Lambda^4}{16} \qquad A_4 = \frac{\Lambda^3}{8}$$

$$A_5 = \frac{\Lambda^4}{16}$$

$$I_2 = \frac{-C_2}{A} \left[\log(1-A\sin\theta) \right]_{\phi}^{\psi}$$

$$I_3 = \frac{-\Lambda(1+P_1)}{A^2}\left[2(1-A^2)^{\frac{1}{2}}\tan^{-1}\left(\frac{\tan\frac{\theta}{2}-A}{(1-A^2)^{\frac{1}{2}}}\right) + A\cos\theta-\theta\right]_{\phi}^{\psi}$$

$$I_4 = \frac{-1}{A^2}\left[A\sin\theta+\log(1-A\sin\theta)\right]_{\phi}^{\psi}$$

$$I_5 \simeq C_1\left[e^{\Lambda\theta}\{\frac{A_6}{\Lambda} + \frac{A_7}{\Lambda^2+1}(\Lambda\sin\theta-\cos\theta)\right.$$

$$- \frac{A_8}{\Lambda^2+4}(\Lambda\cos2\theta+2\sin2\theta) - \frac{A_9}{\Lambda^2+9}(\Lambda\sin3\theta-3\cos3\theta)$$

$$+ \frac{A_{10}}{\Lambda^2+16}(\Lambda\cos4\theta+4\sin4\theta) + \frac{A_{11}}{\Lambda^2+25}(\Lambda\sin5\theta-5\cos5\theta)$$

$$\left.- \frac{A_{12}}{\Lambda^2+36}(\Lambda\cos6\theta+6\sin6\theta) - \frac{A_{13}}{\Lambda^2+49}(\Lambda\sin7\theta-7\cos7\theta)\}\right]_{\phi}^{\psi}$$

$$A_6 = \frac{A}{2} + \frac{3A^3}{8} + \frac{5A^5}{16} \qquad A_7 = 1 + \frac{3\Lambda^2}{4} + \frac{5A^4}{8} + \frac{35A^6}{64}$$

$$A_8 = \frac{A}{2} + \frac{A^3}{2} + \frac{15A^5}{32} \qquad A_9 = \frac{\Lambda^2}{4} + \frac{5\Lambda^4}{16} + \frac{21\Lambda^6}{64}$$

$$A_{10} = \frac{\Lambda^3}{8} + \frac{3\Lambda^5}{16} \qquad A_{11} = \frac{A^4}{16} + \frac{7\Lambda^6}{64}$$

$$A_{12} = \frac{A^5}{32} \qquad A_{13} = \frac{\Lambda^6}{64}$$

$$I_6 = \frac{C_2}{A}\left[\frac{2}{(1-A^2)^{\frac{1}{2}}}\tan^{-1}\left(\frac{\tan\frac{\theta}{2}-A}{(1-A^2)^{\frac{1}{2}}}\right) - \theta\right]_{\phi}^{\psi}$$

$$I_7 = \frac{(A^2-P_1)}{A^2}\left[\frac{2}{(1-A^2)^{\frac{1}{2}}}\tan^{-1}\left(\frac{\tan\frac{\theta}{2}-A}{(1-A^2)^{\frac{1}{2}}}\right) + A\cos\theta-\theta\right]_{\phi}^{\psi}$$

The methods for obtaining some of the above integrated groups are not altogether obvious. For this reason the detailed integration is given in appendix (3).

5.0. Validity of the linearised 'ph' Analysis.

This analysis may be examined in two stages. Initially it must be established that Reynold's equation gives a true representation of conditions existing in the gas film, and secondly the approximations made in its solution should be justified.

It is more convenient to study the solution of the equation first, and then to compare theoretical and experimental values in order to assess its utility.

It is important, when carrying out such an assessment, that the theoretical and physical properties are compared at the earliest possible stage in the analysis, which for lubricating films requires the comparison of predicted, and actual pressure profiles. To compare load capacities, would lead to the possibility of discrepancies being disguised by the process of integration.

Accurate solutions may be obtained by numerical means, the accuracy depending on the time and computational facilities available. These solutions may then be employed as 'mathematical standards' for purposes of comparison.

Although it is possible to obtain solutions numerically for finite bearings, it is less demanding on computation time to deal with the infinite cases. The approximations however, must then be studied to determine the part played by end flow in their modification.

Equation (9) is symmetrical in x and y, except for the term in U. If the approximations made in obtaining equation (10) from equation (9) are legitimate, then all the terms on the right hand side of (9) must be small compared with those on the left. When the legitimacy is only tested for an infinite bearing, it might be argued that the term in U is 'weighting' the left hand side, and the other terms in x are of the same order as those on the right, this would mean that although the approximation was valid for the x direction it may be invalid for y, since y has no 'weighting' term.

This condition cannot occur, for in order to maintain the equality of the equation, either one or more of the terms on the right, or the remaining terms on the left must be of the same order as the term in U. Therefore to show that the approximation is good for an infinite bearing, would be to show that all the terms on the right are small, and that the same order of validity exists for a finite bearing.

For this reason the numerical solutions discussed in the following chapters will be limited to those for infinite pads, with the exception of existing solutions obtained by The Franklin Institute reference (17).

5.1. The Numerical Solution of Reynold's Equation.

From section (3.1), equation (8), we have Reynold's equation for an infinite bearing:-

$$\frac{dp}{dx} = \frac{6\mu U(ph+B)}{ph^3} \qquad \text{.....(8)}$$

nondimensionalising:-

$$\frac{d\bar{P}}{d\theta} = \frac{\Lambda c(\bar{P}H+B_1)}{\bar{P}H^3} \qquad \text{.....(41)}$$

where $\Lambda c = \dfrac{6\mu\omega R^2}{p_a c^2}$

or

$$\frac{d\bar{P}}{d\theta} = \frac{\Lambda c(\bar{P}(1-A\sin\theta)+B_1)}{\bar{P}(1-A\sin\theta)^3} \qquad \text{.....(42)}$$

The above equation contains $\bar{P}$, the absolute nondimensional pressure. In most calculations concerning pad bearings, $\bar{P}$ will take on values between 1 and 2. When these values are stored in the computer, they are handled in floating point form. If gauge pressure is again substituted for absolute pressure, the values between 1 and 2 have one less digit to be stored, and between 1 and 1.1, two less digits, etc. The result is a reduction in rounding errors when small mesh sizes are employed. (42) then becomes:-

$$\frac{dP}{d\theta} = \frac{\Lambda c((P+1)(1-A\sin\theta)+B_1)}{(P+1)(1-A\sin\theta)^3} \qquad \text{.....(43)}$$

Equation (43) requires two boundary conditions for its complete solution. These are given by the ambient conditions at either end of the pad, i.e.

when $\theta = \phi$ and ψ $\quad P = 0$

One boundary condition provides a starting value for the numerical integration, while the other determines the value of B_1.

5.2. Evaluation of B_1.

Unfortunately, B_1 can only be found by satisfying the boundary conditions after integrating (43), which for a step by step process involves trial values for B_1.

Returning to equation (41), and considering the point at which the pressure is a maximum, i.e.

$$\frac{d\bar{P}}{d\theta} = 0, \text{ then:-}$$

$$\bar{P}H = -B_1$$

Since $\bar{P}$ and H must always be positive, B_1 must take on negative values. By similar reasoning, it can be shown that when integrating in the positive direction, a reduction in B_1 causes a positive reduction in the value of P at the trailing edge of the pad.

A flow diagram of this iteration is shown in figure (6).

A condition which must be borne in mind, is that in practice P cannot take a value of less than -1, which corresponds to absolute vacuum. It was found that if this limit was exceeded during the integration process, the remainder of the process became unstable, it was therefore necessary when this did occur to increase B_1 immediately, and to recommence the integration.

6.0. Numerical Study.

6.1. Finite Difference Solution.

If equation (43) is written in a backward difference form, with an interval Δ_θ and a pivotal point (θ_n, P_n), it becomes:-

$$\frac{P_{n+1} - P_n}{\Delta_\theta} = \frac{\Lambda c((P_n+1)(1-A\sin\theta_n)+B_1)}{(P_n+1)(1-A\sin\theta_n)^3}$$

or

$$P_{n+1} = \frac{\Delta_\theta \Lambda c((P_n+1)(1-A\sin\theta_n)+B_1)}{(P_n+1)(1-A\sin\theta_n)^3} + P_n \qquad \ldots\ldots\ldots(44)$$

The above expression may be handled in one of two ways. A set of simultaneous equations can be set up in P_n and B_1, and solved by matrix methods, or a step by step method may be employed. The step by step method was favoured in this instance, since the computation was performed on a multiprogramming machine, where it is better to sacrifice time in preference to storage space.

The finite difference solution assumes that the curve between two adjacent mesh points is in fact straight. The accuracy of the solution is therefore improved by a reduction in mesh size, which is assisted by the use of dimensionless gauge pressure as already outlined. The importance of a small mesh size becomes marked when the compressibility number is high, not only because of accuracy, but also to maintain a convergence for B_1.

6.2. The Runge-Kutta Method.

Unlike the finite difference solution, the Runge-Kutta method assumes an approximation to the curve between mesh points, and as a result can attain the same accuracy with far fewer points. There is however a stability limitation on the minimum number of points chosen.

The Runge-Kutta method can take many forms, but in this thesis is restricted to what is known as the classical form, reference (18). We then have:-

$$\bar{P}_{n+1} = \bar{P}_n + \frac{\Delta_\theta \Lambda c}{6} (k_0 + 2k_1 + 2k_2 + k_3) \qquad \ldots\ldots\ldots(45)$$

where

$$k_0 = \frac{\bar{P}_n(1-A\sin\theta_n)+B_1}{\bar{P}_n(1-A\sin\theta_n)^3}$$

$$k_1 = \frac{(\bar{P}_n+\tfrac{1}{2}k_0)(1-A\sin(\theta_n+\tfrac{1}{2}\Delta_\theta))+B_1}{(\bar{P}_n+\tfrac{1}{2}k_0)(1-A\sin(\theta_n+\tfrac{1}{2}\Delta_\theta))^3}$$

$$k_2 = \frac{(\bar{P}_n+\tfrac{1}{2}k_1)(1-A\sin(\theta_n+\tfrac{1}{2}\Delta_\theta))+B_1}{(\bar{P}_n+\tfrac{1}{2}k_1)(1-A\sin(\theta_n+\tfrac{1}{2}\Delta_\theta))^3}$$

and $$k_3 = \frac{(\bar{P}_n+k_2)(1-A\sin(\theta_n+\Delta_\theta))+B_1}{(\bar{P}_n+k_2)(1-A\sin(\theta_n+\Delta_\theta))^3}$$

The calculations for each iteration using the Runge-Kutta method, take about four times as long as those using the finite

difference solution. Thus it is necessary for the Runge-Kutta method to attain a greater accuracy when using a quarter of the mesh points to make it worthwhile.

6.3. Numerical Evaluation of the Analysis for the Infinite Pad.

The analytical solution of the film pressure profile is given by equations 18, 19, 20 and 21. These equations contain the parameter:-

$$\Lambda = \frac{6\mu\omega R^2}{p_a c_1^{\,2}}$$

The value of c_1 was taken by Ausman (12), for a plain journal bearing, to be the radial clearance between the journal and the bearing. For that particular case, it was in fact, also the mean film thickness. In this study, the value of c_1 has been taken as the mean geometric clearance under the pad, which is :-

$$c_1 \simeq c\{1 + \frac{\Lambda(\cos\psi - \cos\phi)}{(\psi - \phi)}\} \qquad \ldots\ldots\ldots(46)$$

The validity of c_1 will be considered in a later chapter.

The relationship between Λ and Λc is then given by:-

$$\frac{\Lambda}{\Lambda c} = \left(\frac{c}{c_1}\right)^2 \qquad \ldots\ldots\ldots(47)$$

This relationship has been used in determining the analytical pressure profile for various values of Λ.

The actual calculation of the analytical pressure profiles, has been approached in two ways. The simpler involves assuming the value of p_1 to be ambient, i.e. $P_1 = 0$, and results in the direct evaluation of equation (18). In the alternative method, P_1 is taken to be a mean value of P along the film, and is arrived at by taking a starting value of $P_1 = 0$ and iterating until the variations in P_1 are negligible. This is a very rapidly convergent process.

The two methods are compared in section (8.0).

6.4. Numerical Stability.

It has often been noted, that when solutions are being sought for Reynold's equation at high values of Λc, numerical instabilities may occur. Solutions for an infinite pad bearing are no exception.

The instability stems from the relationship between B_1 and the pressure profile. As the compressibility number increases beyond a certain range, very small variations in B_1 cause large variations in the computed pressure distribution. This is best illustrated by the example shown in figure (7) and the following table:

$\Lambda c = 15$ $\phi = -30^{\circ}$ $\psi - \phi = 120^{\circ}$ $A = .5$ mesh = 50.	
$-B_1$	P at $\theta = \psi$
0	63.5625
1	56.2504
1.125	53.9647
1.1875	50.7278
1.195312	49.2447
1.199218	47.3882
1.205078	43.4153
1.205322	39.7655
1.205353	37.9099
1.2053683	35.5664
1.2053759	30.9391
1.2053769	28.0581
1.2053774	15.0112

The starting value for B_1 in the iteration is zero. When the integration is commenced from the leading edge, a pressure of 63 atmospheres results at the trailing one. As the value of B_1 is reduced to some amount a little less than -1.2, the calculated trailing edge pressure begins to fall towards ambient, and would indeed fall to ambient if the computer were infinitely accurate. Unfortunately the variations in successive values of B_1 become so

small, that they are lost in the computer's rounding error. This condition is further aggravated when a two dimensional mesh system is employed, and has in the past limited solutions to those for small compressibility numbers.

It was found in practice that for a value of $\Lambda = .5$, and $\phi = -30$, the stability limit on a 120° bearing using a finite difference solution was $\Lambda_c = 10$, and using the Runge-Kutta solution $\Lambda_c = 6$. For this reason, a counter was incorporated in the programme to limit the number of iterations should instability occur.

Although the Runge-Kutta method produced fast and accurate solutions at low compressibility numbers, it was abandoned in favour of the finite difference method, because of its unstable behaviour when Λ_c was high.

6.5. Construction of Design Curves.

The analytical approximation for end flow correction shows that to design a single pad, two forms of design curve are required if the parameters are to be truly dimensionless.

One form is shown in figures (8) to (12), and represents the dimensionless load capacity per unit length of an infinitely long bearing, plotted against the dimensionless pivot position. The other set of curves, allows correction due to end flow to be made, and takes account of bearing length.

It should be noted that in the first set, parameters are

plotted for lines of constant Λc, whereas in the second set, they are given for values of constant Λ. Equations (46) and (47) are therefore used for conversion.

The nondimensional load $\bar{W}$, may be calculated using equations (36) to (40) or computed using Simpson's rule from the components of the elemental pressure forces obtained by the finite difference solution. The former method may take two forms, either, that where P_1 is set equal to zero, or that where P_1 is taken to be the mean pressure. It will be seen later that the latter produces the more accurate solution.

In the second form of curve, I_Y is plotted directly from equations (30) and (35).

Curves of $\bar{W}$ against X_p are plotted here for particular values of A (i.e. A = 1-Hm), this is contrary to reference (19) where similar, but not truly dimensionless curves, are plotted for particular values of Λc. It seemed preferable in this case to present Λc in an infinitely variable form, since it is dependent on both machined-in clearance and speed, whereas A is only related to the nondimensional minimum clearance, which for design purposes can be increased in steps of 0.1.

Figure (13) shows a comparison between design curves of $\bar{W}$ against X_p obtained by the analytical method, (solid line), and the finite difference method, (broken line). The points marked on

the numerical curves represent their intersection with lines of constant ϕ.

At high Λc, good agreement is obtained between the two solutions, this is an important point, since it is in this region that numerical solutions become unstable, or are slow to converge, and for this reason, the analytical solution is most useful. At first sight, the difference between the curves at low compressibility numbers appears to be great, but in fact when it is considered that X_p is plotted on an expanded scale, it can be seen that the maximum deviation on the $\Lambda c = .6$ curve is $X_p = .613 - .568$, i.e. less than 5% of the pad length.

In practice, the design curves are not likely to be used at the maxima for $\bar{W}$ for fear of slight variations in running conditions causing a rapid fall-off in load capacity, but would be used for pivot positions nearer the leading edge. For this reason, it is important to plot load capacity accurately, rather than the pivot position at capacity fall-off.

As is shown later, the comparison of theoretical pressure profiles indicates that the analytical solution for $\bar{W}$, tends to slightly over-estimate the load capacity of the pad; it has been decided that where a deviation between the two solutions does occur, the numerical solution will be used, resulting in curves being constructed from the numerical solution at low Λc, and the analytical solution at high Λc.

7.0. Approximations in Linearising.

7.1. Study of the Group $p_a c_1^2$.

This group was substituted in place of ph^2 to obtain the linear equation (11). Its value affects the relationship between Λ and Λc as given by equation (47).

The substitution assumed by Ausman, for plain journal bearings, of $ph^2 \simeq p_a c^2$ was to good effect, for in Journal bearings, "c" is also the mean radial clearance, and p_a approximates to the mean pressure in the bearing.

For a pad bearing, it is a simple task to calculate the mean geometric clearance between the pad and the shaft, but the mean pressure calculation is more complex.

The method adopted in this report was to take $ph^2 \simeq p_a c_1^2$, where c_1 is the mean nondimensional radial clearance.

If the linearisation is sound, equation (10) is valid for all points over the pad surface, and for any given position a definite value for ph^2 exists. If it is assumed that the mean value of ph^2 over the film gives the best conversion from Λ to Λc, then a comparison can be made between it, and the quantity $p_a c_1^2$.

$$\text{Let } P_a \bar{H} = (PH^2)_{\text{mean}}$$

$$\text{then } \bar{H} = (PH^2)_{\text{mean}}.$$

The ratio $c_1/\bar{H}$ will then give the factor by which c_1 is in disagreement when converting from Λc to Λ. This ratio is plotted from

the finite difference solution to the infinite bearing in figure (14), for a pad with a span of 120° and with $\Lambda = .5$. As can be seen, when $\Lambda c \to 0$ the ratio $\to 1$, and hence gives complete agreement, but when $\Lambda c \to \infty$ the values become asymptotic to values between .79 and .88.

When the conversion is used to determine the end flow correction factor I_Y, it is seen from the inset graph on fig (15) that errors in the determination of Λ, create only small variations in the value of I_Y, and this is most marked for $2 \leq \Lambda \leq 7$.

For example when $\Lambda = 2$, $I_Y = 1.9$, and when $\Lambda = 3$, $I_Y = 2.07$, a difference of less than 10% under the worst condition.

The other conversion of Λc to Λ, is in plotting the analytically derived design curves and pressure profiles. Since the analytical design curves are only plotted for the higher compressibility numbers, they fall in a region where large variations in Λ and Λc have only a small effect on the change in $\bar{W}$. This is further borne out by the good agreement of these curves with the numerical curves in fig (13). The effect of errors in Λ for plotting the pressure profiles can be observed in two ways, one is the scaling effect, and the other the movement of the pressure peak along the pad.

7.2. The Quantity P_1.

From equations (18) to (20) it is seen that P_1 acts as a scaling factor on the trigonometric terms, and as a result, has some effect

on the shape of the pressure distribution as well as its magnitude. Its effect on magnitude will be apparent in the following chapter.

8.0. Comparison of Theoretical Pressure Profiles.

In fig (16) the analytical solution for an infinite bearing, with P_1 taken as the mean pressure around the centre line of the bearing, is plotted against the finite difference solution computed with a mesh size of 100.

The analytical solution tends to predict a pressure distribution greater than that of the numerical one, and a displacement of the distribution towards the leading edge. The effect of this displacement is for the analytical pivot position to be forward of the numerical position.

At high and low compressibility numbers, the pressure amplitudes are in closer agreement; this is in keeping with the limiting conditions given in section (3.2). For high compressibility numbers, both the amplitude and the shape of the curves agree well.

Figure (17) shows the analytical solution with $P_1 = 0$, plotted against the same numerical curves as in the previous figure. It should be noted that the amplitude of the distribution is brought more in line with the numerical curve, when P_1 is taken as the mean, although the direct evaluation of equations (36) to (40) make the solution with $P_1 = 0$ a simpler proposition. The improvement in taking P_1 as the mean, is most marked for $\Lambda c = 1.5$.

Direct numerical solutions for a finite pad with a span of 94.5° were plotted at the Franklin Institute, reference (17).

Pressure distributions taken from this reference, are shown in figures (18) and (19). Figure (18) shows the circumferential plot along the pad centre, the Franklin solution being compared with the infinite finite difference solution, which has been corrected for end flow by equation (32). The curves display good agreement on the amplitudes of the pressure peaks. The Franklin curves however, have their peaks displaced towards the trailing edge. One of the disadvantages in obtaining a numerical solution to the finite pad, is that owing to the limitation on computer time and space, the mesh size must be fairly large, and this displacement of the pressure peak could result from this condition. When the numerical solution is obtained for an infinite bearing, it is possible to take a smaller mesh size without any great demand on computation time. For example if the finite bearing is computed with a mesh size of 20 in either direction, 400 mesh points have to be evaluated, whereas a mesh size of 100 for an infinite bearing produces a fifth of the mesh size in the circumferential direction, and only requires 100 points to be evaluated, with a major increase in accuracy. A further disadvantage with the two dimensional mesh system is that of obtaining a stable convergence in both directions. Figure (19) shows the comparison between the axial pressure plots. Most of the deviation between these curves stems from the differences in the circumferential plots. If the circumferential profiles agreed exactly, then the axial

pressure distributions would be in agreement on the pad centre line, and if this were the case, it can be seen that there would be good agreement for $\Lambda c = 1.5$ and $\Lambda c = 4$, and fair agreement for $\Lambda c = 10$. It should be remembered that as $\Lambda c \to \infty$, the pressure gradient in the axial direction becomes zero, as in the case of an infinite bearing, fig (15). It would appear that the curve of $\Lambda c = 10$ taken from reference (17), does not follow this limiting trend, and since it is at a value of Λc, where accurate numerical solutions to a finite bearing are difficult to obtain, it is not a very reliable standard by which to compare a new solution.

In conclusion, it can be said that by comparing the analytical solution with numerical solutions, a test is being made on the analysis as a mathematical evaluation of Reynold's equation. The findings are that the analysis with P_1 as the mean pressure is an improvement on that of $P_1 = 0$, the analysis becomes very accurate at high compressibility numbers, the pressure amplitudes agree well at low compressibility numbers, and from figure (19), the axial pressure distribution is in good agreement with numerical findings.

9.0. The Test Apparatus.

9.1. The Experimental Rig.

A specially constructed rig was used for the experiments described in the following chapters. A sectioned diagram of this rig is given in figure (20).

It is designed such that it can be operated with any number of pads in position. This allows single pad tests to be made, and minimises both the extent of instrumentation required, and the number of pads it is necessary to manufacture. It is also desirable to have a loading system whereby zero load can be attained, and in which the load is unaffected by gravity forces acting on the pad.

For these reasons, the shaft is maintained vertically by two pressurised air slave bearings, its upper portion protruding with minimum clearance through a hole in the top plate. The protruding length provides the working section. At its lower end, the shaft is supported by a pressurised thrust bearing containing a mercury well, by means of which, a needle extending from the shaft centre, provides an earth contact.

The slave bearings are in turn rigidly fixed to a machined channel section encastré in a concrete block. The block provides a cheap and rigid base structure for the rig, and is isolated from the floor by "Metalastic" antivibration mountings. As can be seen

from the diagram, the block is formed in a 'U' shape, providing a soundproof housing for the turbine, and acts as a safety wall in the event of a shaft failure.

The services to the turbine cavity pass from the rear of the structure, through a four inch diameter tube cast into the block. The tube also becomes an exhaust for the turbine air, and is packed with corrugated paper for silencing. A control panel containing air regulators and pressure gauges, provides a front to the turbine cavity, and convenient regulation of the various compressed air services.

Shaft motion in either of the two slave bearings, may be monitored from the two capacitance transducers, positioned in quadrature at each of the bearings. The running speed is recorded from a "Southern Instruments' electromagnetic pick-up, triggered by two small holes drilled in opposite sides of the shaft to maintain dynamic balance.

9.2, Loading System.

An air lubricated cross-slide, was located on the top plate, to which a circular pad carrying three pivot supports, was attached. This facilitated the mounting of three pads on a common structure, whilst allowing easy access for instrumentation, and being suitable for any extension of the present work to multi-pad systems. The cross-slide provided pivot movement normal to the shaft axis.

It was designed such that loads could be applied by compressed air trapped in the cavity at the forward end of the cross-slide, the air pressure being indicated on a gauge. The slide was calibrated against a dead weight load, when it was in its mid-position, this being determined by a dial gauge.

Unfortunately, the slides were constantly becoming clogged with dirt, and after a while, distortion of the cross slide made it difficult to obtain repeatability of the load calibration due to surface contact occurring.

Since these experiments involve the use of a single pad, it was decided to have a simple dead weight loading system, rather than spend time correcting the slide-way.

The loading was finally achieved by locking the cross-slide in position, and replacing one of the pivot supports by a simple bell-crank lever, with a pivot for the pad at one end, and a weight carrier at the other, (fig (21). This gave a three to one load magnification.

It is likely that with improvement, the cross-slide loading system would provide a valuable means of loading a multi-pad bearing, as the load can be orientated by means of the circular pad support, fig (21).

9.3. The Test Shaft.

Originally, the two inch diameter shaft was made by modifying an old rotor used in tests by the U.K.A.E.A. This had the

advantage of having a hard chrome surface, which reduced the risk of damage in the event of a bearing seizure. As proper grinding facilities were not available in the University workshop, the shaft had to be ground by an industrial concern, and when returned, although round, it was found to have a bent axis.

Owing to the difficulties and delays of having a shaft manufactured in this way, an attempt was made to machine a shaft from mild steel, using laboratory workshop facilities. The use of a mild steel shaft, was made possible by the pressure jacking of the pad during starting, but greater care had to be taken during experiments to avoid surface contact.

The mild steel shaft was first machined to a dimension a few thousandths of an inch in excess of the finished size. The centre portion of the shaft, which had to be knurled, fig (23) was turned to a diameter of 1.9 ins., and the knurl applied. At this stage, internal stresses in the bar could exist, and consequently the shaft had to have cyclic heating in a small furnace. The shaft was then turned between centres, until it was .001 ins., greater than the finished size, thus producing a true axis. In fact, the distortion due to stress relieving was hardly measurable. The final finishing was by honing between centres, and the roundness attained measured by a pneumatic ring gauge, was in the order of .0001". A polish was obtained by the light application of a piece of polishing paper,

whilst the shaft was rotating in the rig. Finally the centre at the lower end of the shaft was drilled and tapped to take a brass earthing needle for immersion in the mercury well.

As a check on the axis of rotation, a .001" capacitance displacement probe was mounted in place of the pivot and showed a peak to peak deviation of .00004" when the shaft was rotated slowly.

The polar moment of inertia of the shaft was calculated assuming a standard density for the mild steel; to verify this value, its weight was also calculated and compared by weighing, leading to an agreement of better than .1%, and giving a value of $I = 1.703 \times 10^{-3}$ slugs ft^2.

9.4. The Rotor Drive.

A number of possible drive systems were considered for the purpose, finally reducing to three probable arrangements.

A steam impulse turbine had the advantages of providing a powerful but compact unit, with very high jet velocities. It presented however, problems of exhausting the steam, and maintaining a thermally stable rig. An electric induction motor was considered, but it was feared that it may have been difficult to balance the rotor at high speeds. On the other hand, balancing a hysteresis motor would have been much simpler, but here there was the danger of heat being generated in the shaft.

An air turbine drive was finally selected, consisting of five

"Laval" nozzles directed onto the knurled surface of the shaft. The knurled shaft form of drive, had previously proved very effective in reducing turbine noise, with little loss in driving power.

In order to manufacture a "Laval" nozzle, it is necessary to create a smooth convergent-divergent bore, otherwise a shock wave may exist near the throat, resulting in an energy loss within the nozzle itself. Under normal machining conditions it is difficult to manufacture small bores to this requirement, and consequently the author decided to adopt the following technique.

A short length of quarter inch diameter smooth bore, hard copper tube, was held between two rollers, and formed along one of its diameters to cause a reduction in flow area. The pipe was then trimmed in such a way, that the divergence continued up to the exit, and the exit shaped to follow the contour of the knurled shaft, fig (26).

9.5. The Tilting Pads.

The pads were made by modifying existing full journal bearings. These bearings came from the remains of rigs used by the U.K.A.E.A. in conjunction with the chrome plated shaft mentioned previously. The exact nature of the material is not known, but it is some form of fairly hard copper alloy. As the mild steel shaft could not be allowed to make moving contact with the pad, the rubbing properties of the pad were unimportant.

Two pads were cut from each bearing, and were machined in such a way as to form a pair of flanges on their rear side to act as stiffeners; this made possible a thinner and lighter pad, without a great loss in rigidity. The pivot positions were formed by 120° conical recesses in which the pivot, having a 90° cone, could be located. Pressure tappings consisted of .013" diameter holes in the pad surface, leading to short lengths of hypodermic tubing cemented into the back face, fig (27).

The required radius for the pad was achieved by lapping. The lap used, was of the helical expanding type, consisting of a tapered mandrel passing through the centre of a cast iron lap, into which was cut a helical slit. The mandrel and lap were first mounted in a lathe, and the pad was slowly traversed by hand along the lap, whilst the machine was in motion. Once the condition had been reached, where all the pad surface was in contact with the lap, the lap was removed from the lathe, and supported between a pair of "dead" centres, to obtain a final finish by hand lapping. During the lapping operations, the lap had to be constantly "dressed" to avoid it "necking" at its centre, where most of the wear took place. The lapping medium was diamond paste, of which two grades were used, one for roughing, and the other for the hand finishing. A particular danger when lapping pads as opposed to full bearings, is the build up of compound at the leading and trailing edges; if allowed to

accumulate, these surfaces will be cut back below the raminder of the pad.

As no roundness measuring equipment, suitable for checking the pads, existed in the laboratory, the pads had to be compared with a standard cylinder. For this purpose, some accurately manufactured rotors, used on another rig, were employed. These rotors were inspected and sized, using a pneumatic ring gauge.

The method of checking, consisted of smearing the surface of the cylinder with a thin layer of engineers blue, and rubbing the pad against it. This technique was found to be most satisfactory, because when blue appeared all over the pad surface, it was found that after cleaning these surfaces, the pad and cylinder could be easily wrung together, suggesting that the limitation on accuracy was set by the pneumatic gauging, which was better than .0001 ins.

9.6. Pressure Jacking.

For starting purposes, jacking gas was applied to the pad through the pressure tapping holes, this allowed starting to take place without causing surface contact. A diagram of the layout of this system is shown in fig (28). Once the journal had reached a load bearing speed, the jacking gas was clamped off.

9.7. Measuring Techniques.

The pressure distribution was recorded on a mercury manometer, connected to a 'Dralim" channel selection valve. Since only six

channels could be selected with a single valve, a total of three valves was used, and by interconnecting, made available sixteen possible tapping points. In order to put the minimum of constraint on the pad, the pressure tappings were joined to the selectors by small bore plastic tube, as used for electrical insulation.

Displacement was measured by capacitance transducers of the "Wayne Kerr" type, ref (20). This form of capacitance transducer, has the advantage of producing a voltage signal, which is linear with displacement. The capacitance probes themselves, were specially made for the experiments, since the standard manufactured probe is bulky and heavy. The probes consisted of a central electrode, around which a guard ring of minimum thickness was constructed, the fabrication was then shielded by "Tufnol", to insulate it from the pad. A photograph of the probe is shown in fig (25). Very small diameter co-axial cable was soldered to the electrode and guard ring, so that little force was applied to the pad. Unfortunately, the small diameter cable had a very high capacitance, and only a short length could be used, before a joint with a larger cable had to be made. Experience had shown that if the probe and cable capacitance exceeded 130 p.f., a nonlinear signal was produced by the meter. These capacitance probes were fitted at the four corners of the pad, but in a part of the pad outside the bearing surface. The displacement calibration was

made against a barrel micrometer, which was only rotated in one direction to obviate "back-lash". The calibrations are given below, and a typical calibration curve is plotted in fig (29).

Maximum nominal displacement = .002", number of unit divisions on meter = 10.	
Probe	Meter divisions/inch displacement
1	5.45×10^3
2	5.13×10^3
3	5.34×10^3
4	5.56×10^3

Speed was recorded by a digital counter triggered from a "Southern Instruments" tachometer. The original signal being taken from a magnetic pick-up near the two holes on the shaft surface. This made possible a very accurate estimation of the speed, and during run-down tests, could be set to count the period over a given number of cycles, and thus offer a very rapid and accurate method of speed recording, as well as measuring the time interval.

10.0. Accuracy of Displacement Measurements.

The capacitance probes when calibrated with the barrel micrometer, were checked at different positions on the micrometer thread, to average out any local thread imperfections. It was found, however, that the readings taken at different positions, were repeatable. The estimated accuracy as a result, could be put at about 1% of the full scale deflection. Since the probes gave a nominal full scale deflection of .002", it follows that the most pessimistic error in obtaining D_1 and D_2 (appendix 4), occurs when $c = .625 \times 10^{-3}$ ins., and assumes that all the error is in the region of the scale used for the experiments; this gives an error in the order of 3%.

From appendix 4:

$$\phi = \tan^{-1} \left(\frac{D_2B_4 - D_1B_2}{D_1B_1 - D_2B_3}\right)$$

It can be seen that if the quantities D_2B_4 and D_1B_2 or D_1B_1 and D_2B_3 were of the same order, their difference could be composed mainly of the error. In these tests however, the quantities D_2B_4 and D_2B_3 were positive and D_1B_2 and D_1B_1 negative; thus maintaining the order of error to less than 3%.

Again from appendix (4):

$$A = \frac{D_1}{(B_3 \sin\phi + B_4 \cos\phi)}$$

It was found that the experimental values of ϕ were always

negative, which leads to the first term in the denominator being negative, and the second positive. Hence the error in A could be large if both terms were of the same order, and in any case, the 3% error would be increased. Fortunately, for this series of tests, one term was always twice the magnitude of the other, limiting the error in A to less than 6%.

A possible source of error in using displacement probes, is the zero datum setting. Because of the wringing together of the pad and the standard cylinder, no problems were encountered, since the variation in datum reading was very much better than one meter division for all positions on the cylinder. (better than 1% F.S.D)

These displacement measuring techniques, appear to be consistent with obtaining a high degree of experimental accuracy.

11.0. Actual Pressure Distributions.

In keeping with the policy of studying the film pressure distribution, to test the validity of the two solutions obtained to Reynold's equation, a study of the actual pressure profiles in the bearing film were made. The aim was to obtain pressure plots at conditions as widely separated as the rig permitted, in order to test the theory over the greatest possible range.

11.1. Experimental Procedure.

The pressures were recorded at small tapping holes in the pad surface, which have already been described, and were displayed on the mercury manometer. Layouts of the tapping holes for the two conditions tested, are given in fig (30).

For starting, jacking gas was supplied through the pressure tapping holes, and when the rig had reached its load bearing speed, the jacking gas supply was sealed off, and the rig operated hydrodynamically. It was found with the smaller clearance pad, that the trailing edge jacking was too great owing to the concentration of pressure tapping holes in this region; it became apparent when the pad began to pitch during the run-up, and was easily cured by pinching the trailing edge tapping tubes with a small pipe clamp.

During the recording of the distribution, an attempt was made to hold the rig at a constant speed, but at the higher speed, due to the lack of sensitivity in the nozzle regulator, whilst passing

a large volume of air, the speed tended to follow the compressor pressure cycle. This necessitated the recording of the pressure at the instant the cycle passed through the test speed.

The response of the manometer was relatively slow, owing to the small bore of the plastic tube, and the size of the tapping holes. To expedite the recording of the pressures, instead of tappings being selected in geometric order, they were selected by their pressure magnitude, the pressure change between each selected point was thus kept to a minimum, resulting in a shorter settling time for the manometer.

The rig was first operated using a pad with a machined-in radial clearance of $.975 \times 10^{-3}$ ins, giving a compressibility number of 1.232. In order to attain a high compressibility number, it was necessary to both reduce the machined-in clearance, and increase the operating speed to a point near the controllable limit of the rig; this produced a compressibility number of 5.3.

11.2. Experimental Results.

For the above operating conditions, three different loads were applied to the pivot, and the resulting dimensionless pressures were recorded at the tapping points. These pressures are given in tables (1) and (2) and plotted in figures (31) to (33).

TABLE (1)

$\psi - \phi = 120^{\circ}$ $c = .975 \times 10^{-3}$ ins. R = 1 in.

L = 3 ins $X_p = .584$ N = 11,100 r.p.m.

$\Lambda c = 1.232$

			PRESSURE DISTRIBUTION (P)		
			LOADS (LBS)		
TAPPING	X	Y	12.12	15.12	18.12
1	.750	1.25	.104	.131	.154
2	.960	.75	.171	.213	.248
3	.208	.75	.113	.139	.161
4	.960	.20	.193	.240	.277
5	.834	.20	.314	.384	.460
6	.667	.20	.360	.456	.559
7	.375	.20	.213	.260	.308
8	.917	.20	.208	.250	.288
9	.750	.20	.362	.453	.544
10	.584	.20	.330	.420	.507
11	.166	.20	.083	.100	.115
12	.709	.75	.288	.357	.421
13	.917	1.25	.069	.071	.074
14	.250	1.25	1.191	.054	.063
FILM THICKNESS INS $\times 10^{-3}$		LEADING EDGE	1.072	1.124	1.191
		TRAILING EDGE	.424	.475	.532
		A	.567	.535	.521
		ϕ	-25°	-31.8°	-41.6°
		Λ	2.305	1.970	1.65

TABLE (2).

$\psi - \phi = 120^{\circ}$ $c = .625 \times 10^{-3}$ ins. R = 1 in.

L = 3 ins. $X_p = .584$ N = 18,900 r.p.m.

$\Lambda c = 5.3$

TAPPING	X	Y	PRESSURE DISTRIBUTION (P) LOADS (LBS) 15.12	21.12	27.12
1	.750	1.25	.137	.192	.240
2	.960	.75	.103	.151	.199
3	.250	.75	.144	.202	.247
4	.960	.20	.151	.216	.260
5	.835	.20	.363	.514	.637
6	.666	.20	.407	.580	.747
7	.375	.20	.254	.356	.459
8	.920	.20	.254	.350	.445
9	.709	.20	.418	.582	.755
10	.542	.20	.356	.513	.679
11	.167	.20	.116	.151	.185
12	.750	.75	.332	.446	.583
13	.960	1.25	.013	.021	.021
14	.250	1.25	.055	.079	.100
FILM THICKNESS INS $\times 10^{-3}$		LEADING EDGE	1.06	.99	.931
		TRAILING EDGE	.610	.518	.458
		Λ	.635	.565	.523
		ϕ	-99.5	-81	-70.6
		Λ	2.96	3.10	3.40

The theoretical pressure distributions plotted in figures (31) to (33) were computed from the data given at the foot of each table; these values being calculated from the expressions in appendix (4).

11.3. Discussion of Results.

The curves shown in fig (31) for $\Lambda c = 1.232$ give a good correlation between experiment and theory. It should be noted that the analytical solution tends to over-estimate the pressure distribution, but gives a good positioning of the pressure peak, whereas the numerical solution presents a more correct order of magnitude to the profile, but tends to displace it towards the trailing edge.

Fig (32) represents the axial pressure distribution over one half of the pad, and is plotted on the generator $X = .7$. The analytical curves are plotted directly from the pressure distribution obtained by means of the analytical solution, but the "numerical curves" are plotted by obtaining the numerical pressure profile for an infinite pad, and using equation (32) to plot the axial profile, which in fact is making use of the analytical solution.

It can be seen that the "numerical" distributions agree more closely with the experimental points, but this is only so, because at the position where the axial distribution was taken, there is a closer experimental agreement with the "numerical" curves than with the analytical. What is important, is the form of the axial distribution. If a theoretical curve can be constructed to pass

through all the experimental points, then equation (32) is a valid approximation, and only requires an accurate value for P_∞.

Referring back to fig (32), it seems reasonable having regard for the closeness of the numerical curves to the experimental points, that by selecting a suitable value for P_∞, equation (32) could be shown to be almost exact, the greatest error being at the extremities of the pad, where an inflection appears to occur.

Reconsidering the question of design curves, (Section (6.5)), it would appear better, to construct design curves in this region of lower compressibility number, using the numerical method.

The curves of circumferential pressure distribution for $\Lambda c = 5.3$, (fig (33)), show some deviation between experiment and theory. The first point to be considered is that the two theoretical distributions agree well, and therefore the error does not lie in the solution of Reynold's equation. This leaves two main possibilities; one, that the error is to be found in the experimental readings, and the other, that Reynold's equation does not truly represent the conditions existing in the film.

To check out the possibility of experimental errors, the author took further results at both high and low compressibility numbers, and remeasured the pad and shaft dimensions, yielding results consistent with those included in this thesis.

The question of Reynold's equation not truly representing the

conditions in the film, could account for a substantial proportion of the deviation.

The experimental distribution being displaced forward of that predicted by theory, suggests that greater friction exists in the film, than was accounted for in the theory. This would mean that the intake pressure gradient, created by the gas being "dragged" into the film beneath the pad, would be greater, and as a result, the pressure peak would occur nearer the leading edge. On the other hand the viscous flow of gas between the peak pressure position, and the trailing edge, would result in the lower pressure gradient.

The actual viscous loss being greater than the predicted loss, will be verified in the section on bearing friction.

The assumption made in obtaining Reynold's equation for the fluid film under the pad, was that the boundaries were smooth. In practice however, all machined surfaces have a finite roughness. On the author's rig, the problem of surface finish was further aggravated by the use of the mild steel rotor, had facilities been available for the manufacture of a hard steel or chrome rotor, a better finish could have been attained.

From the film shape parameters measured during the experiments, the load capacities and pivot positions were computed from the design curves. These values are compared with the actual values in the following table.

TABLE (3)

ϕ	Λ	$\bar{W}$	COM-PUTED W	ACTUAL W	COM-PUTED X_P	ACTUAL X_P	ERROR IN X_P
-99.5°	.635	.4947	14.85	15.12	.67129	.584	9%
-81°	.565	.6955	21.10	21.12	.67385	.584	9%
-70.6°	.523	.8472	26.51	27.12	.67345	.584	9%

Although the experimental and theoretical profiles are displaced relative to each other, it can be seen that the actual and computed loads correspond well. It is shown however, that the computed pivot position is nearer the trailing edge. If the position of operation on the design curve is not near the point of load fall-off, then as the pivot is moved nearer the trailing edge, the load capacity is increased. It is evident that this is the condition which could result when a single pad arrangement is being designed for high compressibility number operation. The computed pivot position would be "aft" of the actual position to support the load, this would make possible a higher capacity at the clearance, and would suggest that the theory tended to under-estimate the applied load.

Care must therefore be taken, when using design curves at a high compressibility number, to avoid working too near the load fall-off condition, and in the case examined, not within 10% of it.

In general, it appears that good agreement is obtained between experiment and theory at lower compressibility numbers, but at high values of Λc, although there is good agreement on load capacity, some error does occur in calculating the pivot position.

12.0. Bearing Losses.

The estimation of bearing losses in any system, is an important factor in system design. Although it may be impossible to calculate exactly these losses, it is essential to have some idea of their relative magnitude.

12.1. Viscous Loss.

From a theoretical point of view, the viscous loss for a single pad may be treated in one of three ways.

A simple approach, like that of Petroff's for a plain journal bearing, may be used, taking a pad with a concentric clearance equal to the actual mean clearance. With this method, it is first necessary to calculate the mean clearance, and from there it is only a small step to consider the actual form of the film, and to assume a linear velocity profile between the two surfaces, which leads to a solution more in keeping with the physical conditions. The third way involves considering the velocity profile as derived from the Navier-Stokes' equations, equation (4a). Although this is a more desirable form of velocity distribution it is necessary to use numerical integration to determine the torque.

In this study, a linear velocity distribution between the two surfaces has been assumed.

The clearance at any position in the film is:-

$$h = c\left[1-A\sin\theta\right]$$

The viscous shear stress then becomes:

$$\mu \frac{\partial u}{\partial z} = \frac{\mu\omega R}{c[1-A\sin\theta]}$$

From which the torque on the shaft will be:-

$$\frac{2\pi\mu R^3 NL}{c} \int_{\phi}^{\psi} \frac{d\theta}{[1-A\sin\theta]} = \frac{2\pi\mu R^3 NL}{c} \left[\frac{2}{(1-A^2)^{\frac{1}{2}}} \tan^{-1} \frac{(\tan\frac{\theta}{2}-A)}{(1-A^2)^{\frac{1}{2}}} \right]_{\phi}^{\psi}$$

and the corresponding horsepower loss:-

$$HP = \frac{4\pi^2 N_1{}^2 \mu R^3 L}{550c} \left[\frac{2}{(1-A^2)^{\frac{1}{2}}} \tan^{-1} \frac{(\tan\frac{\theta}{2}-A)}{(1-A^2)^{\frac{1}{2}}} \right]_{\phi}^{\psi} \qquad \text{.....(48)}$$

Where 'N_1' is the shaft speed in cycles per second.

12.2. Experimental Investigation of Viscous Losses.

The rig design is particularly suited to determining the loss by viscous retardation of the shaft.

It was first necessary to carry out a run-down test, with the pad operating hydrodynamically against the shaft, and to measure the retardation at various speeds. The run-down had then to be repeated without the viscous drag of the pad, but with the same conditions as before prevailing in the slave bearings, the drag from the pad being the difference between these two cases.

When the loaded pad is operating against the working section, some degree of deflection is to be expected at the slave bearings.

If the pad is completely removed from the working section, the slave bearings will operate in an unloaded condition, producing a change in their frictional characteristics. For this reason it was decided to leave the loaded pad in position, and to apply jacking gas via the pressure tapping holes, to lift it as far clear of the shaft as possible.

This situation was complicated by more jacking gas escaping from one end of the pad than the other, producing a turning moment on the shaft. The problem was overcome by repositioning the pivot so that the gas escaped equally in either direction. The condition being achieved when the shaft remained in a state of static equilibrium.

It was not possible to use the displacement probes mounted in the pad for clearance measurements under jacked conditions, owing to the limitation on their range, (.002"). For this reason, the pivot displacement was measured by an externally mounted probe. The pivot clearance under jacked conditions was .0032", and to give some idea of the frictional loss at such a clearance, calculations were made on the assumption of a .0025 in., concentric clearance, which yielded a horsepower loss of .00115 at 236 c/s. Clearly if this value is compared with the actual losses measured and calculated in tables (4) and (5), the jacked pad can be considered as contributing nothing to the retardation.

Retardation was measured by means of a digital counter, triggered from the tachometer circuit.

To obtain accurate speed values at short and even intervals of time, the counter was set to measure the periodic time over 10 cycles every 6.05 seconds, enabling a five digit accuracy to be recorded, and to be inverted on a desk calculator to obtain speed and retardation.

It was found that a plot of retardation against speed, for both the pad retarding, and the pad jacked, produced an almost linear relationship. For this reason, a linear interpolation was employed to find the retardation at specific speeds under both conditions, enabling the difference due to the frictional drag of the pad, to be determined accurately.

The run-down test with the pad operating hydrodynamically was repeated, and held at certain speeds while clearance measurements were taken, to ascertain the film shape parameters, from which the losses were calculated using equation (48).

The final results are tabulated in tables (4) and (5) and plotted in figure (34).

TABLE (4)

Results from run-down tests		
Speed c/s	Retardation c/s^2	Power Loss HP
225	13.40	.367
200	12.55	.306
175	11.50	.245
150	10.59	.193
125	9.50	.144
100	8.35	.102
77.5	7.36	.069

Moment of inertia of shaft = 1.703×10^{-3} slugs ft^2

TABLE (5)

Calculated values of power loss			
Speed c/s	ϕ	A	Power Loss HP
236	-36.5	.493	.234
196	-32.7	.519	.171
172	-29.2	.543	.139
151	-27.5	.560	.111
132	-23.8	.592	.091
106	-20.1	.639	.064
92.5	-18.2	.655	.052
61.5	-12.4	.779	.032

The above values were calculated from the actual leading and

trailing edge clearances during hydrodynamic operation.

12.3. Discussion of Results.

Figure (34) shows the horsepower loss due to viscous shear between the shaft and the pad.

The upper curve is that plotted from the run-down tests, and the lower one is calculated from the film shape and running conditions. It can be seen, that the calculated values under estimate the losses by almost 50%, and clearly equation (48) can only be used as an approximate guide to design. Nevertheless, it does give some indication of the orders of magnitude to be expected, and some allowance can be made for them in the power supplied.

In reference (17), run-down tests were performed on a 4 inch diameter rotor, freely supported in two sets of tilting pads, and frictional losses, calculated on the basis of a nonlinear velocity distribution, were compared with the experimental results. The calculations yielded losses which were a quarter of those found experimentally, the authors attributing the difference to windage. On the form of rig they used, it was impossible to measure the actual bearing friction experimentally, and to say that the difference is due to windage, can only be speculation. It is likely in fact, that their calculations also under estimated the losses, and the difference was only in part due to windage.

It would appear that if the bearing power consumption given by

equation (48) is doubled, some resemblance to the friction may be attained.

12.4. Pressure Loss.

In integrating the pressure around the pad, a single force was found, which acted along a line through the centre of curvature of the pad, and gave the centre of pressure or pivot position. A similar resultant force will act on the shaft along a line through the shaft centre.

If the pad is tilted about its pivot position, the two centres will not coincide, and the condition shown in fig (36) will arise.

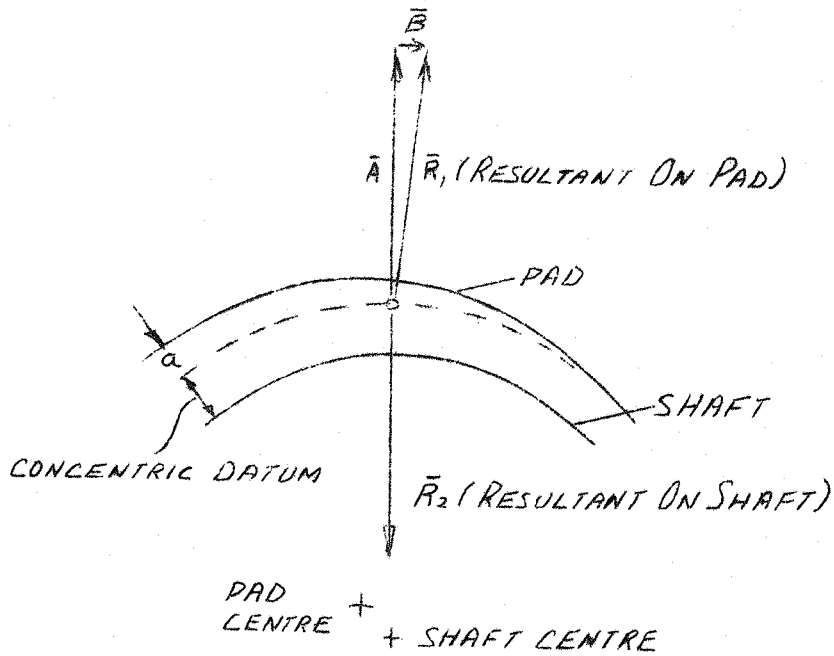

Fig (36)

The resultant forces on the pad and shaft respectively, are given by $\bar{R}_1$ and $\bar{R}_2$. $\bar{R}_1$ can be resolved into two components, one acting

along the line of $\bar{R}_2$, and the other normal to $\bar{R}_2$. The normal component, $(\bar{B})$, must in someway be transmitted through the film as part of the loss, and in effect represents the summation of the pressure forces acting on the projected area 'a'. The value of this component can be found from the product of the load on the pad, and the angle of tilt about the pivot.

The values of horsepower loss due to $\bar{B}$ acting along the film, were calculated from the film shape parameters at various speeds, and at constant load. They are tabulated in table (6).

TABLE (6)

Loss due to pressure calculated from film conditions.

Speed c/s	Angle of tilt about pivot radians	Power loss HP
236	3.48×10^{-4}	1.165×10^{-3}
196	3.43 "	.953 "
172	3.35 "	.817 "
151	3.24 "	.693 "
132	3.22 "	.603 "
106	3.12 "	.469 "
92.5	3.02 "	.396 "
61.5	2.88 "	.251 "

These losses are shown in fig (35) and may be compared with those obtained from the run-down tests in fig (34). The losses due to run-down, are of the order of 500 times as great as those

from pressure. It therefore seems reasonable in the practical bearing, to neglect the effects of the tangential pressure-force.

12.5. Radial Position of the Pivot.

If the frictional forces acting on elemental areas around the pad surface are resolved into a total moment about the pivot, then the pad will tend to pitch.

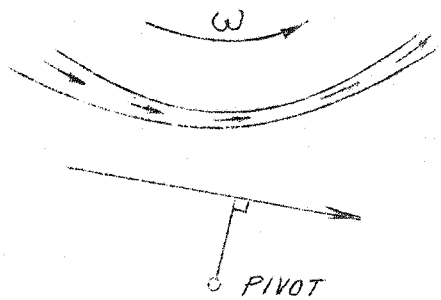

Fig (37a)

Figure (37a) shows the effect of the radial pivot position being a long way outside the pad surface, and figure (37b), the effect of it being near or inside the surface.

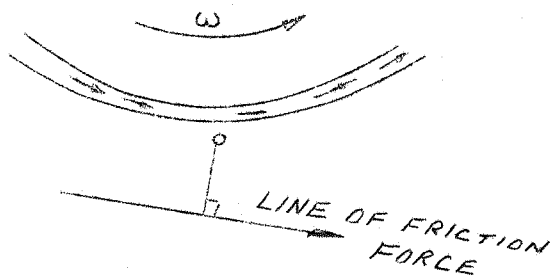

Fig (37b)

In figure (37a) the resultant moment tends to make the pad pitch leading edge down, and figure (37b), leading edge up.

Clearly, at a given running speed and film shape, there exists a radial pivot position about which the turning moment due to friction is zero. It is this position which has been assumed in calculating the design curves, as frictional moments were neglected in their derivation. In practice however, the frictional moments are small compared with the moments due to pivot loading, providing the pivot is not at an unreasonable distance outside the pad surface.

In reference (21), it is claimed that one of the assumptions made, is that the pivot lies on the pad surface. This in fact cannot be so, as friction was neglected in the authors' calculations. A better assumption would be that the pivot was positioned radially, such that frictional turning moments about it were zero.

Although under normal conditions, the frictional moments acting on the pad are small, it is better to position the pivot as near the surface as possible, so that when a lightly loaded pad tends to pitch, the effect of friction is to pull the leading edge clear of the shaft, and thus avoid 'lock-up'.*

* 'Lock-up' is the condition arising when the leading edge of the pad is sucked on to the shaft resulting in seizure.

13.0. Pivot Stiffness.

Pivot stiffness may be defined as the rate of change of film clearance under the pivot with change in pivot load.

This is an important factor in tilting-pad bearing design, since it is in fact, the overall relative stiffness between the shaft and housing, along the line of the pivot. The stiffnesses of the individual pivots may be resolved to determine the radial stiffness of the shaft relative to the bearing housing, in any given direction.

13.1. Obtaining Values of Stiffness from Design Curves.

Stiffness, at a given compressibility number, is best obtained by cross-plotting from curves similar to those shown in figure (38). The alternative method would be to store the curves shown in figures (8) to (12) in a computer. This could only be done by obtaining intermediate points to those computed, by interpolation, and then for a given pivot position, selecting the nearest corresponding values of $\bar{W}$, A, and ϕ, from which the clearance and stiffness could be calculated. Although the amount of storage space required, would not be outside the range of a large computer, it would mean that sets of curves of stiffness for individual pivot positions, and different compressibility numbers should be presented. The author feels that for the purposes of simplicity, it is better to reduce the number of design curves to a minimum, and to use the basic design curves for cross-plotting the load-clearance, and stiffness curves.

Figure (38) may be constructed in two ways. It can be plotted by the direct evaluation of equations (36) to (40) as outlined for the design curves, or it can be cross-plotted from figures (8) to (12). The former method was favoured in this thesis, but in practice it may be more convenient to cross-plot from the design curves.

To obtain the load-clearance curves, and hence the stiffness, lines of constant pivot position are drawn on figure (38), (in this case X_p = .5 and .584), and corresponding values of $\bar{W}$, ϕ, and A, are taken from the curves. From the dimensionless pivot position;

$$X_p = \frac{\theta_1 - \phi}{\psi - \phi} \qquad \text{.....(49)}$$

θ_1 can be determined, and from equation (12), the dimensional clearance.

The various values of W may be obtained from $\bar{W}$ by using equation (40) and figure (15). It should be noted, that Λ plotted in figure (15) can be obtained from Λc by means of equation (47).

13.2. Experimental Investigation.

The investigation required the monitoring of pivot movement during the variation in applied load.

Since the test shaft was mounted vertically in two slave bearings, the danger arose of including the deflection of these bearing films in the absolute deflection of the pivot. Although the capacitance probes fitted at each slave bearing to detect instabilities,

could have been used to measure these deflections, it was a simpler task to position a displacement probe on the reverse side of the shaft to the pivot. The method also took account of any bending of the shaft which may occur.

The pivot deflection was measured by a probe recording the deflection of the loading arm at a position directly along the pivot line. As the actual pivot consisted of a screwed shank surmounted by a conically machined cap of "Araldite", to give electrical insulation for the touch meter, it was necessary to determine the contribution made by the elasticity of this structure to the deflection of the loading arm. This part of the investigation consisted of allowing the pad to remain at rest in contact with the shaft, whilst applying loads to the loading arm, and measuring the arm movement with the probe positioned along the pivot line.

It was found that the elastic deflection of the pivot was of the same order as that of the film, and that under each load, the "Araldite" exhibited a time lag in settling to its fully deflected position. The time lag was also observed during the actual readings, and care was taken in allowing it to settle fully. The readings were found to be repeatable within the limits of the instrumentation.

Before the tests could be started, a datum for film thickness measurements had to be found. This datum was one of zero film

clearance at the pivot, which is obtained when the loaded pad is in contact with the shaft. In practice however, this condition is not so easily achieved, and it was found that the contact friction allowed the pad to remain twisted about the pivot axis. To overcome the problem, the pad was turned slightly by hand, and the point at which the displacement meter needle reached the end of its swing, and began to return, was taken as the point of zero pivot film thickness.

The actual load-deflection curves were obtained by running the shaft and pad combination under hydrodynamic conditions, whilst loading the pad, and taking readings of the pivot deflection. The deflection results so obtained, permitted the calculation of the real pivot movement.

The limitation in load capacity was reached when slight touching was detected; it is likely that this limit could have been exceeded by improving the surface finish.

The results obtained are given in the following table and plotted in figure (39).

TABLE (7)

$\psi - \phi = 120^{o}$ N = 13,200 RPM R = 1 in	$c = .975 \times 10^{-3}$ ins $\Lambda c = 1.5$ L = 3 ins	
PIVOT LOAD W (Lbs)	PIVOT FILM THICKNESS (INS $\times 10^{-3}$)	
	$X_P = .584$	$X_P = .5$
6.12	1.04	.73
9.12	.84	.59
12.12	.70	.48
15.12	.60	.45
18.12	.52	.39
21.12	.46	.32
24.12	.42	.29
27.12	.37	.29

13.3. Discussion of Results.

The experimental and theoretical results shown in figure (39) exhibit some discrepancy. It should be borne in mind at this stage, that the absolute values of deflection obtained from the experiments, are somewhat suspect, due to the difficulty in obtaining the zero clearance value, although there is little doubt in the accuracy of measuring deflection changes. Another quantity known accurately, is the applied load, and it therefore follows, that

comparisons between theory and experiment, should be made in terms of these two parameters.

Under the heavier load conditions and where the pivot film clearances become small, the gradients of the experimental and theoretical curves agree well, the gradient in fact being the stiffness of the individual pad assembly, neglecting material elasticity.

For light loads, the experimental curves tend to indicate a more rapid increase in clearance, than do the theoretical curves. Excluding experimental errors, which it is felt could only partially contribute to this difference, the variation may stem from the following possibility.

Reynold's equation is based on laminar flow between the two bounding surfaces. When the clearance between the surfaces increases, so does the value of Reynold's number based on the film thickness. Reynold's number of course is a measure of the transition between laminar and turbulent flow. In a full journal bearing, the film thickness is limited by the machined in clearance of the bearing, but for a pad, it is only limited by pitch stability, and may become large in comparison. It was found by Abramowitz ref (22), that for a water lubricated tilting-pad thrust bearing, transition could commence at a Reynold's number as low as 600. If the same Reynold's number applied for a tilting-pad air-bearing, a clearance of $.9 \times 10^{-3}$ ins would be sufficient to cause

transition at the test speed of 13,200 r.p.m. Since the pivot thickness at the lighter loads shown in figure (39), are approaching this value, it is likely that the leading edge thickness has exceeded it, and greater lift is being generated than is predicted by the laminar theory.

The theory would also tend to predict a limit to the clearance under lightly loaded conditions, which would be brought about by the reduced convergence of the wedge, and could be likened unto a full journal bearing with the journal running at the centre of the bearing. This is apparent from fig (39), since the theoretical curves, if continued, would intersect the clearance axis. If the experimental conditions do create turbulence, the experimental curves may cross the clearance axis at some higher value.

Another factor emerging from the curves, is the increase in stiffness at high loads, occurring when the pivot position is moved nearer to the centre of the pad. In this particular case, for a load of 20 Lbs, the theoretical curves give stiffnesses of 5.5×10^4 Lbs/in for $X_p = .584$ and 11×10^4 Lbs/in for $X_p = .5$.

Stiffness is important in dynamically loaded systems, and it would appear that for heavily loaded bearings, a central pivot position would be preferred. It must be pointed out however, that a centrally pivoted pad is more prone to pitch instability when lightly loaded, (a condition discussed in the next chapter), and

care must be taken to see that a dynamic load does not exceed this lower limit.

Generally, for design purposes, it is more convenient to work in terms of minimum film thickness than pivot thickness, as the former is governed by accuracy of machining.

In conclusion, it can be said that the design curves predict an accurate pivot stiffness providing the bearing is operating at one of the smaller clearances, i.e. something less than half the machined in clearance. It is also shown that a centrally pivoted bearing is stiffer, at these clearances, although the clearance may be smaller at a given load, and care must be taken to see that the lower load limit is not exceeded for reasons of stability.

14. Pitch Stability.

The stability of individual pads in pitch, is an important factor in bearing design. If the pads begin to pitch, there is a danger that the leading edge may come into contact with the shaft, and 'lock-up' result.

Under normal operating conditions, the gas film is either convergent, or convergent-divergent as shown in fig (40a). If however, the fluid film is allowed to become divergent-convergent, as shown in fig (40b), the narrow clearances at the leading and trailing edges will cause a reduction in pressure at the leading edge, and possibly an increase in pressure at the trailing edge, with the result that the pad will tend to pitch leading edge down.

The boundary between these two conditions, is when the film is parallel, in which case $H_m = 1$.

If H_m always occurs at $\theta = + \frac{\pi}{2}$, and if under normal operating conditions the film is convergent-divergent, which is the basis of the design curves, then when H_m becomes greater than one, the divergent-convergent film results. Although in simple theory, provided that $H_m < 1$ the pad would be stable; in practice, any slight disturbing force could cause H_m to exceed one, and then the instability could occur. It is therefore better to design with H_m as far below unity as possible.

It should be noted that when $H_m = 1$ the load capacity is zero,

from which it follows that the pad must remain loaded for stable operation. A simple way of achieving this condition, is to pre-load the bearing, either by spring loading one of the pivots, or by fixing the pivot circle such that when the maximum journal load is applied, all the pads remain loaded.

It was considered unwise to attempt to study this aspect of tilting-pad performance on the rig described in this thesis, since the effects the pressure tapping tubes and cavities have on the damping of the pad is unpredictable. In fact a full investigation of pad stability, is a project in itself.

15.0. Use of Design Curves.

By virtue of their geometry, tilting-pad bearings are in general more complex to design than the plain journal bearing. The geometry of a plain journal bearing is simply defined by the journal, and bearing diameters, and by the eccentricity ratio. A multi-pad bearing on the other hand, requires the relative geometry between the shaft and each pad to be given. Although the minimum clearance under each pad may be likened to the eccentricity of the plain journal, each pad also makes an angle with the shaft.

In any study of pad bearings, the properties of a single pad must be examined, as in this thesis, and the complete bearing studied in terms of the equilibrium conditions existing between individual pads.

This section sets out to give some of the factors governing the design of the multipad system, and includes a set of five worked examples illustrating the application of the single pad design curves to the complete bearing. To avoid unnecessary repetition, it has been assumed that the reader will study the examples in numerical order. Only pads of 120^{o} span are considered, as design curves for other pad configurations are not included in this thesis.

15.1. Load Capacity when $\Lambda c \to \infty$.

Unlike a liquid bearing, a particular gas-bearing can only support a maximum finite load, even though the speed of rotation, or Λc, may tend to infinity. Figure (45) shows a plot of $\bar{W}$ against X_p for $\Lambda c \to \infty$, with varying H_m. This graph may be used to make a preliminary study of the bearing should the load capacity of a particular configuration be in doubt. The graph yields the maximum load that it is possible to carry with a single pad. It is used in the same way as the other $\bar{W}$-X_p design curves, but has the advantage of displaying H_m on the one graph. It should be noted that when $\Lambda c \to \infty$, $I_Y \to L/R$.

15.2. Selection of H_m.

The effect of H_m on pitch stability has already been discussed in the previous chapter. The other factors affecting H_m, are load capacity and machining accuracy.

It is evident from the design curves, that if the other parameters are held constant as H_m decreases, the dimensionless load $\bar{W}$ becomes greater. It is therefore desirable, in order to support a substantial load, to maintain H_m at a minimum. But the minimum value of H_m is also dictated by the accuracy of manufacture. If the bearing is to function hydrodynamically, the two surfaces must remain out of contact. This consideration is illustrated in example (1).

15.3. Optimum Conditions.

In deciding the optimum design conditions, the operating conditions must be considered. For example; if the bearing is under some form of dynamic loading, high pivot stiffness may be desirable, in which case, the pad would be pivoted near its centre, (section 13). The stiffness of a particular geometry can always be determined, by plotting out the load-displacement curves, using the method in example (5).

On the other hand, it may be necessary to obtain the greatest minimum clearance for a given load, in which case, the bearing would be designed with the pads operating near to the peaks on the $\bar{W}$-X_p curves, which are plotted for constant H_m. It should be pointed out at this stage, that a small shift from the peak conditions could cause a rapid fall-off in $\bar{W}$, it is therefore better to choose a design with the pivot a little nearer the pad centre, so that some latitude can be given to the bearing manufacture.

15.4. Distortion.

It must be remembered that the design curves are presented for particular bearing geometries, and that any pad distortion due to either loading, or thermal conditions, must be accounted for.

15.5. Examples.

Example 1.

A shaft is supported on two bearings, each bearing consisting of two 120^{o} pads, with pivots positioned at 60^{o} either side of the vertical centre-line, and at .55 of the distance from the pad leading edge. The diameter of the shaft is 6 ins, and the length of each pad is 10 ins.

The nominal machined-in radial clearance, between the pads and the shaft, is 1.5×10^{-3} ins, and the accuracy of machining for both the shaft and the pad, is $\pm .2 \times 10^{-3}$ ins.

What is the load capacity of the assembly when rotating at 3,000 r.p.m.?

The total variation in accuracy, which could reduce the film thickness to zero, is $.4 \times 10^{-3}$ ins, or as a proportion of the machined-in clearance $.4/1.5 = .267$.

This means that if the value of H_m was .267, the two surfaces may touch. In order to avoid touching, let the design be $H_m = .4$

Considering a single pad:

$$\Lambda c = \frac{6\mu\omega R^2}{p_a c^2}$$

$$= 6 \times \left(\frac{3.728}{10^7}\right) \times \left(\frac{2\pi \times 3{,}000}{60}\right) \times \left(\frac{3}{12}\right)^2 \times \left(\frac{12}{1.5\times10^{-3}}\right)^2 \times \left(\frac{1}{14.7\times144}\right)$$

$$\Lambda c = 1.33$$

From fig (10) i.e. the design curves for $H_m = .4$, when $X_p = .55$ and $\Lambda c = 1.33$, then $\bar{W} = .66$ and $\phi = 9^o$.

But the pivot load W, from equation (40) is:

$$W = p_a R^2 I_Y \bar{W}$$

Equations (46) and (47) give:

$$\Lambda = \Lambda c \left(\frac{1}{\left[1 + A \frac{(\cos\psi - \cos\phi)}{(\psi - \phi)} \right]} \right)^2$$

where $\psi - \phi = 120^o$, or $\psi = 129^o$

and $A = 1 - H_m$,

therefore,

$$\Lambda = 1.33 \left(\frac{1}{\left[1 + .6 \frac{(\cos 129^o - \cos 9^o)}{2.09} \right]} \right)^2$$

$$\Lambda = 4.55$$

Now from figure (15), with $L/R = 10/3 = 3.33$, and $\Lambda = 4.55$, $I_Y = 2.62$, ~~but~~ then:

$$W = p_a R^2 I_Y \bar{W} = 14.7 \times 3^2 \times 2.62 \times .66$$

$$= 229 \text{ Lbs}$$

This is the load applied along the axis of each pivot.

The total load supported by the four pads is:

$$4 \times 229 \cos 60^o$$

Total load = <u>458 Lbs</u>

Example (2).

A rotor is supported in the same manner as in example (1), the dimensions of the pad and shaft, the accuracy of machining, and the speed of rotation, being the same. The bearing must however support a load, inclusive of shaft weight, of 550 lbs. What must the machined-in clearance be?

The load carried by each pad is:

$$\frac{550}{4 \cos 60^{\circ}} = 275 \text{ Lbs}$$

Since the load per pad, is greater than in the previous example, then either Λc must increase, or H_m decrease. Because of the machining accuracy, the latter is not possible, and since Λc is inversely proportional to c, then c must become less than 1.5×10^{-3} ins. It must be remembered that H_m is a proportion of c, and to maintain the actual minimum clearance, when c is reduced, H_m must be increased.

Let us therefore assume that H_m becomes .5.

For this type of problem, it is necessary to plot a small section of graph in the region of interest, and for this particular problem; a graph of W against Λc.

It is convenient to calculate the values in a tabular form for the graph. These values are calculated in exactly the same way as example (1).

Taking values of Λc = 2, 3, 5 and 6:-

REMARKS	Λc	2	3	5	6
From fig (11),	$\bar{W}$	.56	.63	.692	.708
" " "	ϕ	9^o	12^o	16^o	18^o
$\psi-\phi = 120^o$	ψ	129^o	132^o	136^o	138^o
From eq^{n}s 46 & 47	Λ	5.36	8.20	14.0	16.99
" fig 15	I_Y	2.72	2.90	3.08	3.15
" eq^n 40	W(lbs)	202	242	282	295

These values are plotted in fig (41). From this graph it can be seen that for W = 275 Lbs, Λc = 4.5,

$$\text{but } \Lambda c = \frac{6\mu\omega R^2}{p_a c^2}$$

$$\text{or } 4.5 = 6 \times \left(\frac{3.728}{10^7}\right) \times \left(\frac{2\pi \times 3{,}000}{60}\right) \times \left(\frac{3}{12}\right)^2 \times \left(\frac{12}{c}\right)^2 \times \left(\frac{1}{14.7 \times 144}\right)$$

from which $\underline{c = .81 \times 10^{-3} \text{ ins.}}$

Now H_m = .5 and thus $h_m = .405 \times 10^{-3}$ ins. This minimum clearance only just allows for the machining accuracy, and in practice, it would be better to increase this minimum clearance, by trying a greater value of H_m, or by changing some of the parameters, such as increasing the speed, or moving the pivot to the .6 position.

Example (3).

A triple-pad bearing, supports a shaft load of 800 Lbs, and the top shoe has a pre-load of 400 Lbs. If the diameter is 8 ins, the length of the pads 12 ins., the machined-in radial clearance 2×10^{-3} ins., and the operating speed 5,000 r.p.m., what is the minimum clearance under each pad, assuming that the pivot position is .6 of the way from the leading edge on all pads, and the pivot for the top pad lies on the vertical centre-line?

$$\Lambda c = \frac{6\mu\omega R^2}{p_a c^2}$$

$$= 6 \times \left(\frac{3.728}{10^7}\right) \times \left(\frac{2\pi \times 5{,}000}{60}\right) \times \left(\frac{4}{12}\right)^2 \times \left(\frac{12}{2\times 10^{-3}}\right) \times \left(\frac{1}{14.7\times 144}\right)$$

$$= 2.17$$

For this example, it is necessary to determine H_m or A, $(A = 1-H_m)$, for various loads applied to a particular pad. It should be noted that all the pads are operating under similar conditions, and it is therefore possible to construct a single graph of W against H_m, and to apply it to any of the pads in the system.

Again the following values are calculated in a tabular form.

REMARKS	H_m	.2	.3	.4	.5	.6
{with X_P = .6}	$\bar{W}$	2.16	1.43	1.01	.73	.52
{ } {From curves }	ϕ	9^o	5^o	0^o	-8^o	-19^o
$\psi - \phi = 120^o$	ψ	129^o	125^o	120^o	112^o	101^o
From eq'ns (46 & 47)	Λ	15.0	11.1	6.73	4.81	3.56
" fig (15)	I_Y	2.75	2.65	2.5	2.32	2.16
" eqn. (40)	W	1,398	891	594	398	264

A graph of W against H_m is given in figure (42).

For the top pad, a load of 400 Lbs yields H_m = .495.

The load supported by each of the lower pad pivots, is:-

$$W = \frac{1,200}{2 \cos 60} = 1,200 \text{ Lbs}$$

giving H_m = .230.

Since the minimum clearance h_m of the pad circle, occurs at $\theta = 90^o$, then provided $-30^o < \phi < 90^o$, the minimum clearance will occur beneath the pad, as in this example. For $\phi < -30^o$, the actual minimum clearance of the pad will be at the trailing edge, and this must be calculated from

$h = c(1-A\sin\theta)$, where $\theta = \psi$.

For this example the minimum clearance for the top pad is:-

$$.495 \times 2 \times 10^{-3} = \underline{.990 \times 10^{-3} \text{ ins.}},$$

and for the lower pads:-

$$.230 \times 2 \times 10^{-3} = \underline{.460 \times 10^{-3} \text{ ins}}.$$

Example (4)

It is necessary for a shaft to rotate in either direction. It is supported in two pairs of 120° pads, the pivots being 60° either side of the vertical centre-line. The journal diameter is 2 ins., and the length of pads 4 ins., with a radial machined-in clearance of 5×10^{-4} ins. If the weight of the shaft is 50 Lbs, what would be the vertical change in displacement of the shaft, if the speed of rotation was reduced from 12,000 r.p.m. to 4,000 r.p.m?

In order that the shaft may rotate in either direction, the pads must be pivoted at their centres, i.e. $X_p = .5$.

Now $\Lambda c = \dfrac{6\mu\omega R^2}{p_a c^2}$ and R = 1 in.

with $c = 5 \times 10^{-4}$ ins.

Then for a rotation of 12,000 r.p.m.,

$$\Lambda c = 5.2$$

and for 4,000 r.p.m.,

$$\Lambda c = 1.73$$

To find the deflection, the film shape parameters A, and ϕ must be known for each running condition. Since $H_m = 1-A$, a graph of H_m against load, and against ϕ, will allow these parameters to be determined for the particular running conditions.

As in previous examples, the following tabular layout has been adopted.

For N = 12,000 r.p.m.:-

REMARKS	H_m	.3	.4	.5	.6
	$\bar{W}$	1.09	.73	.52	.36
	ϕ	29°	27°	25°	23°
	ψ	149°	147°	145°	143°
Extrapolating from Fig 15	I_Y	3.85	3.8	3.75	3.65
	W(Lbs)	61.8	40.7	28.6	19.3

These values are plotted in figure (43a).

In a similar manner, the curves given in figure (43b) were calculated for N = 4,000 r.p.m.

Now the load per pad pivot, is:

$$W = \frac{50}{4 \cos 60^\circ} = 25 \text{ Lbs.},$$

from figure (43), the following values result:-

$$N = 12{,}000 \text{ r.p.m.} \qquad H_m = .535, \quad \phi = 24.5^\circ,$$

$$N = 4{,}000 \text{ r.p.m.} \qquad H_m = .45 \quad \phi = 18^\circ,$$

but $h = c(1-A\sin\theta)$ where $A = 1-H_m$, the pivot clearance, is the value of h when $\theta = \theta_1$,

and $$X_P = \frac{\theta_1-\phi}{\psi-\phi} = .5,$$

giving a pivot film thickness of 2.68×10^{-4} ins, for N = 12,000 r.p.m., and 2.32×10^{-4} ins, for N = 4,000 r.p.m.

The pivot deflection becomes:-

$$(2.68-2.32) \times 10^{-4} = 3.4 \times 10^{-5} \text{ ins.}$$

The vertical deflection of the shaft

$$= 3.4 \times 10^{-5} \cos 60^{\circ} = 1.7 \times 10^{-5} \text{ ins.}$$

If a bearing is operating under fluctuating speed conditions, a graph of rotor displacement against speed may be plotted by calculating various points in the above manner. It should be remarked, that when the two load supporting pivots are displaced symmetrically on either side of the vertical load line, the load line becomes the locus of the shaft centre.

Example (5).

If the shaft in example (4), now weighs 20 Lbs, and continues to run at 12,000 r.p.m., but if a top shoe is fitted to each bearing, with the pivot rigidly connected to the other two pivots via the bearing housing, such that the total pre-load under these conditions is 60 Lbs, what will be the deflection of the shaft, if a load of 20 Lbs is applied to it.

The shaft load, pre-load, and the applied load for each bearing, will be a half of those stated above.

The running conditions for a single pad are similar to those given in the last example, with the result that Ac is also 5.2, and figure (43a) may be applied to a single pad in this example.

From figure (43a) the following values of W, H_m and ϕ have been obtained, which enables the calculation of the pivot film thickness to be made. The absolute displacement of the shaft is based on the zero datum being the shaft resting statically on the pads, and is equal to cos 60° times the pivot film clearance. As in the previous examples, it can be shown that the load applied to each lower pivot is equal to the total load on the bearing, since the pivots are 60° from the load line.

The following table will enable two graphs of displacement against load to be plotted:-

REMARKS	W	60	50	40	30	20
From fig (43a)	H_m	.305	.340	.405	.490	.575
" "	ϕ	28.9°	28.1°	26.9°	25.2°	23.6°
$X_P = \frac{\theta_1-\phi}{\psi-\phi}$	θ_1	88.9°	88.1°	86.9°	85.2°	83.6°
$h = c(1-A\sin\theta_1)$	h_1 ins 10^{-4}	1.525	1.70	2.02	2.46	2.89
Absolute shaft displacement	$h_1\cos 60^\circ$ ins 10^{-4}	.762	.85	1.01	1.23	1.44

Where h_1 is the actual clearance at the pivot position.

Now the pivot film clearance for the top pad will be h_1 and the absolute displacement of the shaft is $h_1 \cos 60^\circ$ or $\frac{1}{2}h_1$.

In figures (44a) and (44b) the pivot film thickness for the top pad, and the absolute displacement of the shaft are plotted against load.

When the bearing is operating under the 'no load' condition, the load on the top pad, is the pre-load of 30 Lbs per bearing, and on the lower pair of pads, it is the preload plus the shaft weight = 30 + 10 = 40 Lbs.

From figures (44a) and (44b) under these conditions,

Top pivot film thickness = 2.46×10^{-4} ins.,

Absolute shaft displacement = 1.0×10^{-4} ins.

If we plot the change in preload on the top pad with shaft deflection, for any given deflection, by adding the shaft weight, shaft load, and the preload, it is possible to plot the loading on the lower bearing against the shaft deflection. In a like manner, the load capacity of the lower bearings, can be plotted against deflection. Since the deflection must be common to the top pad and the lower pads, if these curves are plotted on the same axes, their intersection denotes the condition of equilibrium, and the corresponding deflection can be noted.

Deflection (ins$\times 10^{-5}$)	0	.5	1	1.5	2
Top pivot (ins$\times 10^{-4}$) clearance	2.46	2.51	2.56	2.61	2.66
Top pivot load (Lbs)	30	29	28	27	26
Abs. shaft (ins$\times 10^{-4}$) displacement	1.0	.95	.9	.85	.8
Load capacity (Lbs)	40	43	46	50	55
Loading (Lbs)	50	49	48	47	46

From figure (44c) the intersection occurs at 1.2×10^{-5} ins. Hence the deflection = 1.2×10^{-5} ins.

A complete load-displacement plot can be made in this way, in order to determine the overall stiffness of such a bearing.

In practice, the minimum clearance often occurs near the pivot position, and in these cases, a good approximation can be made for

the pivot film clearance and the pivot film stiffness by considering only the minimum clearance.

16.0 Conclusions.

The approximations made in obtaining equation (31), appear to be justified experimentally, and are also confirmed by the comparison made with the numerical curves obtained from reference (17). Indeed, had this approximation not been made, it would not have been possible to obtain an analytical solution, which satisfies the boundary conditions at the sides of the pad, and most certainly, would not have provided a solution where the circumferential and axial conditions were separable.

Tests have been made on the approximation over a limited range of Λc, but it is shown that as $\Lambda c \to \infty$, the finite bearing correction tends to zero, resulting in the same load capacity per unit length as an infinite bearing; in which case the approximation tends to an exact solution.

It has also been demonstrated, that the analytical solution for the infinite bearing, with P_1 as the mean film pressure, can be considered valid for high compressibility numbers; this is the region in which it is most useful, as it is here where numerical solutions encounter stability problems.

The result of this work, is sets of design curves, which may be used to design 120° pad bearings over the complete range of length to diameter ratio, at the same time, predicting their performance quite accurately. The errors due to the approximations

are likely to be far less than those encountered in manufacture. This offers a major step-forward in the steady state design of the tilting-pad gas-bearing, as previously, only the numerical curves presented in reference (19) were available to the designer. These curves only covered a very limited range of pad configurations, and for each length to diameter ratio, the set of curves required, took several hours to compute, reference (23), whereas a set of curves at a constant H_m, presented in this thesis, took only a few minutes to compute.

It has also been shown experimentally, that these design curves may be used to accurately predict the overall stiffness of the single pad system.

The use of gauge pressure instead of absolute pressure, has simplified the evaluation of the boundary conditions, and has also reduced the round-off errors at low compressibility numbers. This problem was also reported in reference (23), and the author has already made a written contribution to that paper making the above suggestion. It would appear, that this technique could be employed to advantage on many forms of bearing, any sub-ambient pressures being denoted as negative.

Finally, an experimental investigation of the viscous losses in the bearing, has shown that the theoretical prediction may only

be used as a guide, and not as an "exact" design quantity. As far as the author is aware, this is the first time the viscous losses in a tilting-pad gas-journal-bearing have been studied in this detail.

16.1. Suggestions for Further Work.

The most obvious extension of this study, is the production of design curves for spans other than 120^{o} it must be borne in mind, that the accuracy of approximation should first be tested for these new configurations. An improved presentation of the design curves could be made, by plotting the characteristics for a particular pivot position; this would allow H_m to be infinitely variable, and would assist in the derivation of the load-displacement and stiffness curves.

As it stands, the theory is quite general within the limits of the approximation, and lends itself to other forms of partial arc journal bearing, such as the axial grooved bearing. It may however be more convenient in such a case, to present the design curves in terms of other parameters, for example eccentricity.

One possible application, is to speed-up the computation of the pressure profile for a spiral groove journal bearing. It is possible that the land between the grooves could be considered as a partial journal bearing, with the ambient conditions at the leading and trailing edges replaced by the conditions existing in the groove.

A change of coordinates may be required to account for the angle of the spiral.

A most promising field of application is in the study of the dynamic characteristics of the tilting-pad bearing. At present the study is of a numerical nature, and is most demanding on computational time. The steady-state approach outlined in this thesis, could probably be utilised in the form of changing steady state conditions producing a rapidly obtained approximation, which could be used as a starting value for the final numerical solution.

It is the intention of the author to follow-up some of the above suggestions.

Appendix (1)

C_5 as a Constant.

To show that when C_5 is a constant:

$$F = F_\infty + C_5 e^{\left(\frac{\Lambda}{2}\right)\theta} \sin\pi\frac{(\theta-\phi)}{(\psi-\phi)} \cosh KY$$

satisfies equation (15).

let $F = F_\infty + C_5 g \cosh KY$

$$\frac{\partial F}{\partial \theta} = \frac{\partial F_\infty}{\partial \theta} + C_5 \frac{\partial g}{\partial \theta} \cosh KY$$

$$\frac{\partial^2 F}{\partial \theta^2} = \frac{\partial^2 F_\infty}{\partial \theta^2} + C_5 \frac{\partial^2 g}{\partial \theta^2} \cosh KY$$

$$\frac{\partial^2 F}{\partial Y^2} = C_5 g K^2 \cosh KY$$

Substituting into equation (15):-

$$\frac{\partial^2 F_\infty}{\partial \theta^2} + C_5 \frac{\partial^2 g}{\partial \theta^2} \cosh KY + C_5 g K^2 \cosh KY$$
$$- \Lambda \frac{\partial F_\infty}{\partial \theta} - \Lambda C_5 \frac{\partial g}{\partial \theta} \cosh KY = A(P_1 \sin\theta - \Lambda\cos\theta)$$

subtracting the equation for the infinite bearing, equation (16), and dividing by $C_5 \cosh KY$:-

$$\frac{\partial^2 g}{\partial \theta^2} + gK^2 - \Lambda\frac{\partial g}{\partial \theta} = 0 \qquad \text{.....(a)}$$

$$\text{but} \quad g = e^{\left(\frac{\Lambda}{2}\right)\theta} \sin \pi \frac{(\theta-\phi)}{(\psi-\phi)}$$

then substituting into (a) and dividing throughout by the exponential and sin terms yields:-

$$\frac{\pi^2}{(\psi-\phi)^2} + \frac{\Lambda^2}{4} - K^2 = 0$$

$$\text{but} \quad K^2 = \frac{\pi^2}{(\psi-\phi)^2} + \left(\frac{\Lambda}{2}\right)^2$$

therefore equation (29) satisfies equation (15) provided C_5 is a constant.

Appendix (2)

The Effect of C_5 being a Variable.

let $C_5 = C(\theta)$

therefore:-

$$F = F_\infty + Cg \cosh KY$$

$$\frac{\partial F}{\partial \theta} = \frac{\partial F_\infty}{\partial \theta} + \frac{\partial C}{\partial \theta} g \cosh KY + C \frac{\partial g}{\partial \theta} \cosh KY$$

$$\frac{\partial^2 F}{\partial \theta^2} = \frac{\partial^2 F_\infty}{\partial \theta^2} + \frac{\partial^2 C}{\partial \theta^2} g \cosh KY + 2 \frac{\partial C}{\partial \theta} \frac{\partial g}{\partial \theta} \cosh KY + C \frac{\partial^2 g}{\partial \theta^2} \cosh KY$$

and $$\frac{\partial^2 F}{\partial Y^2} = K^2 Cg \cosh KY$$

Substituting into equation (15)

$$\frac{\partial^2 F_\infty}{\partial \theta^2} + \frac{\partial^2 C}{\partial \theta^2} g \cosh KY + 2 \frac{\partial C}{\partial \theta} \frac{\partial g}{\partial \theta} \cosh KY + C \frac{\partial^2 g}{\partial \theta^2} \cosh KY + K^2 Cg \cosh KY - \Lambda \frac{\partial F_\infty}{\partial \theta} - \Lambda \frac{\partial C}{\partial \theta} g \cosh KY - \Lambda C \frac{\partial g}{\partial \theta} \cosh KY$$

$$= A(P_1 \sin\theta - \Lambda \cos\theta) + \delta(\theta) \qquad \text{.....(b)}$$

where $\delta(\theta)$ is some deviation from the zero due to assuming "C" to be

a variable.

Subtracting equation (16) and dividing by cosh KY

$$C\left(\frac{\partial^2 g}{\partial\theta^2} + gK^2 - \Lambda\frac{\partial g}{\partial\theta}\right) + \frac{\partial^2 C}{\partial\theta^2}\,g + 2\,\frac{\partial C}{\partial\theta}\,\frac{\partial g}{\partial\theta} - \Lambda\frac{\partial C}{\partial\theta}\,g = \frac{\delta(\theta)}{\cosh KY}$$

From appendix (1), the first group on the left hand side of the above equation results from the correct solution, and is zero, therefore:-

$$\frac{\partial^2 C}{\partial\theta^2}\,g + 2\frac{\partial C}{\partial\theta}\,\frac{\partial g}{\partial\theta} - \Lambda\frac{\partial C}{\partial\theta}\,g = \frac{\delta(\theta)}{\cosh KY} \qquad \text{.....(c)}$$

now C_5 from the analysis was assumed to be

$$C_5 = \frac{-F_\infty}{g\cosh\frac{KL}{2R}} = C(\theta), \text{ in this appendix.}$$

$$= -\frac{DF_\infty}{g} \text{ say.}$$

Substituting into equation (c)

$$D\left(\frac{2}{g}\,\frac{\partial g}{\partial\theta}\,\frac{\partial F_\infty}{\partial\theta} - \frac{\partial^2 F_\infty}{\partial\theta^2} - \frac{2}{g^2}\,F_\infty\left(\frac{\partial g}{\partial\theta}\right)^2 + \frac{1}{g}\,F_\infty\,\frac{\partial^2 g}{\partial\theta^2}\right)$$

$$-\frac{2D}{g}\,\frac{\partial F_\infty}{\partial\theta}\,\frac{\partial g}{\partial\theta} + \frac{2D}{g^2}\,F_\infty\left(\frac{\partial g}{\partial\theta}\right)^2 + \Lambda D\,\frac{\partial F_\infty}{\partial\theta}$$

$$-\frac{\Lambda D}{g}\,F_\infty\,\frac{\partial g}{\partial\theta} = \frac{\delta(\theta)}{\cosh KY}$$

hence:-

$$\left(\frac{\partial^2 F_\infty}{\partial\theta^2} - \Lambda\frac{\partial F_\infty}{\partial\theta}\right) - \frac{F_\infty}{g}\,\frac{\partial^2 g}{\partial\theta^2} + \frac{\Lambda}{g}\,F_\infty\,\frac{\partial g}{\partial\theta} = \frac{-\delta(\theta)}{D\cosh KY}$$

and then from equation (16) becomes:-

$$A(P_1\sin\theta-\Lambda\cos\theta) - \frac{F_\infty}{g}\left(\frac{\partial^2 g}{\partial\theta^2} - \Lambda\frac{\partial g}{\partial\theta}\right) = \frac{-\delta(\theta)}{D\cosh KY}$$

but

$$g = e^{\left(\frac{\Lambda}{2}\right)\theta}\sin\pi\frac{(\theta-\phi)}{(\psi-\phi)}$$

therefore substituting and simplifying:-

$$A(P_1\sin\theta-\Lambda\sin\theta) + F_\infty\left(\frac{\pi^2}{(\psi-\phi)^2} + \left(\frac{\Lambda}{2}\right)^2\right) = \frac{-\delta(\theta)}{D\cosh KY}$$

from eq 30

or

$$A(P_1\sin\theta-\Lambda\cos\theta) + F_\infty K^2 = \frac{-\cosh\frac{KL}{2R}\,\delta(\theta)}{\cosh KY}$$

It can be seen from a study of the theoretical pressure profiles that a good approximation results if $P_1 = 0$

$$\therefore \quad \Lambda A\cos\theta - F_\infty K^2 = \delta(\theta)\frac{\cosh\frac{KL}{2R}}{\cosh KY}$$

or:-

$$\frac{\Lambda\Lambda\cos\theta}{1-A\sin\theta} - P_\infty K^2 = \frac{\delta(\theta)}{1-A\sin\theta}\,\frac{\cosh\frac{KL}{2R}}{\cosh KY} \qquad \ldots\ldots\ldots\ldots(d)$$

If the assumption that C_5 may be an arbitrary function of θ, is valid as a good approximation, then the right hand side must be small, or in the limit tend to zero. If the right hand side was zero, the assumption would be exact, and then the two terms on the left hand side, would be everywhere equal to each other.

If $\frac{\Lambda A\cos\theta}{K^2(1-A\sin\theta)}$ is plotted on the same axes as P_∞, then for a good approximation, the difference between these two curves must be small.

In figure (18) a comparison has been made with the direct numerical method employed in reference (17) and the analytical end flow correction. One of these curves will therefore be used to study the magnitude of the right hand side of equation (d). Since the curve of $\Lambda c = 1.5$ is the one most affected by the end flow, this curve will be used as an example.

P_∞ is plotted in figure (46) together with the corresponding curve: $\frac{\Lambda A\cos\theta}{1-A\sin\theta}$. It would appear that the maximum values of the right hand side of equation (d), (i.e. the maximum differences between the two curves), are of the same order as the difference in assuming P_1 equal to ambient, and P_1 equal to the mean film pressure in section (8.0). Since P_1 appears on the right hand side of the original differential equation, (b), it would affect the pressure profile in a similar way to which the right hand side of (d) affects the profile end flow correction. Furthermore, the right hand side of equation (d), takes positive and negative values, which will result in a small average value over the length of the film.

It would seem in this particular case, that equation (31) is a good approximation to the solution of the original differential

equation in F, this is further borne out by section (8.0). If at higher compressibility numbers, the end flow correction error does increase, this is less important, since as previously mentioned, the end flow correction itself becomes small.

Individual cases may be examined in this way to give some idea of the accuracy of the solution.

APPENDIX (3)

Evaluation of Integrals.

The groups I_1, I_2, I_3, I_4, I_5, I_6, and I_7, were evaluated in the following way:

$$I_1 = \int_{\phi}^{\psi} \frac{C_1 e^{\Lambda\theta}\cos\theta d\theta}{1-A\sin\theta}$$

Expanding the denominator as a binomial series

$$I_1 = \int_{\phi}^{\psi} C_1 e\Lambda\theta\cos\theta(1+A\sin\theta+A^2\sin^2\theta+A^3\sin^3\theta+A^4\sin^4\theta)d\theta$$

$$= C_1 \int_{\phi}^{\psi} e^{\Lambda\theta}\{\left(1 + \frac{A^2}{4} + \frac{A^4}{8}\right)\cos\theta+\left(\frac{A}{2} + \frac{A^3}{4}\right)\sin2\theta$$

$$- \left(\frac{A^2}{4} + \frac{3A^4}{16}\right)\cos3\theta - \frac{A^3}{8}\sin4\theta + \frac{A^4}{16}\cos5\theta\}d\theta$$

$$= C_1 \int_{\phi}^{\psi} e^{\Lambda\theta}(A_1\cos\theta+A_2\sin2\theta-A_3\cos3\theta-A_4\sin4\theta+A_5\cos5\theta)d\theta$$

Yielding the value given for I_1 in section (4.2)

$$I_2 = \int_{\phi}^{\psi} \frac{C_2\cos\theta d\theta}{1-A\sin\theta}$$

$$= \frac{-C_2}{A}\left[\log(1-A\sin\theta)\right]_{\phi}^{\psi}$$

$$I_3 = \Lambda(1+P_1) \int_\phi^\psi \frac{\cos^2\theta d\theta}{1-A\sin\theta}$$

$$= \frac{\Lambda(1+P_1)}{A^2} \{\int_\phi^\psi \frac{A^2-1 \quad d\theta}{(1-A\sin\theta)} + \int_\phi^\psi A\sin\theta d\theta + \int_\phi^\psi d\theta\}$$

The first integral may be evaluated using the tangent of the half angle substitution:-

$$I_3 = \frac{\Lambda(1+P_1)}{A^2} \left[\frac{2(A^2-1)}{(1-A^2)^{\frac{1}{2}}} \tan^{-1}\left(\frac{\tan\frac{\theta}{2}-\Lambda}{(1-A^2)^{\frac{1}{2}}}\right) - A\cos\theta+\theta\right]_\phi^\psi$$

$$I_4 = \int_\phi^\psi \frac{\sin\theta\cos\theta d\theta}{1-\Lambda\sin\theta}$$

This may be evaluated by making a substitution of the form:-

$$u = 1-\Lambda\sin\theta$$

giving:-

$$I_4 = \frac{1}{A^2} \left[(1-A\sin\theta)-\log(1-A\sin\theta)\right]_\phi^\psi$$

and since the limits of integration are given, this reduces to:-

$$I_4 = \frac{-1}{A^2} \left[A\sin\theta+\log(1-\Lambda\sin\theta)\right]_\phi^\psi$$

$$I_5 = \int_\phi^\psi \frac{C_1 e^{\Lambda\theta}\sin\theta d\theta}{1-A\sin\theta}$$

As with I_1, expanding the denominator as a binomial series

$$I_5 \simeq \int_{\phi}^{\psi} C_1 e^{A\theta}(\sin\theta+A\sin^2\theta+A^2\sin^3\theta+A^3\sin^4\theta+A^4\sin^5\theta$$

$$+A^5\sin^6\theta+A^6\sin^7\theta)d\theta$$

$$= \int_{\phi}^{\psi} C_1 e^{A\theta}\{\left(\frac{A}{2}+\frac{3A^3}{8}+\frac{5A^5}{16}\right)+\left(1+\frac{3A^2}{4}+\frac{5A^4}{8}+\frac{34A^6}{64}\right)\sin\theta$$

$$-\left(\frac{A}{2}+\frac{A^3}{2}+\frac{15A^5}{32}\right)\cos2\theta-\left(\frac{A^2}{4}+\frac{5A^4}{16}+\frac{21A^6}{64}\right)\sin3\theta$$

$$+\left(\frac{A^3}{8}+\frac{3A^5}{16}\right)\cos4\theta+\left(\frac{A^4}{16}+\frac{7A^6}{64}\right)\sin5\theta$$

$$-\frac{A^5}{32}\cos6\theta-\frac{A^6}{64}\sin7\theta\}d\theta$$

$$= \int_{\phi}^{\psi} C_1 e^{A\theta}(A_6+A_7\sin\theta-A_8\cos2\theta-A_9\sin3\theta+A_{10}\cos4\theta$$

$$+A_{11}\sin5\theta-A_{12}\cos6\theta-A_{13}\sin7\theta)d\theta$$

Again this gives the value of I_5 stated in section (4.2)

$$I_6 = C_2 \int_{\phi}^{\psi} \frac{\sin\theta d\theta}{1-A\sin\theta}$$

$$= C_2 \left\{\int_{\phi}^{\psi} \frac{d\theta}{A(1-A\sin\theta)} - \int_{\phi}^{\psi} \frac{d\theta}{A}\right\}$$

Using the half angle substitution as in I_3 then I_6 becomes:-

$$I_6 = \frac{C_2}{A}\left[\frac{2}{(1-A^2)^{\frac{1}{2}}}\tan^{-1}\left(\frac{\tan\frac{\theta}{2}-A}{(1-A^2)^{\frac{1}{2}}}\right) - \theta\right]_{\phi}^{\psi}$$

$$I_7 = \frac{A(\Lambda^2-P_1)}{(1+\Lambda^2)}\int_{\phi}^{\psi}\frac{\sin^2\theta\, d\theta}{1-A\sin\theta)}$$

$$= \frac{A(\Lambda^2-P_1)}{(1+\Lambda^2)}\left[\int_{\phi}^{\psi}\frac{d\theta}{A^2(1-\Lambda\sin\theta)} - \frac{1}{A}\int_{\phi}^{\psi}\sin\theta d\theta - \frac{1}{\Lambda^2}\int_{\phi}^{\psi}d\theta\right]$$

$$= \frac{(\Lambda^2-P_1)}{A(1+\Lambda^2)}\left[\frac{2}{(1-A^2)^{\frac{1}{2}}}\tan^{-1}\left(\frac{\tan\frac{\theta}{2}-A}{(1-A^2)^{\frac{1}{2}}}\right) + A\cos\theta-\theta\right]_{\phi}^{\Psi}$$

APPENDIX (4)

In calculating the film shape parameters A and ϕ, it is necessary to have some relationship between these quantities and values recorded from the capacitance displacement probes fitted to the pad.

If h_L and h_T are the mean values of displacement recorded between the two probes fitted near the leading edge and near the trailing edge respectively, then since:

$$h = c(1-A\sin\theta),$$

$$h_L = c(1-A\sin(\phi+\gamma))$$

and $$h_T = c(1-A\sin(\phi+\gamma+\alpha))$$

where γ is the position of the leading edge probe from the edge, and α is the angle between the probes, see fig (47), or

$$h_L = c\left[1-A(\sin\phi\cos\gamma+\cos\phi\sin\gamma)\right] \qquad \ldots\ldots\ldots\ldots\ldots\ldots(a)$$

and $$h_T = c\left[1-A(\sin\phi\cos(\gamma+\alpha)+\cos\phi\sin(\gamma+\alpha)\right] \qquad \ldots\ldots\ldots\ldots\ldots\ldots(b)$$

Let $B_1 = \cos(\gamma+\alpha)$ $\qquad$ $B_2 = \sin(\gamma+\alpha)$

$B_3 = \cos\gamma$ $\qquad$ and $\qquad$ $B_4 = \sin\gamma$

then eliminating A between (a) and (b);

$$\frac{h_T}{c} = 1 - \frac{D_1(B_1\sin\phi+B_2\cos\phi)}{(B_3\sin\phi+B_4\cos\phi)}$$

where $D_1 = 1 - \dfrac{h_L}{c}$

$$\text{or} \quad D_1 \frac{(B_1 \tan\phi + B_2)}{(B_3 \tan\phi + B_4)} = 1 - \frac{h_T}{c} = D_2$$

giving:

$$\phi = \tan^{-1} \left(\frac{D_2 B_4 - D_1 B_2}{D_1 B_1 - D_2 B_3} \right)$$

From (a)

$$A(B_3 \sin\phi + B_4 \cos\phi) = D_1$$

from which

$$A = \frac{D_1}{(B_3 \sin\phi + B_4 \cos\phi)}$$

The mean geometric clearance c_1 is:

$$c_1 = \frac{\int_\phi^\psi h d\theta}{(\psi - \phi)} = c \frac{\int_\phi^\psi (1 - A\sin\theta) d\theta}{(\psi - \phi)}$$

$$\text{therefore} \quad c_1 = c \left[1 + \frac{A(\cos\psi - \cos\phi)}{(\psi - \phi)} \right]$$

Now $\Lambda_c = \frac{6\mu\omega R^2}{p_a c^2} = \frac{\pi\mu R^2 N}{5 p_a c^2}$

for air at standard conditions, and with R = 1 in.

$$\Lambda_c = \frac{N}{923 \times 10^7} \left(\frac{R}{c} \right)^2$$

The above equations were used to relate the experimental and theoretical parameters.

Appendix (5)

"Analytical" Program.

The following A.L.G.O.L. computer program, was written to evaluate equations (40) and (36), for the plotting of the $\bar{W}$-X_p curves by the analytical method.

Like the program in appendix (6), it was written in a modified form, for operation on an I.C.T. 1909 digital computer.

The data should be presented in the following order:

δ, ψ-ϕ, N, LS, LINC, LNO, PS, PINC, PNO, A_1, A_2, A_3,---A_n,

Where we have:

δ - limit of convergence on the mean dimensionless pressure P_1

$\psi - \phi$ - in degrees,

N - number of values of A to be read i.e., 1 to n,

LS - starting value of Λc,

LINC - increment in Λc,

LNO - number of values of Λc to be computed

PS - starting value for ϕ

PINC - increment in ϕ

PNO - number of values of ϕ to be computed.

Program.

```
BEGIN REAL DELTA,SPAND,LS,LINC,PS,PINC,PHI,PSI,L,NEWPM,C1,C2,B1,B2,
      B3,B4,B5,B6,B7,B8,B9,B10,B11,B12,B13,T,I,IA,IB,OLDPM,TI,SPAN,
      RAD;
      INTEGER N,LNO,PNO,K,E,F,Y;
      DELTA:=READ;   SPAND:=READ;   N:=READ;   LS:=READ;  LINC:=READ;
      LNO:=READ;   PS:=READ;   PINC:=READ;   PNO:=READ;
      BEGIN ARRAY A[1:N],  LC[1:N,1:LNO+1],   PHID,WB,X[1:N,1:LNO+1,
      1:PNO+1];
           FOR K:=1 STEP 1 UNTIL N DO A[K]:=READ;
           FREE INPUT;
           RAD:=360/6.28318;   SPAN:=SPAND/RAD;
           FOR K:=1 STEP 1 UNTIL N DO
           BEGIN B1:=1+A[K]↑2/4+A[K]↑4/8;   B2:=A[K]/2+A[K]↑3/4;
                 B3:=A[K]↑2/4+3×A[K]↑4/16;   B4:=A[K]↑3/8;
                 B5:=A[K]↑4/16;   B6:=A[K]/2+3×A[K]↑3/8+5 A[K]↑5/16;
                 B7:=1+3×A[K]↑2/4+5×A[K]↑4/8+35×A[K]↑6/64;
                 B8:=A[K]/2+A[K]↑3/2+15×A[K]↑5/32;
                 B9:=A[K]↑2/4+5×A[K]↑4/16+21×A[K]↑6/64;   B10:=A[K]↑
                 3/8+3×A[K]↑5/16;
                 B11:=A[K]↑4/16+7×A[K]↑6/64;   B12:=A[K]↑5/32;
                 B13:=A[K]↑6/64;
                 LC[K,1]:=LS;
                 FOR E:=1 STEP 1 UNTIL LNO DO
                 BEGIN PHID[K,E,1]:=PS;
                      FOR F:=1 STEP 1 UNTIL PNO DO
                      BEGIN PHI:=PHID[K,E,F]/RAD;   PSI:=PHI+SPAN;
                           L:=IC[K,E]/((1+A[K]×(COS(PSI)-COS(PHI))
                           /(PSI-PHI))↑2);
                           NEWPM:=0;
                           L3:C1:=A[K]/((1+L↑2)×(EXP(L×PHI)-EXP(L×
                           PSI)))
                           ×((L↑2-NEWPM)×(SIN(PSI)-SIN(PHI))+L×(1+NEWPM)
                           ×(COS(PSI)-COS(PHI)));
                           C2:=A[K]/((1+L↑2)×(EXP(L×PSI)-EXP(L×PHI)))
                           ×(EXP(L×PHI)×((L↑2-NEWPM)×SIN(PSI)+L×(1+NEW
                           PM)×COS(PSI))
                           -EXP(L×PSI)×((L↑2-NEWPM)×SIN(PHI)+L×(1+NEW
                           PM)×COS(PHI)));
                           T:=PSI;   Y:=1;
```

```
L1:I:=C1×(EXP(L×T)×(B1/(L↑2+1)×(L×COS
(T)+SIN(T))
+B2/(L↑2+4)×(L×SIN(2×T)-2×COS(2×T))
-B3/L↑2+9)×(L×COS(3×T)+3×SIN(3×T))
-B4/L↑2+16)×(L×SIN(4×T)-4×COS(4×T))
+B5/(L↑2+25)×(L×COS(5×T)+5×SIN(5×T))))
-C2/A[K]×LN(1-A[K]×SIN(T))-L×(1+NEWPM)/A
[K]/(1+L↑2)×
(2×SQRT(1-A[K]↑2)×ARCTAN((SIN(T/2)/COS
(T/2)-A[K])/SQRT(1-A[K]↑2))
+A[K]×COS(T)-T)-(L↑2-NEWPM)×(A[K]×SIN
(T)+LN(1-A[K]×SIN(T)))/A[K]/(1+L↑2);
IF Y=1 THEN
BEGIN IA:=I;    Y:=2;    T:=PHI;
      GOTO L1;
END;
IA:=IA-I;
T:=PSI;    Y:=1;
L2:I:=CI×(EXP(L×T)×(B6/L+B7/(L↑2+1)
(L×SIN(T)-COS(T))
-B8/(L↑2+4)×(L×COS(2×T)+2×SIN(2×T))
-B9/(L↑2+9)×(L×SIN(3×T)-3×COS(3×T)
+B10/L↑2+16)×(L×COS(4×T)+4×SIN(4×T))
+B11/(L↑2+25)×(L×SIN(5×T)-5×COS(5×T))
-B12/(L↑2+36)×(L×COS(6×T)+6×SIN(6×T))
-B13/(L↑2+49)×(L×SIN(7×T)-7×COS(7×T))))
+C2×(2/SQRT(1-A[K]↑2)×ARCTAN((SIN(T/2)/
COS(T/2)-A[K])/SQRT(1-A[K]↑2))-
T)/A[K];L×(1+NEWPM)×(A[K]×SIN(T)+LN(1-
A[K]×SIN(T)))/
A[K]/(1+L↑2)↑(L↑2-NEWPM)/A[K]/(1-L↑2)
×(2/SQRT/1-A[K]↑2)×
ARCTAN((SIN(T/2)/COS(T/2)-A[K])/SQRT
(1-A[K]↑2))+A[K]×COS(T)-T;
IF Y=1 THEN
BEGIN IB:=I;    Y:=2;    T:=PHI;
      GOTO L2;
END:
IB:=IB-I;
WB[K,E,F]:=SQRT(IA↑2+IB↑2);
OLDPM:=NEWPM;    NEWPM:=WB[K,E,F]/SPAN
IF NEWPM-OLDPM>DELTA THEN GOTO L3;
T1:=ARCTAN(IB/IA);
X[K,E,F]:=(TI;PHI)/SPAN;
PHID[K,E,F+1]:=PHID[K,E,F]+PINC;
```

```
                    END;
                    LC|K,E+1|:=LC|K,E|+LINC;
               END;
          END;
          FOR K:=1 STEP 1 UNTIL N DO
          BEGIN WRITE TEXT('('P' G.PITTS ANALYTICAL␣VALUES␣FOR
          ␣W␣BAR-PIVOT␣GRAPH(3C)DELTA(5S)SPAN(6S)A(1C)));
               PRINT(DELTA,1,4);  PRINT (SPAND,3,2);   SPACE(2);
               PRINT (A[K],1,4);
               WRITE TEXT('('4C)LAMBDA(4S)PHI(7S)X(9S)W␣BAR(2C)));
               FOR E:=1 STEP 1 UNTIL LNO DO
               BEGIN PRINT(LC[K,E],2,2);   NEW LINE (1);
                    FOR F:=1 STEP 1 UNTIL PNO DO
                    BEGIN SPACE(9);   PRINT(PHID[K,E,F],3,2);
                         PRINT (X[K,E,F],1,3);
                         SPACE(1);   PRINT (WB[K,E,F],2,5);
                         NEW LINE(1);
                    END;
               END;
          END;
     END;
END;
```

PROGRAM.

```
BEGIN REAL DELTA,SPAND,LS,LINC,PS,PINC,A,RAD,SPAN,GRID,PHID,B,INC,
PN,T,OLDB,PSNTOT,PCSTOT,PSN,PCS,THETA;
INTEGER Z,MESH,N,LNO,PNO,K,E,F,J,M;
L9:DELTA:=READ;   MESH:=READ;   SPAND:=READ;   N:=READ;   LS:=READ;
LINC:=READ;
LNO:=READ;  PS:=READ;   PINC:=READ;   PNO:=READ;   M:=READ;
BEGIN ARRAY A[1:N],LC[1:N,1:LNO+1],W,X,PSI,PHI,PHID[1:N,1:LNO+1,
1:PNO+1],P,PSN,PCS[0:MESH];
FOR K:=1 STEP 1 UNTIL N DO A[K]:=READ;
RAD:=360/6.28318;   SPAN:=SPAND/RAD;   GRID:=SPAN/MESH;
FOR K:=1 STEP 1 UNTIL N DO
BEGIN LC[K,1]:=LS;
     FOR E:=1 STEP 1 UNTIL LNO DO
     BEGIN PHID[K,E,1]:=PS;
          FOR F:=1 STEP 1 UNTIL PNO DO
          BEGIN PHI[K,E,F]:=PHID[K,E,F]/RAD;
               PSI[K,E,F]:=PHI[K,E,F]+SPAN;
               Z:=0;   B:=0;   INC:=1;
               L1: P[0]:=0;   PN:=1;   T:=PHI[K,E,F];   Z:=Z+1;
               FOR J:=1 STEP 1 UNTIL MESH DO
               BEGIN P[J]:=LC[K,E]×GRID×(PN×(1-A[K]×SIN(T))+B)/(PN
               ×(1-A[K]×SIN(T))↑3)+P[J-1];
                    IF P[J]<-1 THEN
                    BEGIN INC:=INC/2;   B:=OLDB+INC;
                         GOTO L1;
                    END;
                    T:=T+GRID;
                    PN:=P[J]+1;
               END;
               IF Z>M THEN BEGIN
               W[K,E,F]:=100;   X[K,E,F]:=100;   GOTO L5;
               END;
               IF P[MESH]>DELTA THEN
               BEGIN OLDB:=B;   B:=B+INC;
                    GOTO L1
               END;
               IF P[MESH]<0 THEN
               BEGIN INC:=INC/2;  B:=OLDB+INC;
                    GOTO L1;
               END;
               PSNTOT:=PCSTOT:=0;   T:PHI[K,E,F];
```

```
                    FOR J:=0 STEP 1 UNTIL MESH DO
                    BEGIN PSN[J]:=P[J]×SIN(T);    PCS[J]:=P[J]×COS(T);
                          T:=T+GRID;
                    END;
                    FOR J:=0 STEP = UNTIL (MESH-2) DO
                    BEGIN PSNTOT:=PSNTOT+GRID×(PSN[J]+4×PSN[J+1]+PSN[J+2])/3;
                          PCSTOT:=PCSTOT+GRID×(PCS[J]+4×PCS[J+1]+PCS[J+2])/3;
                    END;
                    THETA:=ARCTAN(PSNTOT/PCSTOT);
                    X[K,E,F]:=(THETA-PHI[K,E,F])/SPAN;
                    W[K,E,F]:=SQRT(PSNTOT↑2+PCSTOT↑2);
                    L5:PHID[K,E,F+1]:=PHID[K,E,F]+PINC
               END;
               LC[K,E+1]:=LC[K,E]+LINC;
          END;
     END;
     WRITE TEXT('('P')G.PITTS.VALUES␣FOR␣W␣BAR-PIVOT␣POSITION␣GRAPH␣BY␣
     FINITE␣DIFFERENCE'3C')
     DELTA'7S'MESH'8S'SPAN'C'));
     PRINT(DELTA,1,5);    SPACE(2);    PRINT(MESH,3,0);    SPACE(7);
     PRINT(SPAND,3,1);    NEWLINE(2);
     WRITE TEXT('('A'9S'LAMBDA'5S'PHI'8S'W␣BAR'5S'PIVOT␣POSITION'2C'));
     FOR K:=1 STEP 1 UNTIL N DO
     BEGIN FOR E:=1 STEP 1 UNTIL LNO DO
          BEGIN FOR F:=1 STEP 1 UNTIL PNO DO
               BEGIN PRINT(A[K],1,4);    SPACE(1);    PRINT(LC[K,E],3,1);
               SPACE(6);
                    PRINT(PHID[K,E,F],3,1);    PRINT(W[K,E,F],3,4) SPACE(1);
                    PRINT(X[K,E,F],0,4);
                    NEW LINE(1)
               END;
          END;
     END;  FREE OUTPUT;
     END; GOTO L9;
END;
```

APPENDIX (6)

"Numerical" Program.

This program is written to derive the $\bar{W}$-X_p curves by "numerical" means. A backward difference method is employed for the integration of equation (43), and a flow diagram for the evaluation of B_1 is shown in figure (6).

The data should be presented in the following order:

δ,MESH,$\psi-\phi$,N,LS,LINC,LNO,PS,PINC,PNO,M,A_1,A_2,A_3,---A_n,

where δ,$\psi-\phi$,N,LS,LINC,LNO,PS,PINC, PNO, and A, are explained in appendix (5), and the following are:

MESH - the number of mesh points taken around the circumference of the pad.

M - the maximum number of iterations considered worthwhile for obtaining B_1.

The program is designed to read in any number of sets of data without further instructions, provided the results are given for the previous set of data first. The input is usually terminated by a stop instruction.

References.

1. Hirn, G. 'Study of the Principal phenomena shown by Friction and of Various Methods of determining the viscosity of lubricants' Bull. Soc. Industr Mulhouse 26, No. 129 (1854).

2. Kingsbury, A. Experiments with an Air Lubricated Bearing J. Amer. Soc. nav Engrs 9 (1897) 267.

3. Ferranti. An Internal Memorandum from A. J. Munday, Dept. of Mech. Eng. The University, Southampton.

4. Pitts, G. Pivoted Pad Bearings. Paper (4b) Symposium on Gas Lubrication 1965, University of Southampton.

5. Snell, L. N. 'Pivoted-Pad Journal Bearings Lubricated by Gas" IGR-R/CA-285 1958 U.K.A.E.A. Industrial Group.

6. Marsh, H. Stability of Aerodynamic Gas Bearings Mechanical Engineering Science Monograph No. 2, I.Mech.E. June 1965.

7. Burgdorfer, A. 'The Influence of the Molecular Mean Free Path on the Performance of Hydrodynamic Gas Lubricated Bearings'. J. Basic Eng. Trans A.S.M.E. 81, 1959.

8. Powell, J.W. The Gas-Behaviour and Load Capacity of Hydrodynamic Gas Journal Bearings. Ph.D. Thesis 1963, Mechanical Eng. The University, Southampton.

9. Curle, N. Laminar Boundary Layer Equations. Oxford Mathematical Monographs O.U.P. 1962.

10. Brand, R.S. 'Inertia Forces in Lubricating Films' J. App.Mech., 22, 1955.

11. Ausman J. S. Finite Gas Lubricated Journal Bearing I.Mech.E. Proceeding of the Conference on Lubrication and Wear 1957.

12.	Ausman, J. S.	An Improved Analytical Solution for Self-Acting Gas-Lubricated Journal Bearings of Finite Length. A.S.M.E. Paper No. 60-Lub-9.
13.	Ausman, J. S.	'Gas Lubricated Bearings' chapter, Advanced Bearing Technology Eds Bisson and Anderson, NASA SP-38 1964.
14.	Katto, Y. Soda, N.	Theory of Lubrication by Compressible Fluid With Special Reference to Air Bearing. 2nd Japan National Congress for Applied Mechanics 1952.
15.	Gross, W. A.	Gas Film Lubrication. John Wiley & Sons, New York, 1962.
16.	Pitts, G.	An Analytical Study of the Tilting Pad Gas Lubricated Journal Bearing. Proc. I.Mech.E. 1966-7 Vol. 181 part 1.
17.	Gunter, E. J. Hinkle, J. G. & Fuller, D. D.	'The Effects of Speed, Load, and Film Thickness on the Performance of Gas-Lubricated, Tilting-Pad Journal Bearings. A.S.L.E. Trans., Vol. 7, No. 4, 1964.
18.	National Physical Laboratory.	'Modern Computing Methods' Notes on Applied Science. H.M.S.O. London, 1961.
19.	Gunter, E. J. Hinkle, J. G. & Fuller, D. D.	Design Guide for Gas-Lubricated Tilting-Pad Journal and Thrust Bearings With Special Reference to High Speed Rotors NYO-2512-1. The Franklin Institute Nov. 1964.
20.	Wayne-Kerr Laboratories Ltd.	Instruction Manual for the B731A Vibration Meter.
21.	Castelli, V., Stevenson, C. H. & Gunter, E. J.	Steady State Characteristics of Gas-Lubricated, Self-Acting, Partial-Arc, Journal Bearings of Finite Width. Franklin Institute Report I-A2049-18 1963.
22.	Abramowitz, S.	Turbulence in a Tilting Pad Thrust Bearing. A.S.M.E. Trans (78) 1-6 (1956).

23. Gunter, E. J. The Influence of Lubricant Compressibility on the Performance of the 120° Partial Journal Bearing. A.S.M.E. paper No. 66-WA/Lub 2.

List of Figures.

1. The tilting pad bearing.
2. Coordinate system for a fluid film (in the text)
3. Diagram to illustrate the angle β
4. Coordinate system for a single pad
5. Axial pressure distribution for a finite and infinite pad
6. Flow diagram for evaluating B_1
7. Graph of B_1, illustrating numerical instability
8. $\bar{W} - X_p$ design curves for $H_m = .2$
9. " " " " $H_m = .3$
10. " " " " $H_m = .4$
11. " " " " $H_m = .5$
12. " " " " $H_m = .6$
13. Comparison of numerical and analytical design curves
14. Curves for the study of the group $(p_a c_1^2)$
15. $I_Y - L/R$ curves for end-flow correction
16. Theoretical pressure profiles (P_1 = mean pressure)
17. " " " ($P_1 = 0$)
18. Numerical pressure profiles (ref 17) (circumferential)
19. " " " " (axial)
20. Sectioned diagram of rig.
21. Sectioned diagram of cross-slide
22. Photograph of rig (general)

23. Photograph of shaft

24. " " pad

25. " " capacitance probe

26. " " nozzles

27. Sectioned diagram of a test pad

28. Line diagram of the jacking and pressure recording system

29. Capacitance probe calibration curve

30. Layout of pressure tapping holes

31. Experimental & theoretical pressure distribution at Y = 0.20 $\Lambda c = 1.232$

32. Axial pressure distribution $\Lambda c = 1.232$

33. Experimental & theoretical pressure distribution $\Lambda c = 5.3$

34. Power loss due to viscous drag

35. Power loss due to pad tilt

36. Loss due to pad tilt (in the text)

37. The effect of friction on the radial pivot position (in the text)

38. $\overline{W} - X_p$ curve for obtaining stiffness

39. Load - Pivot Clearance Curves

40. The effect of H_m on film shape

41. Curve for example (2)

42. Curves for example (3)

43. " " " (4)

44. " " " (5)

45. $\overline{W} - X_p$ curves as $\Lambda c \to \infty$

46. Graph to illustrate the effect of C_5 (appendix 2)

47. Capacitance probe positions (appendix 4)

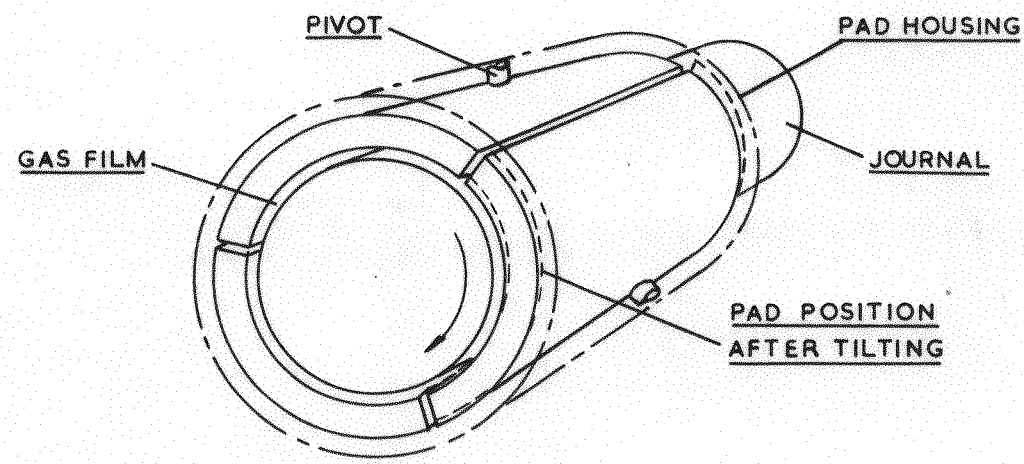

FIG.I. THE TILTING PAD BEARING

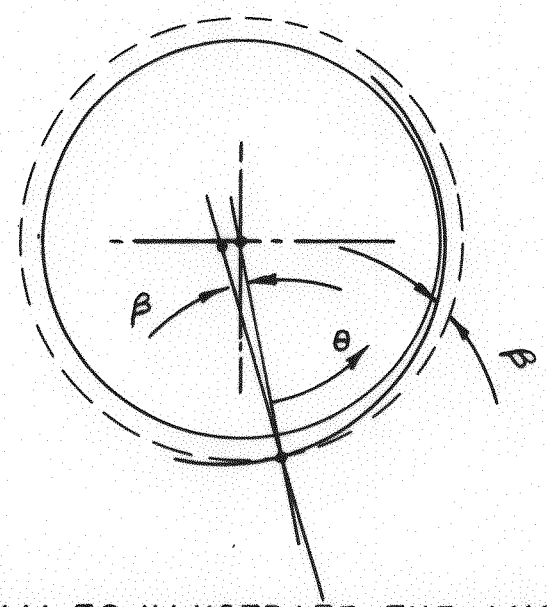

FIG.3. DIAGRAM TO ILLUSTRATE THE ANGLE β

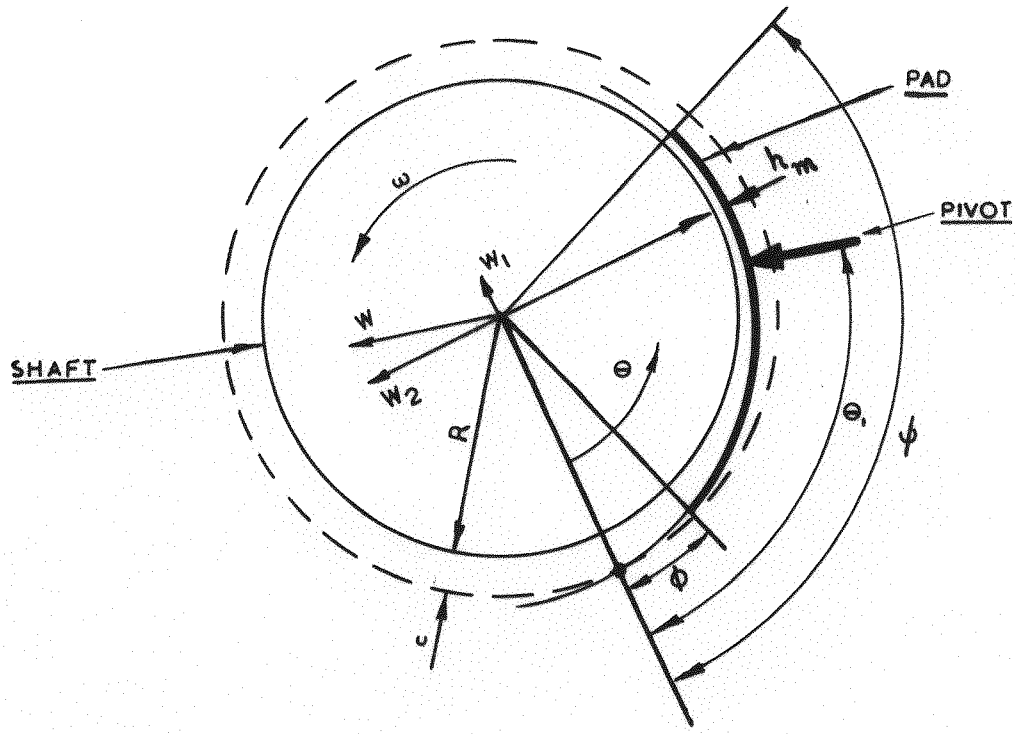

FIG.4. COORDINATE SYSTEM FOR A SINGLE PAD

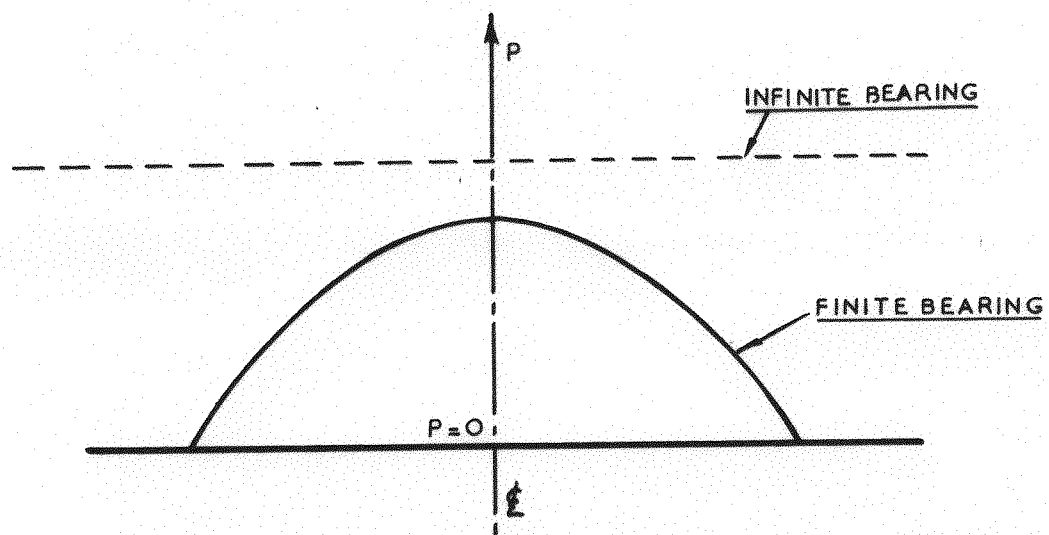

FIG.5. AXIAL PRESSURE DISTRIBUTION FOR A FINITE & INFINITE PAD

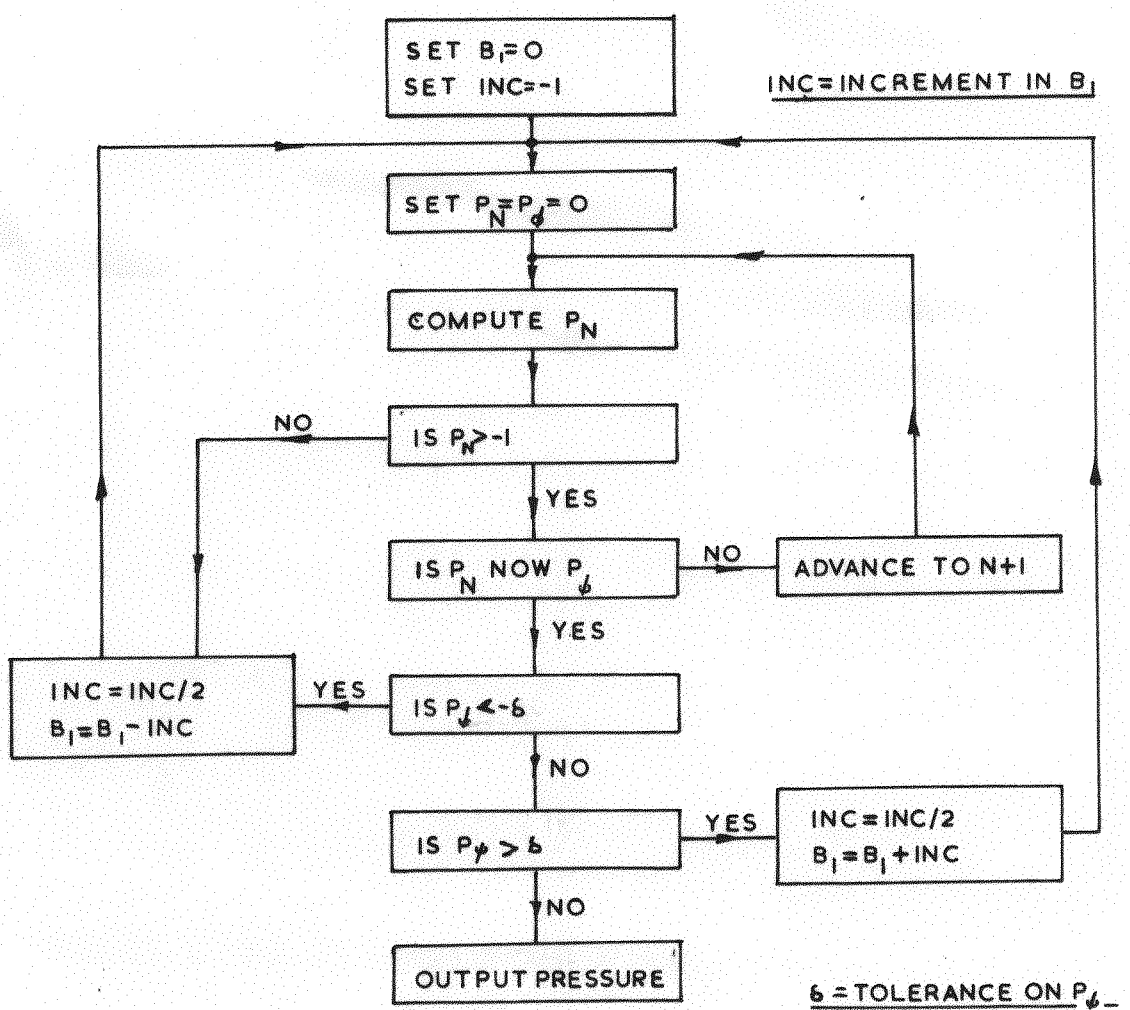

FIG.6. FLOW DIAGRAM FOR EVALUATING B_1

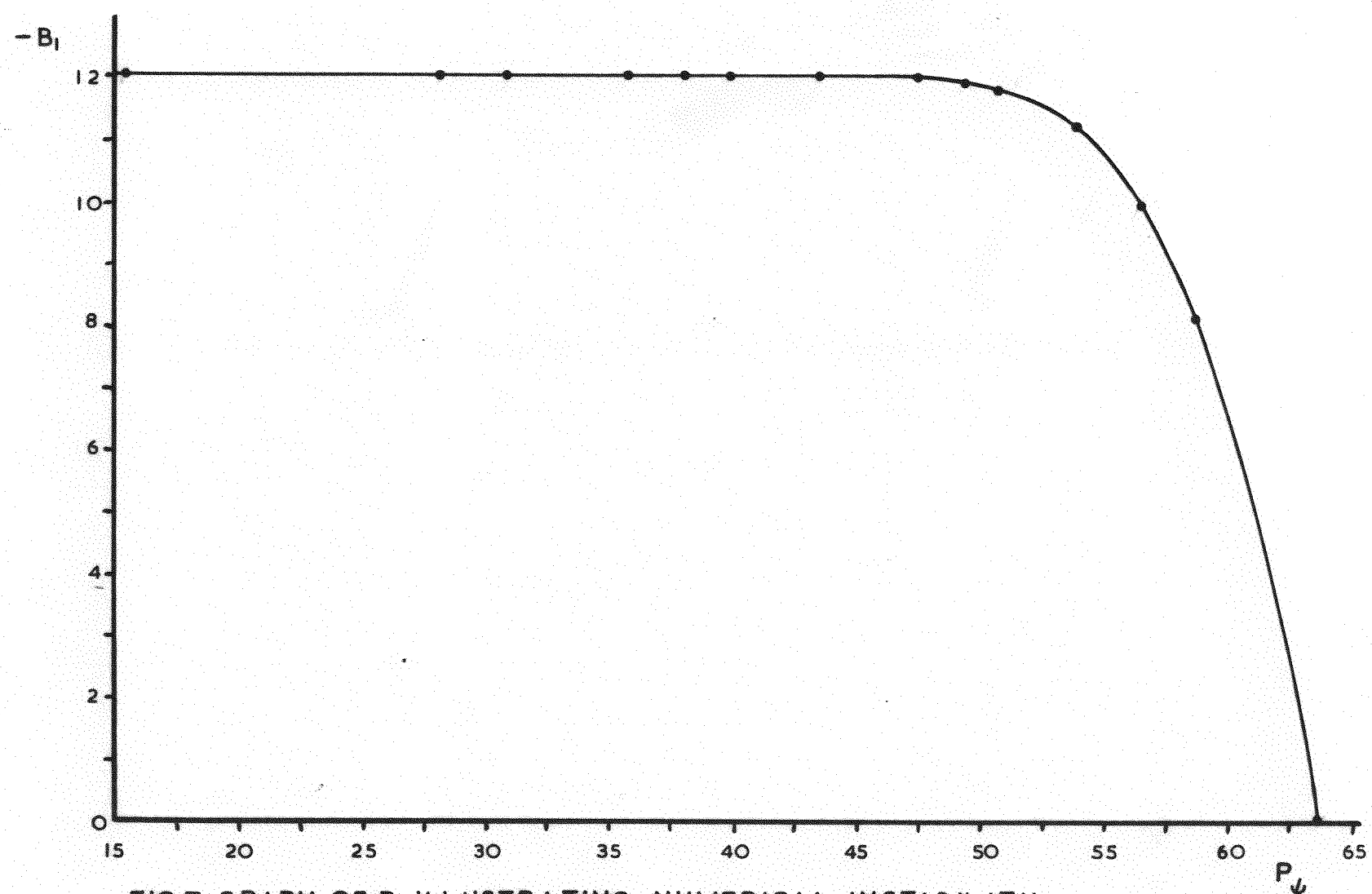

FIG.7. GRAPH OF B_1 ILLUSTRATING NUMERICAL INSTABILITY

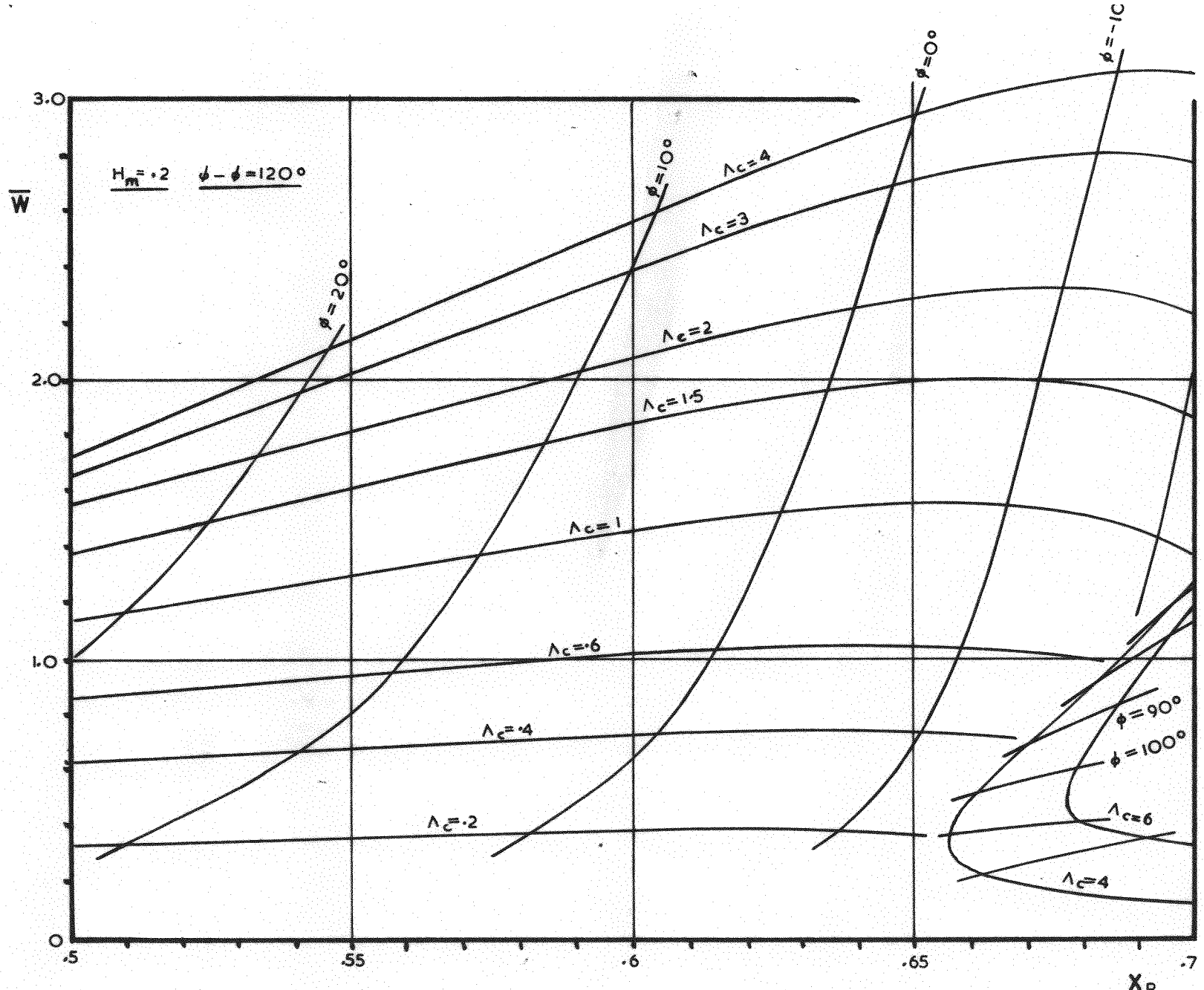

FIG.8. TILTING PAD GAS JOURNAL BEARING DESIGN CURVES $H_M = .2$

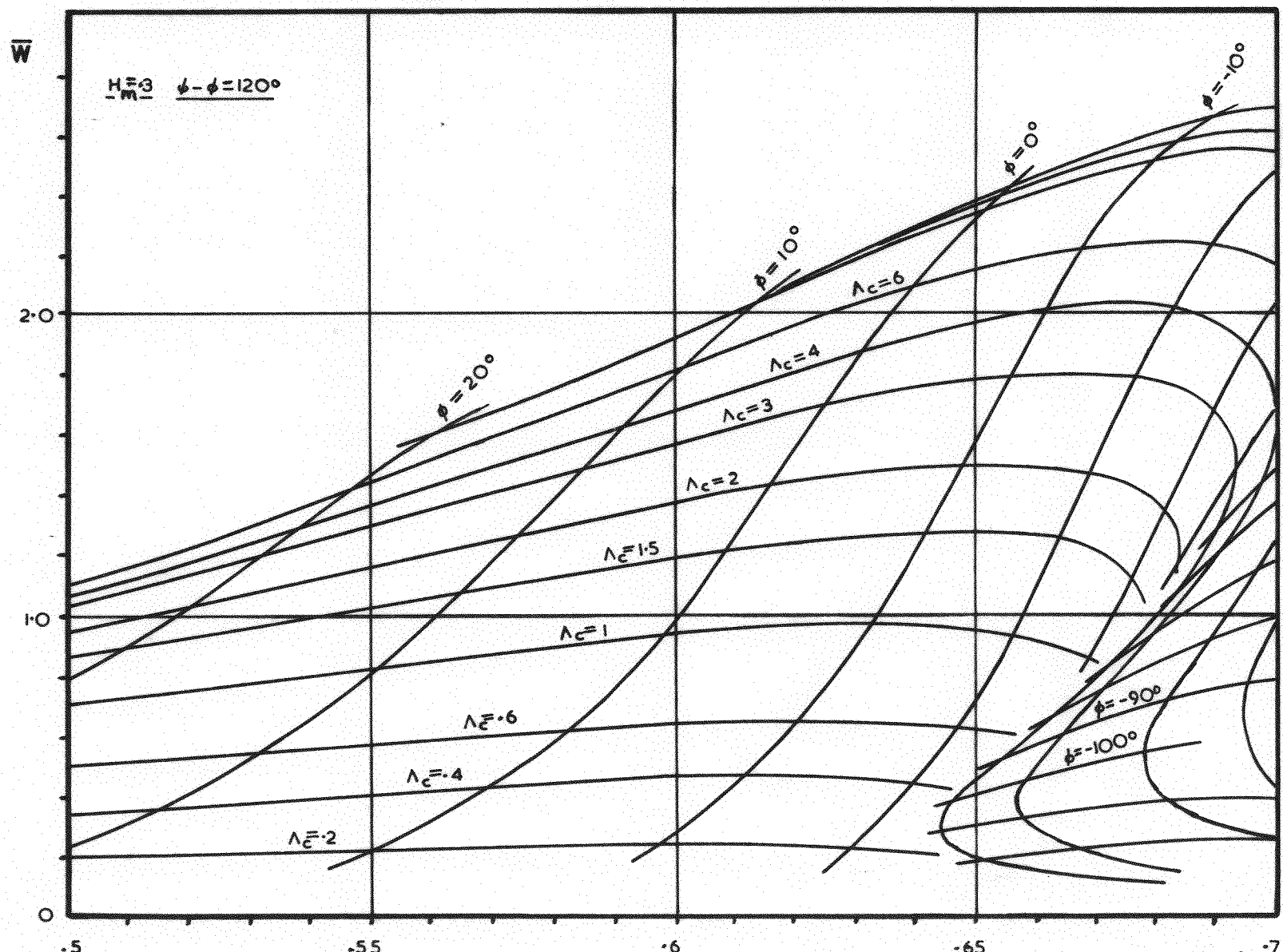

FIG.9. TILTING PAD GAS JOURNAL BEARING DESIGN CURVES $H_M = 3$

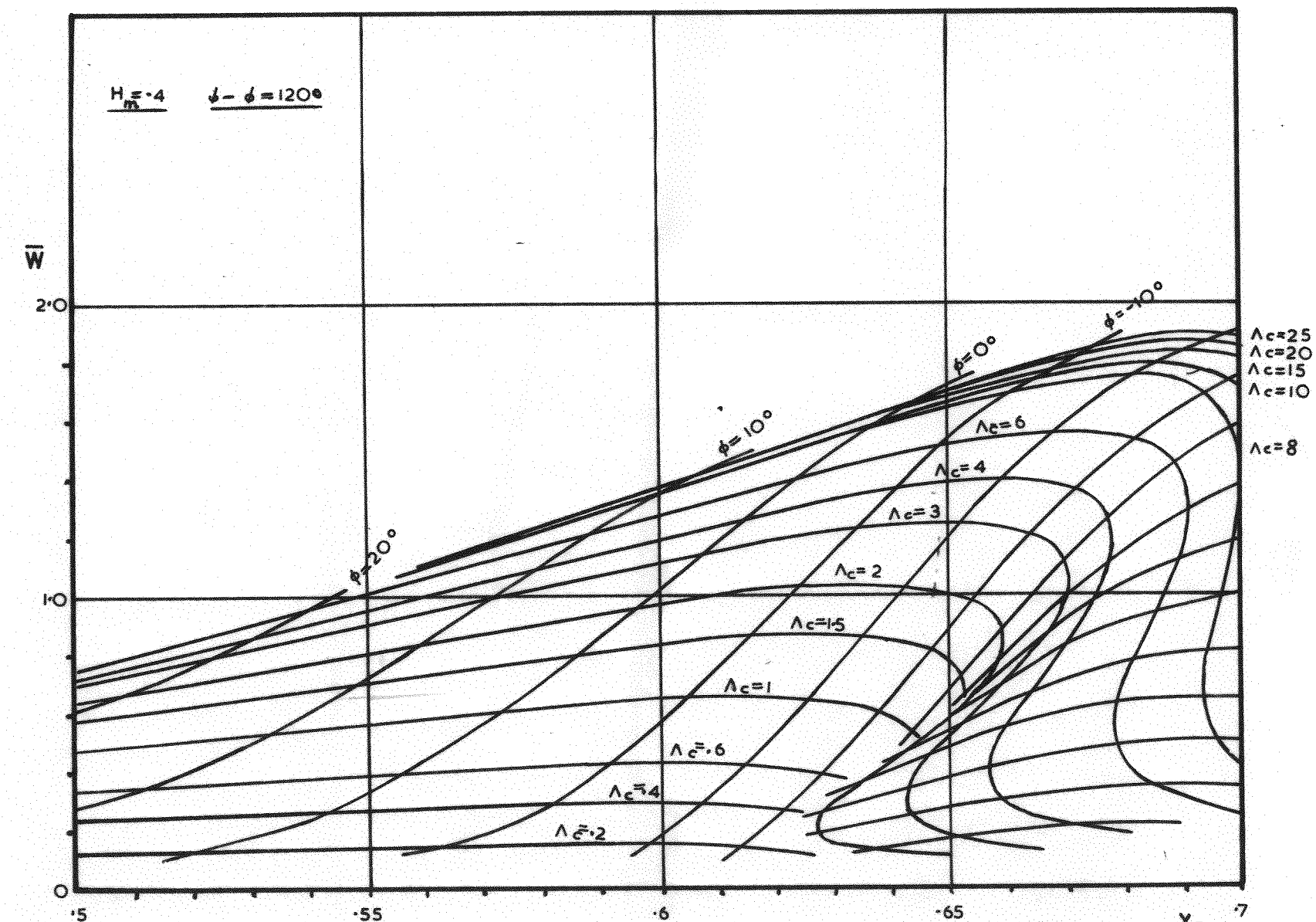

FIG.10. TILTING PAD GAS JOURNAL BEARING DESIGN CURVES $H_M = \cdot 4$

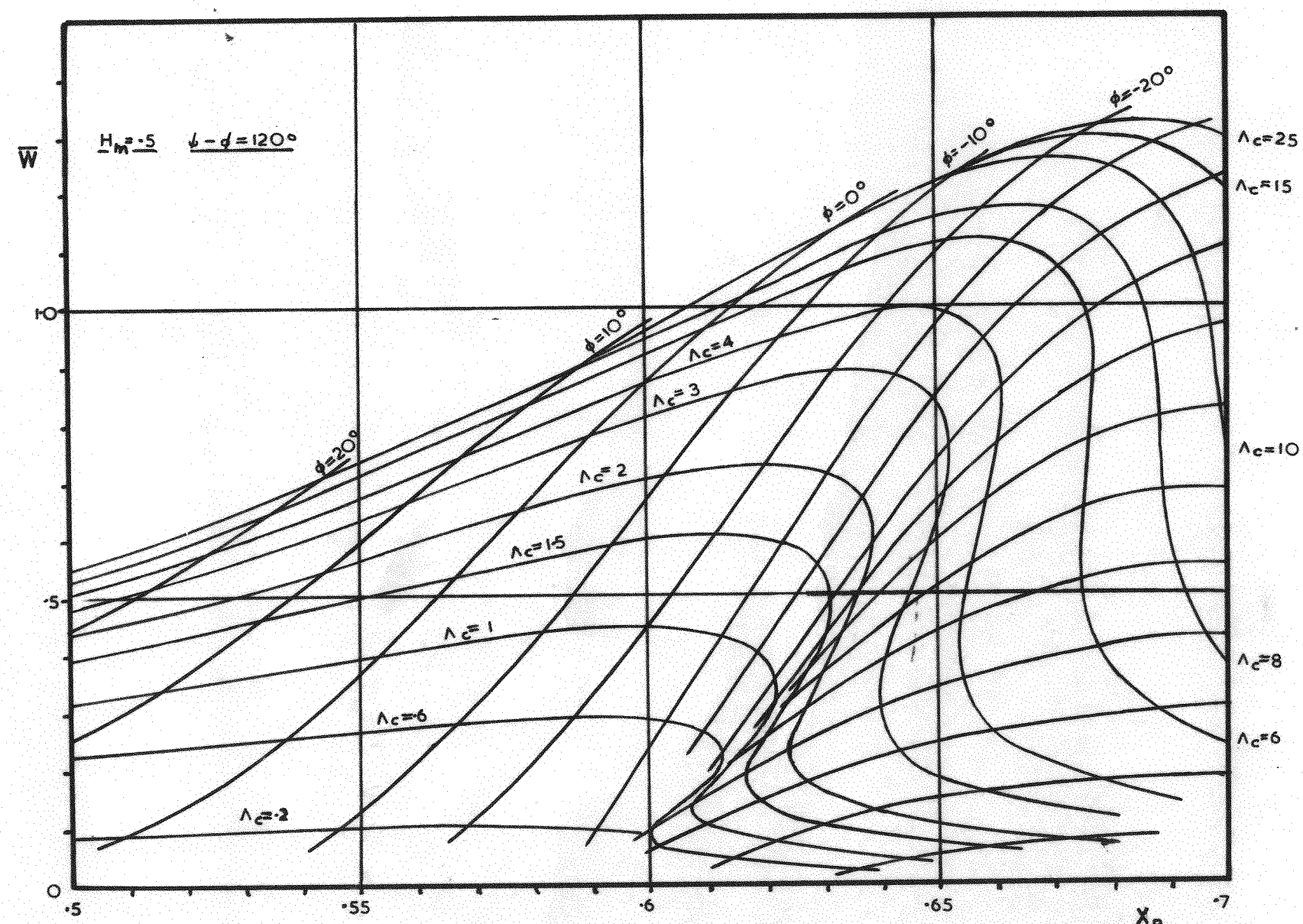

FIG.11. TILTING PAD GAS JOURNAL BEARING DESIGN CURVES H_M=·5

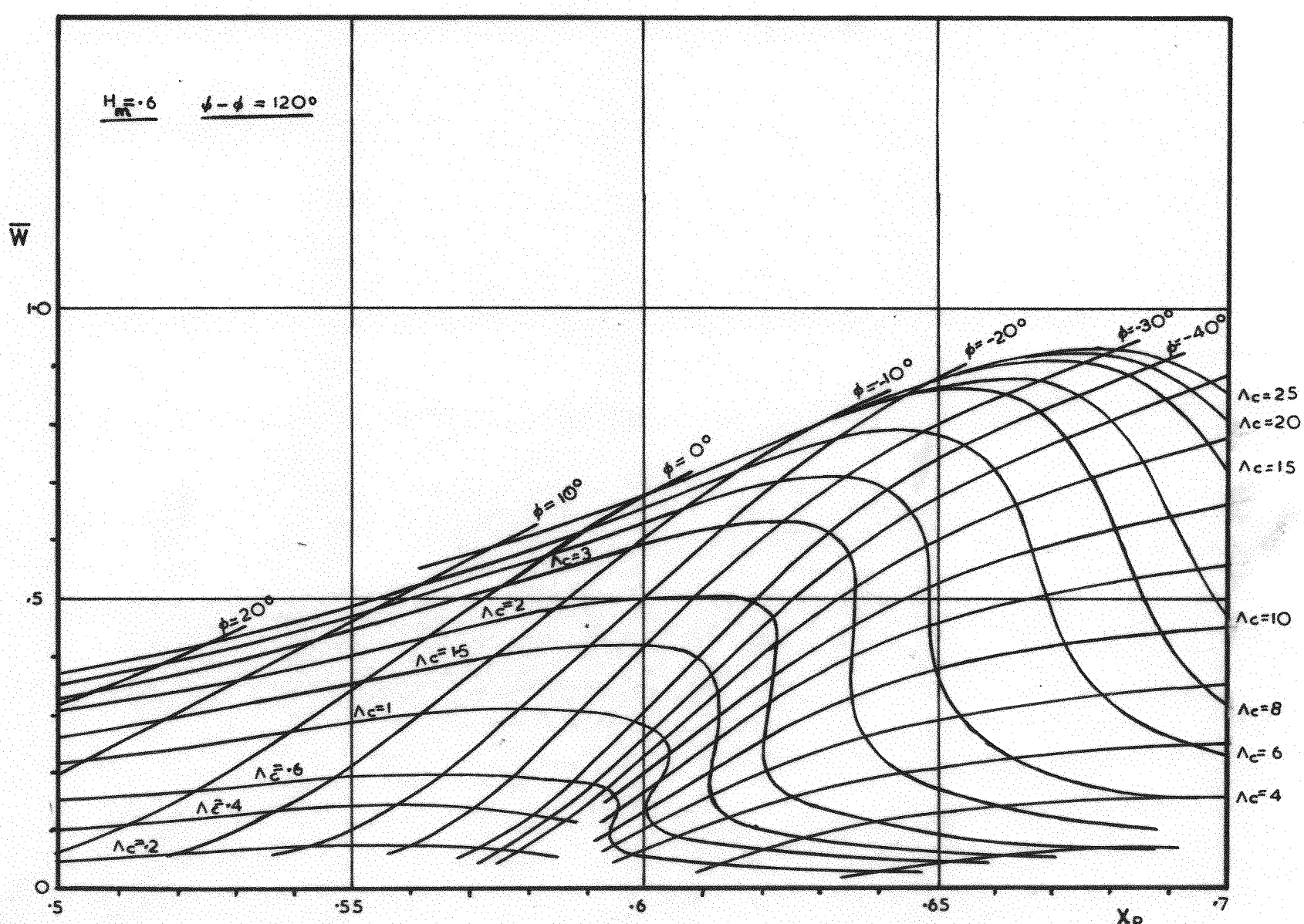

FIG. 12. TILTING PAD GAS JOURNAL BEARING DESIGN CURVES $H_m = \cdot 6$

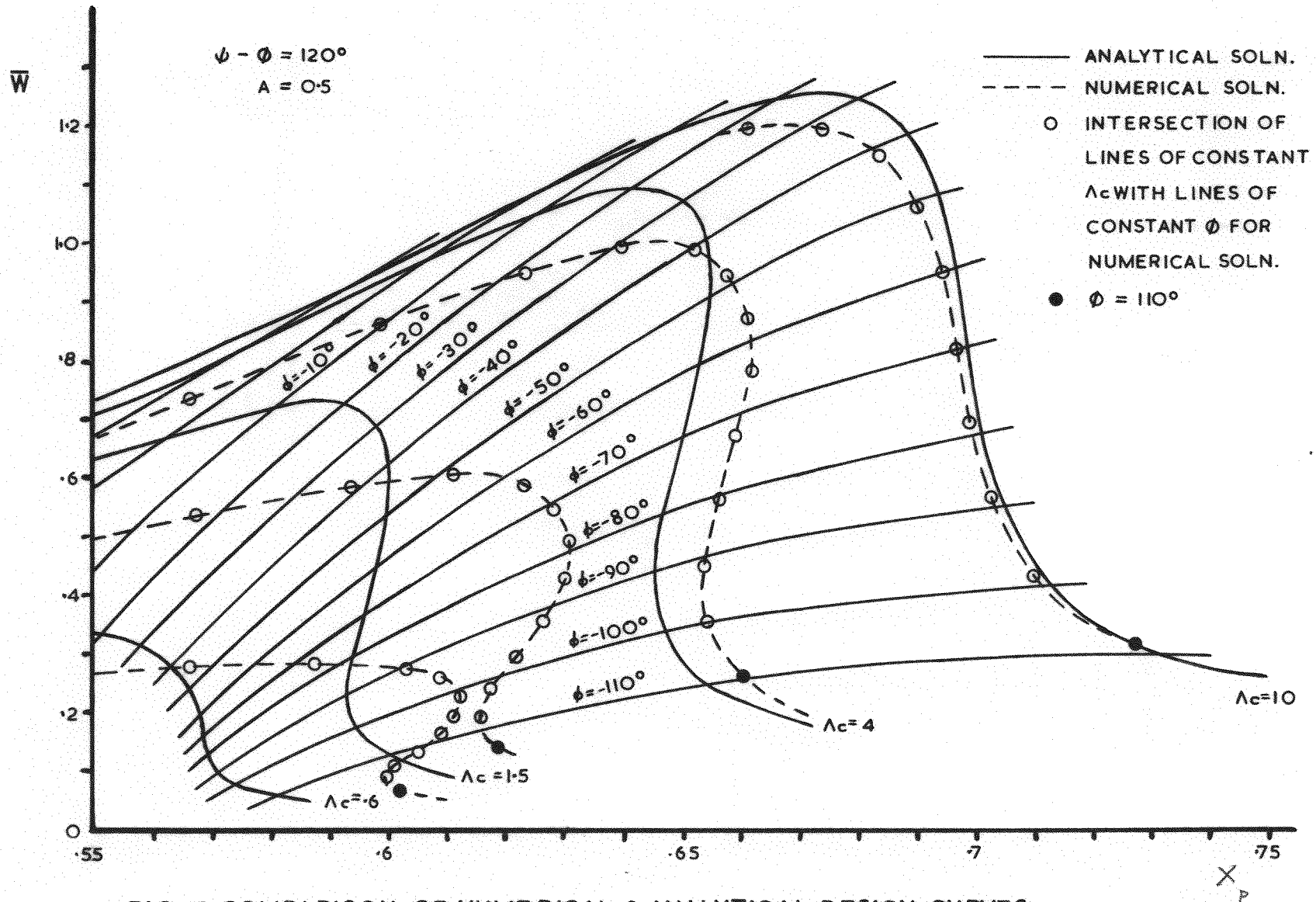

FIG.13. COMPARISON OF NUMERICAL & ANALYTICAL DESIGN CURVES

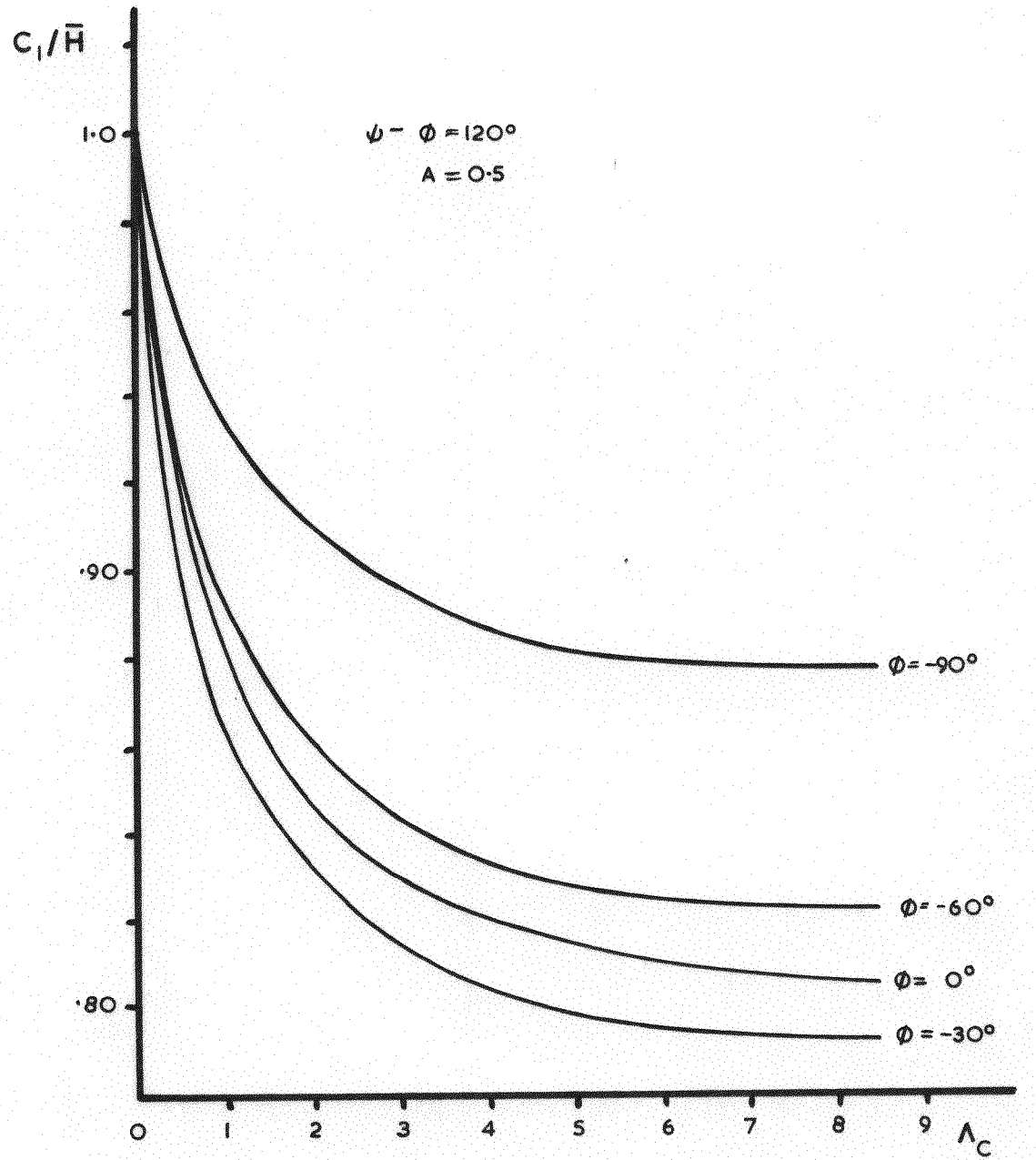

FIG. 14. CURVES FOR THE STUDY OF THE GROUP $P_A C_1^2$

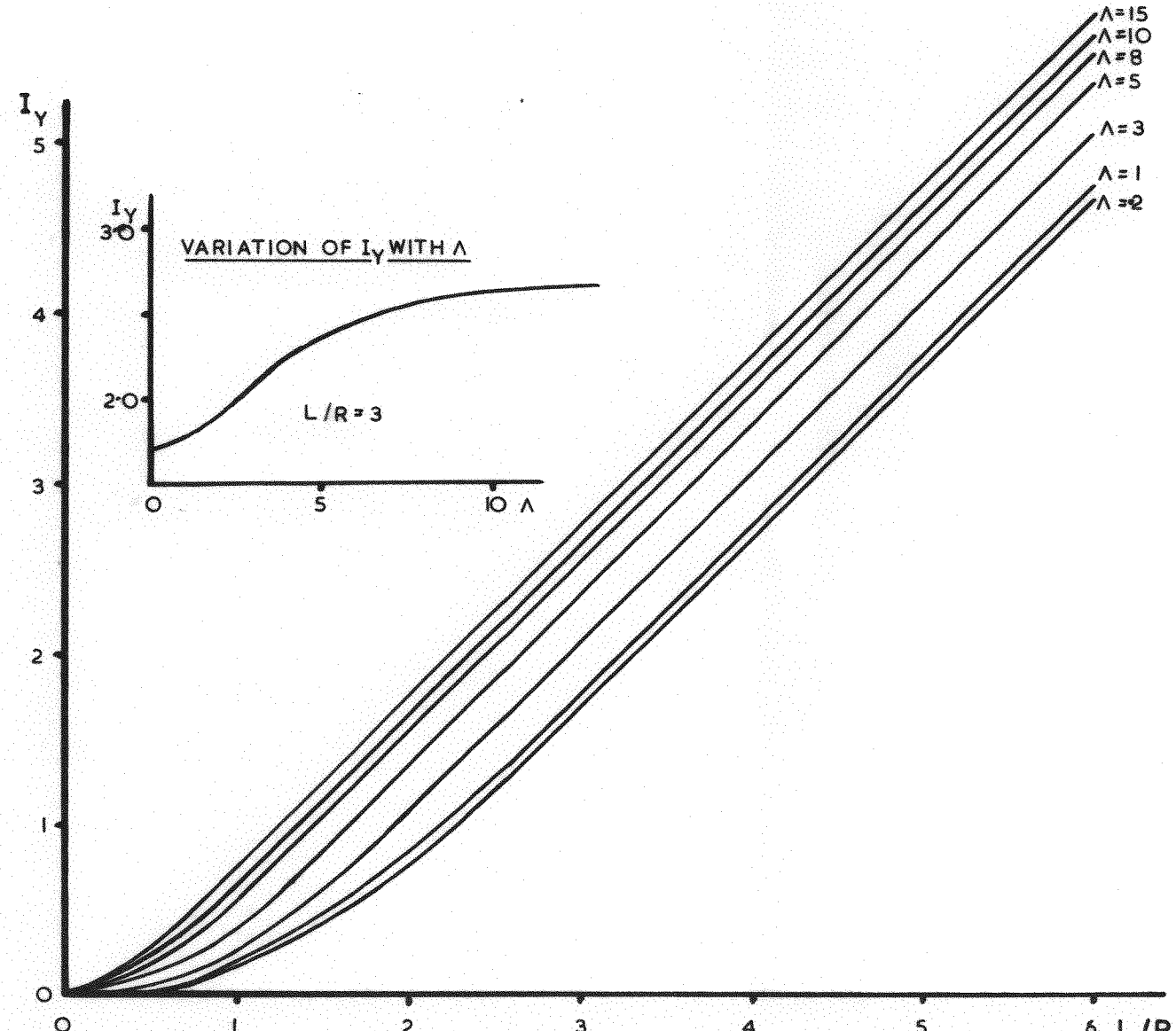

FIG.15. I_Y - L/R CURVES FOR END FLOW CORRECTION

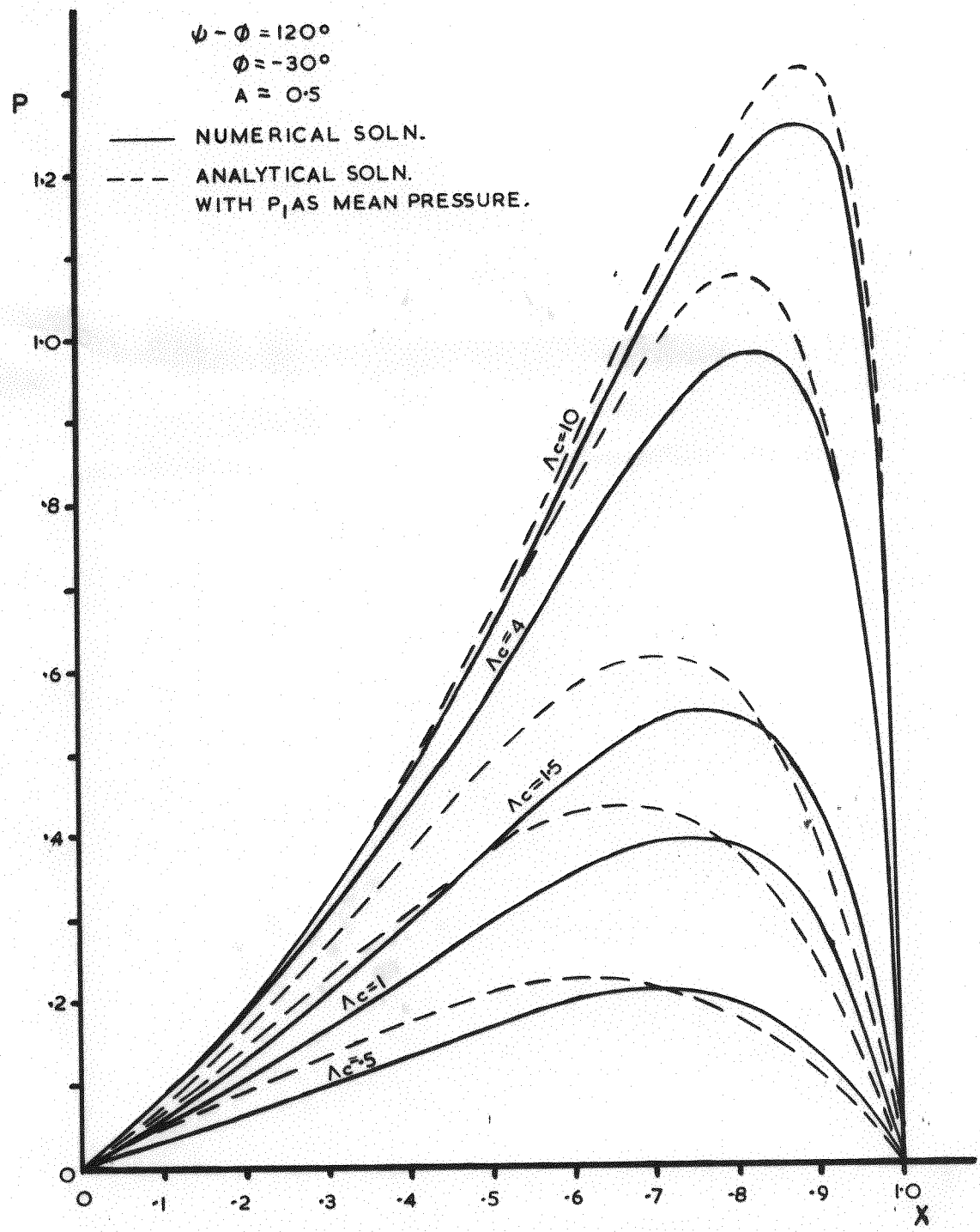

FIG.16. THEORETICAL PRESSURE PROFILES FOR AN INFINITE PAD

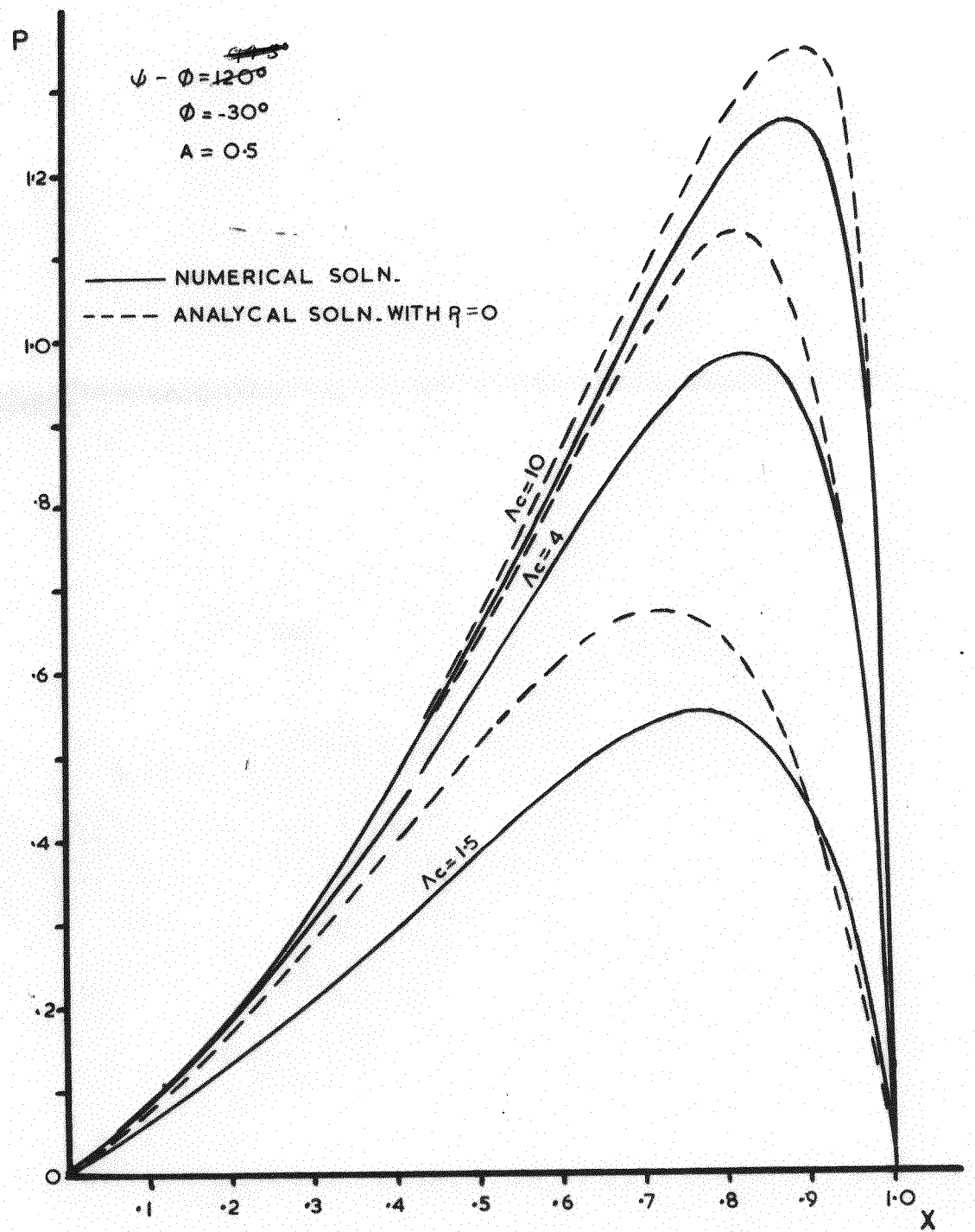

FIG. 17, THEORETICAL PRESSURE PROFILES $P_1 = 0$. INFINITE BEARING.

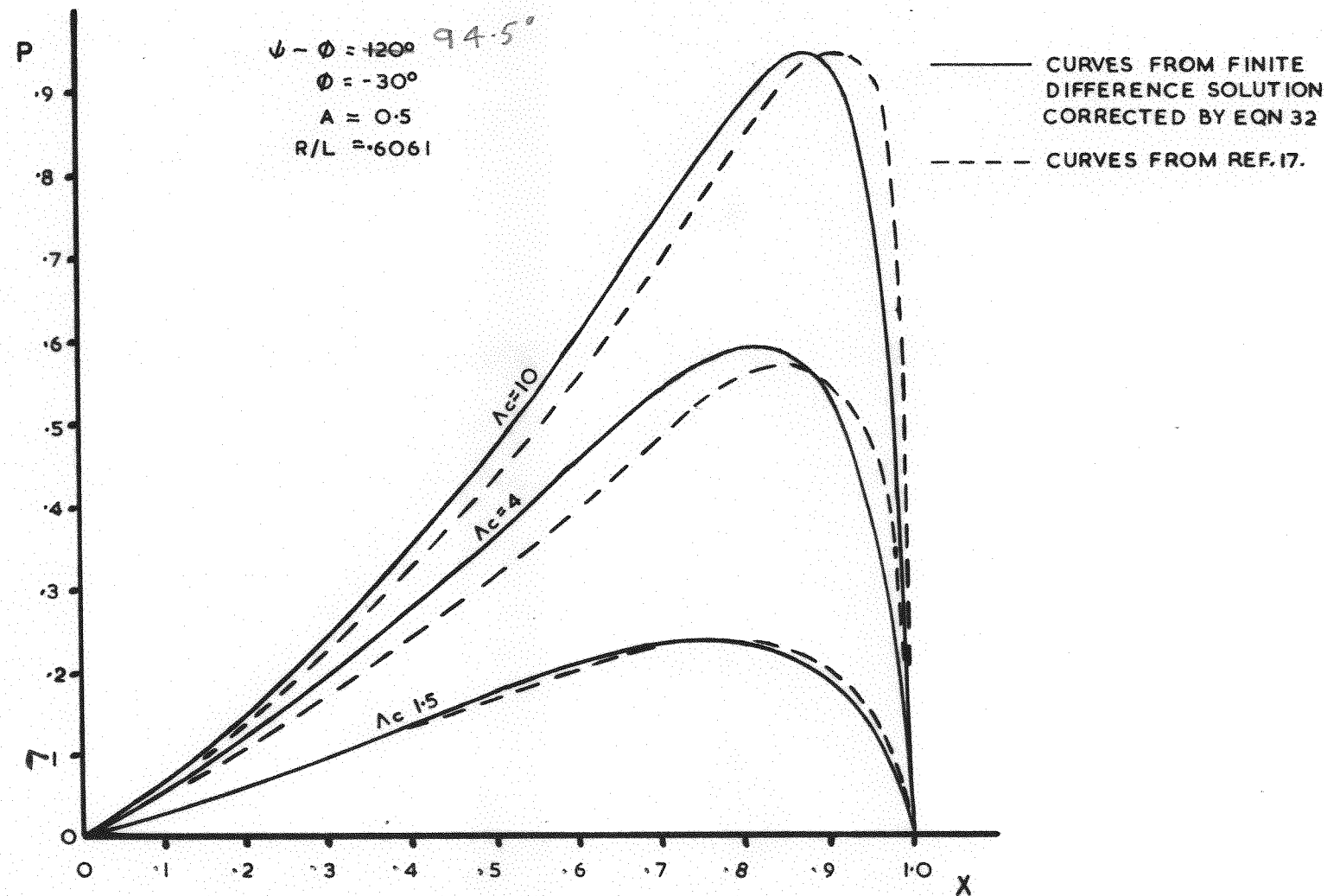

FIG. 18. NUMERICAL PRESSURE PROFILE. REF 17. CIRCUMFERENTIAL.

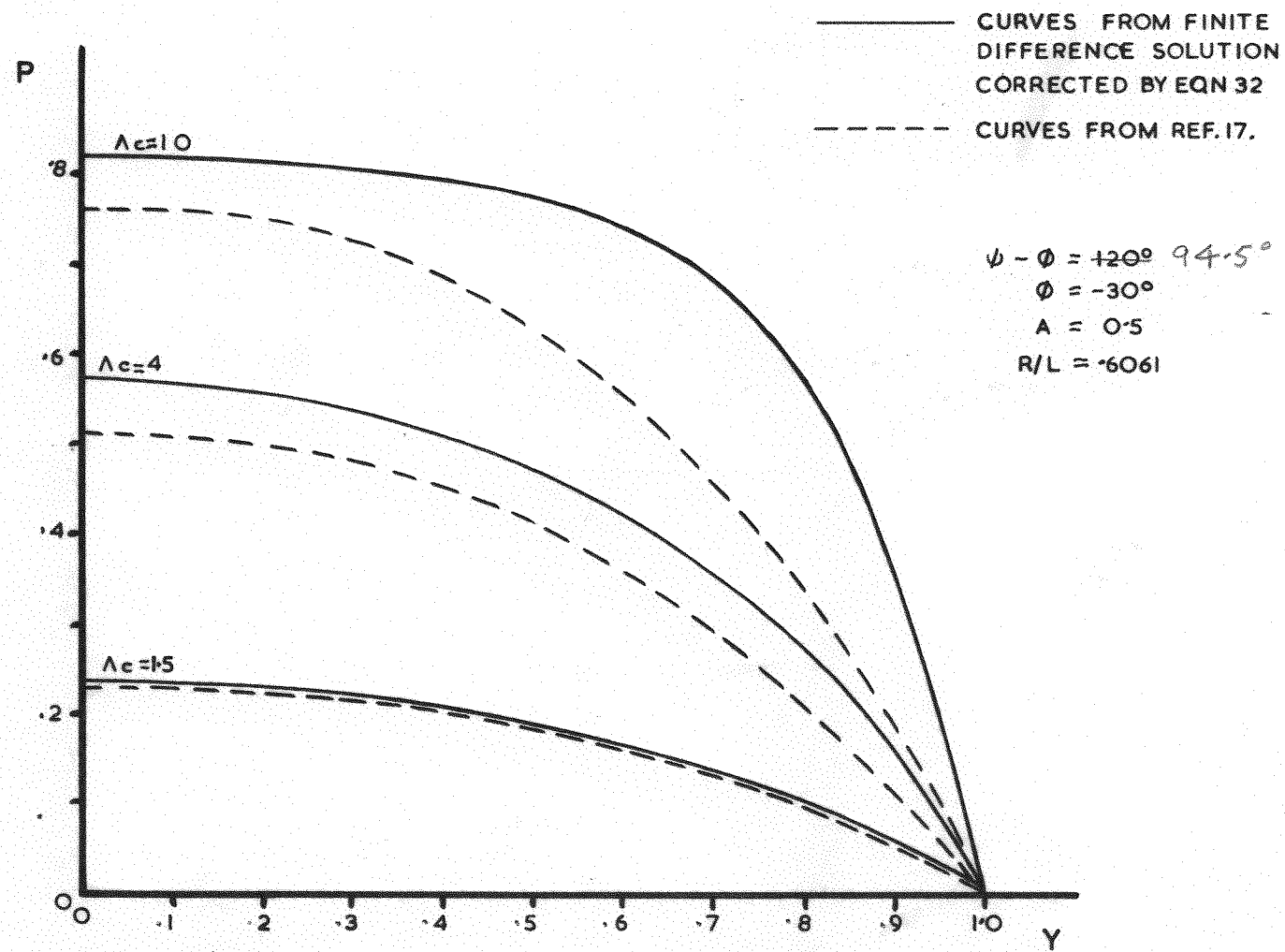

FIG. 19. NUMERICAL PRESSURE PROFILES. REF 17. AXIAL.

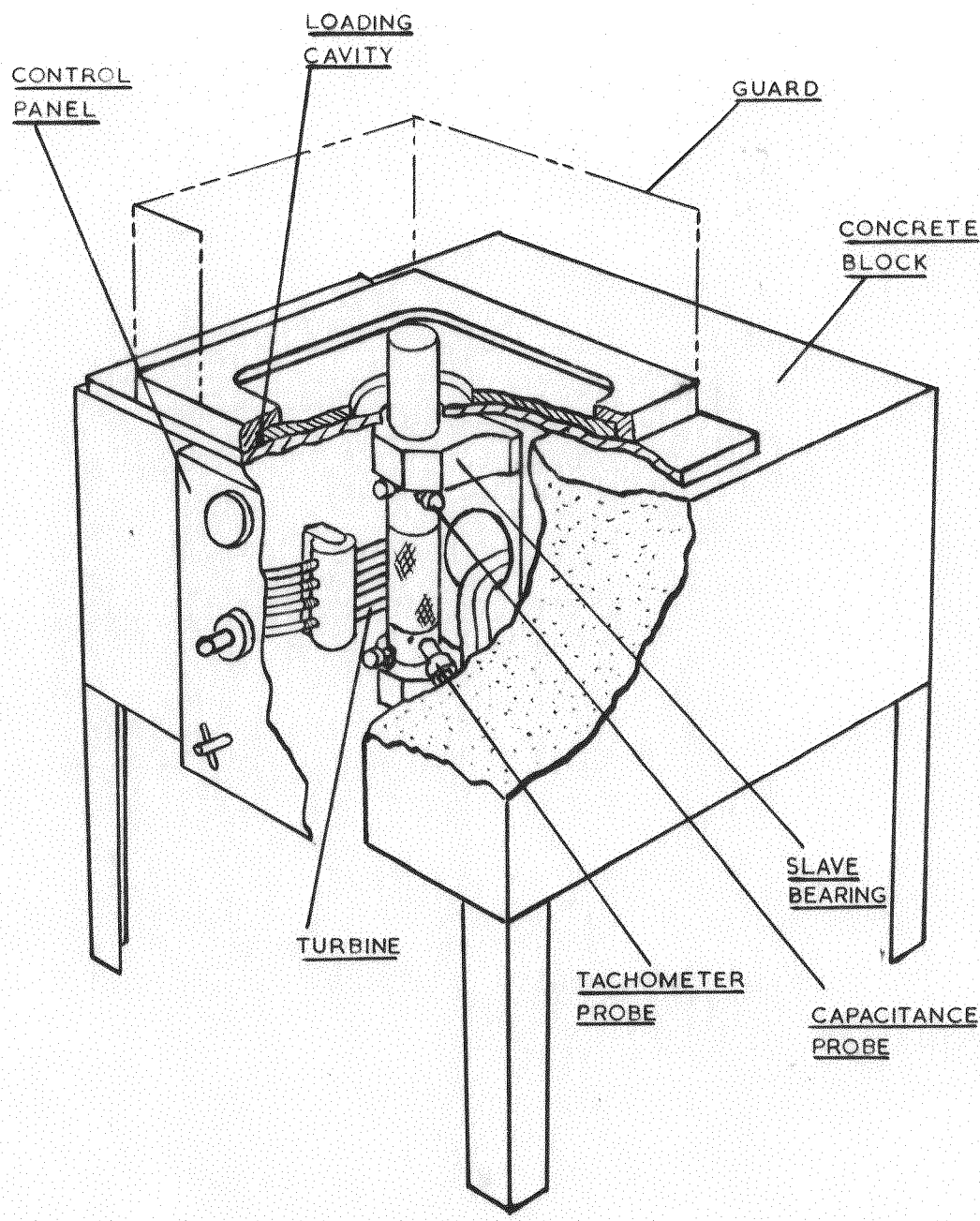

FIG.20. SECTIONED DIAGRAM OF RIG

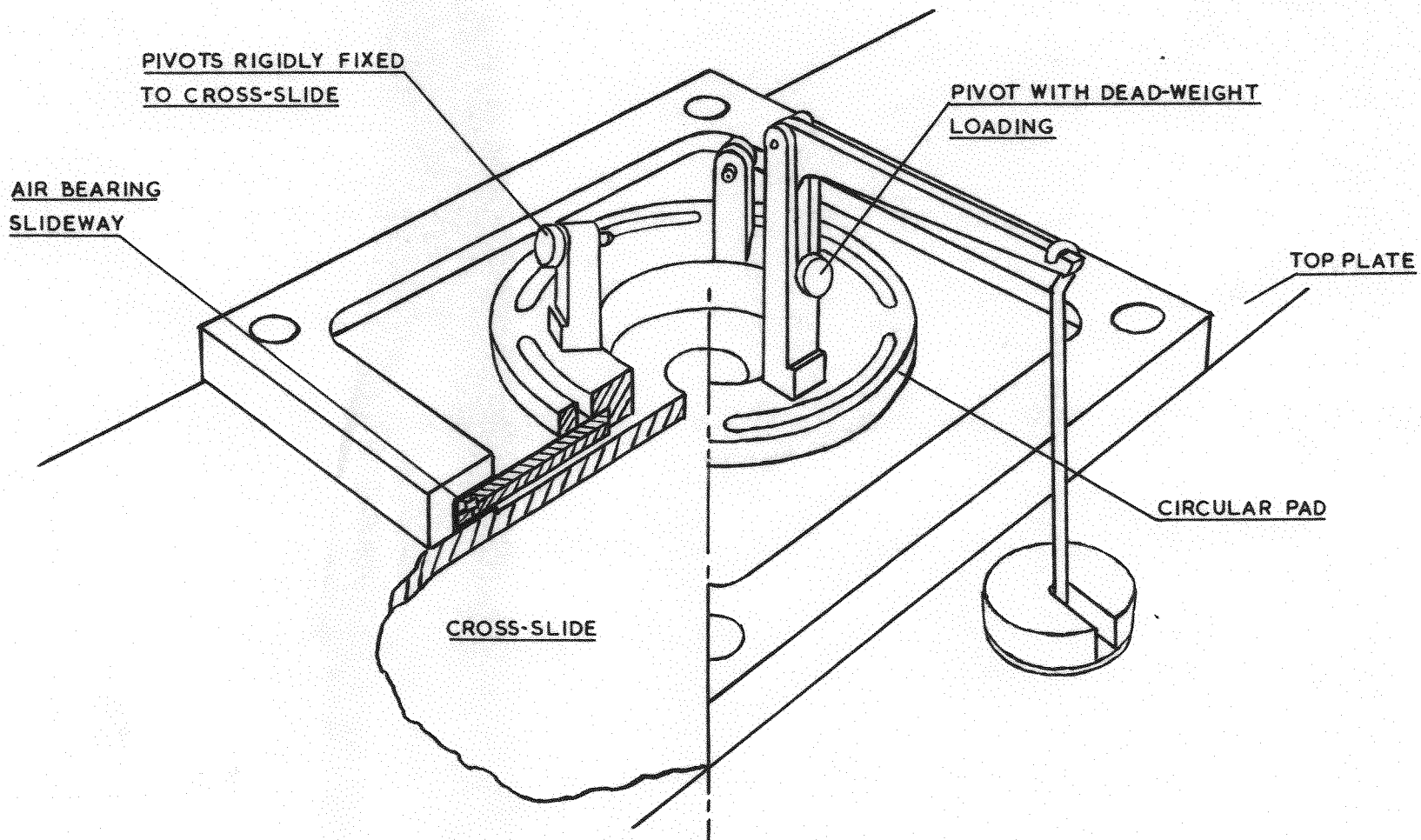

FIG.21.SECTIONED DIAGRAM OF CROSS-SLIDE

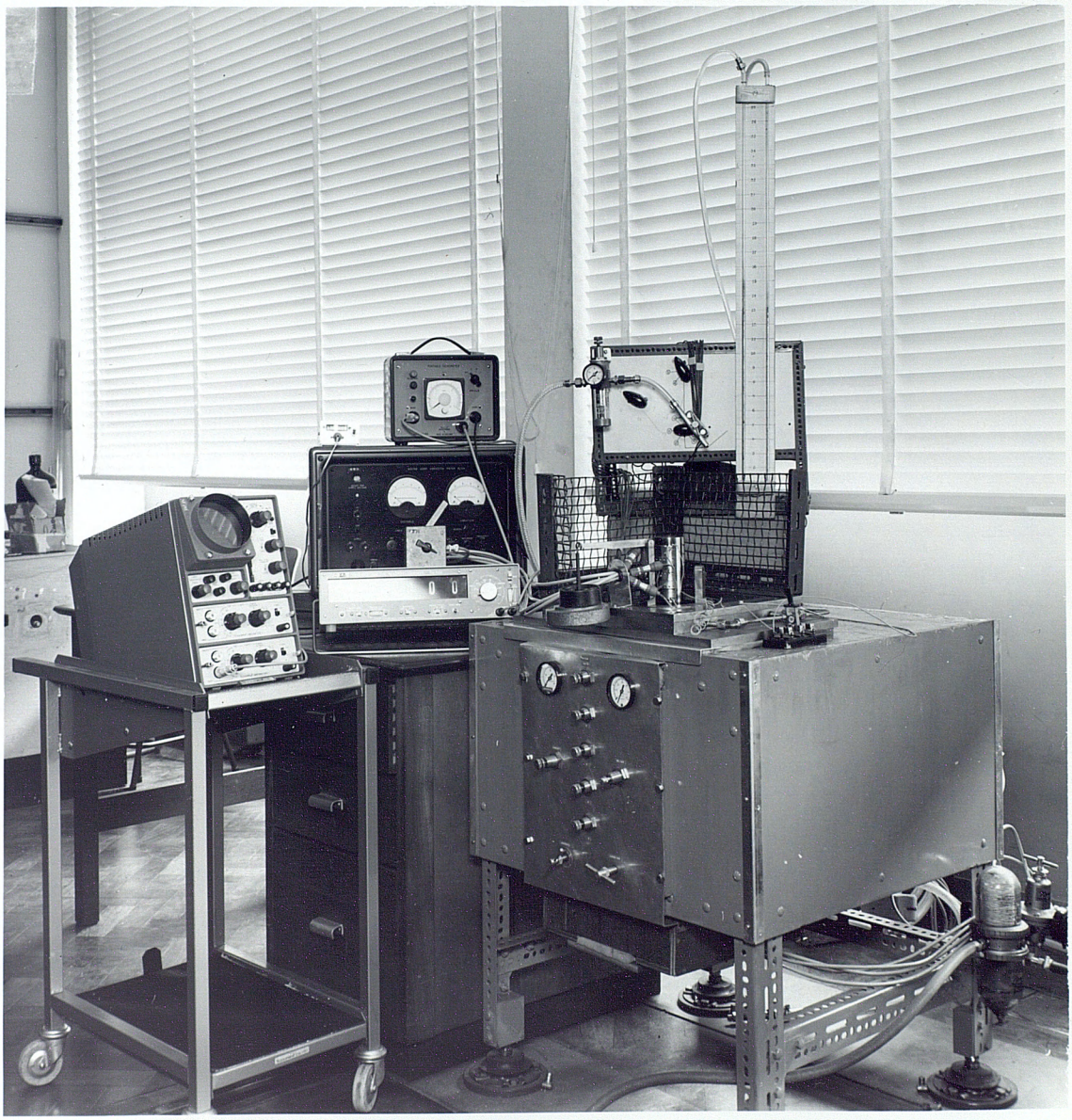

Figure 22. Rig (general)

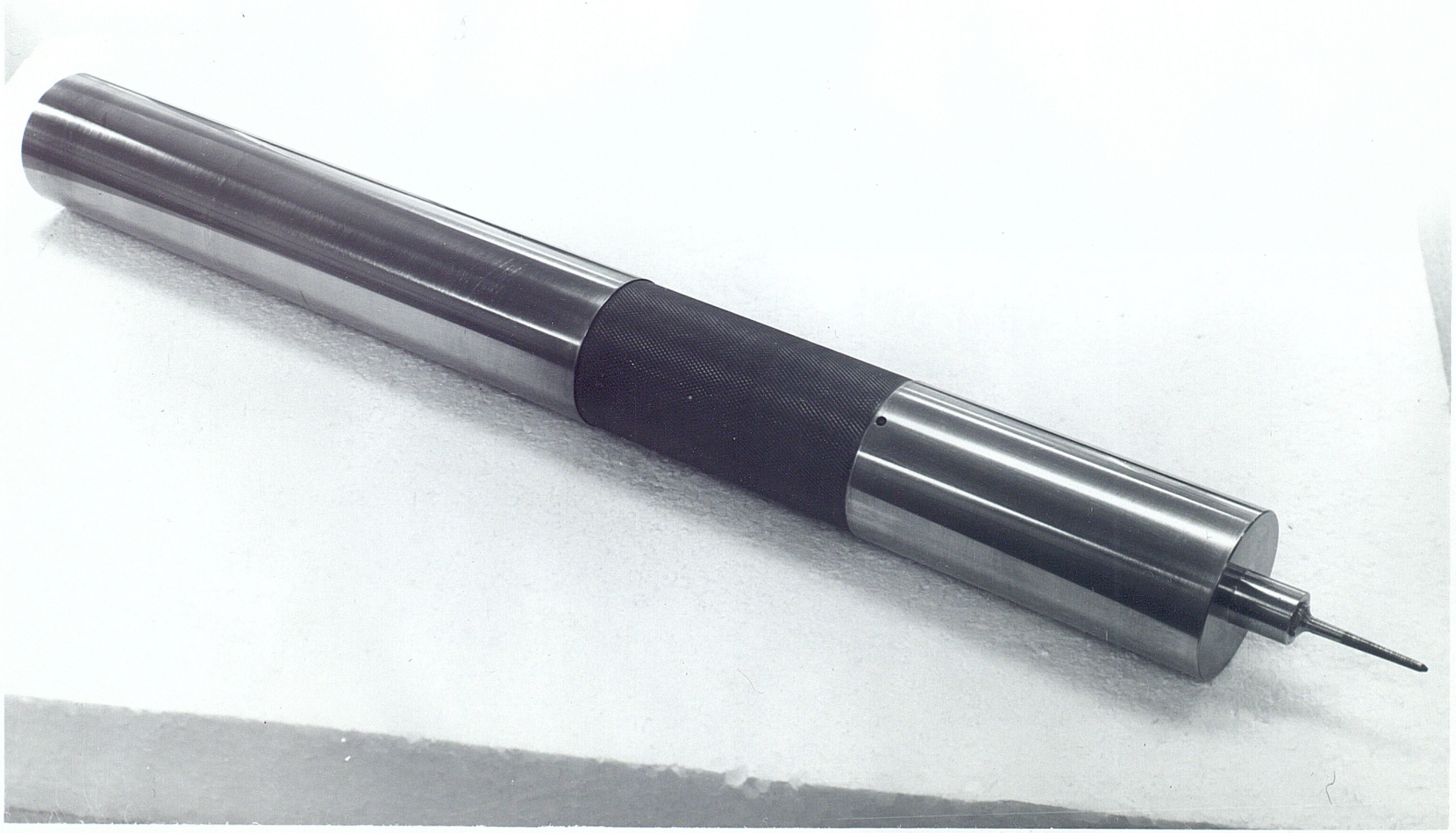

Figure 23. Shaft

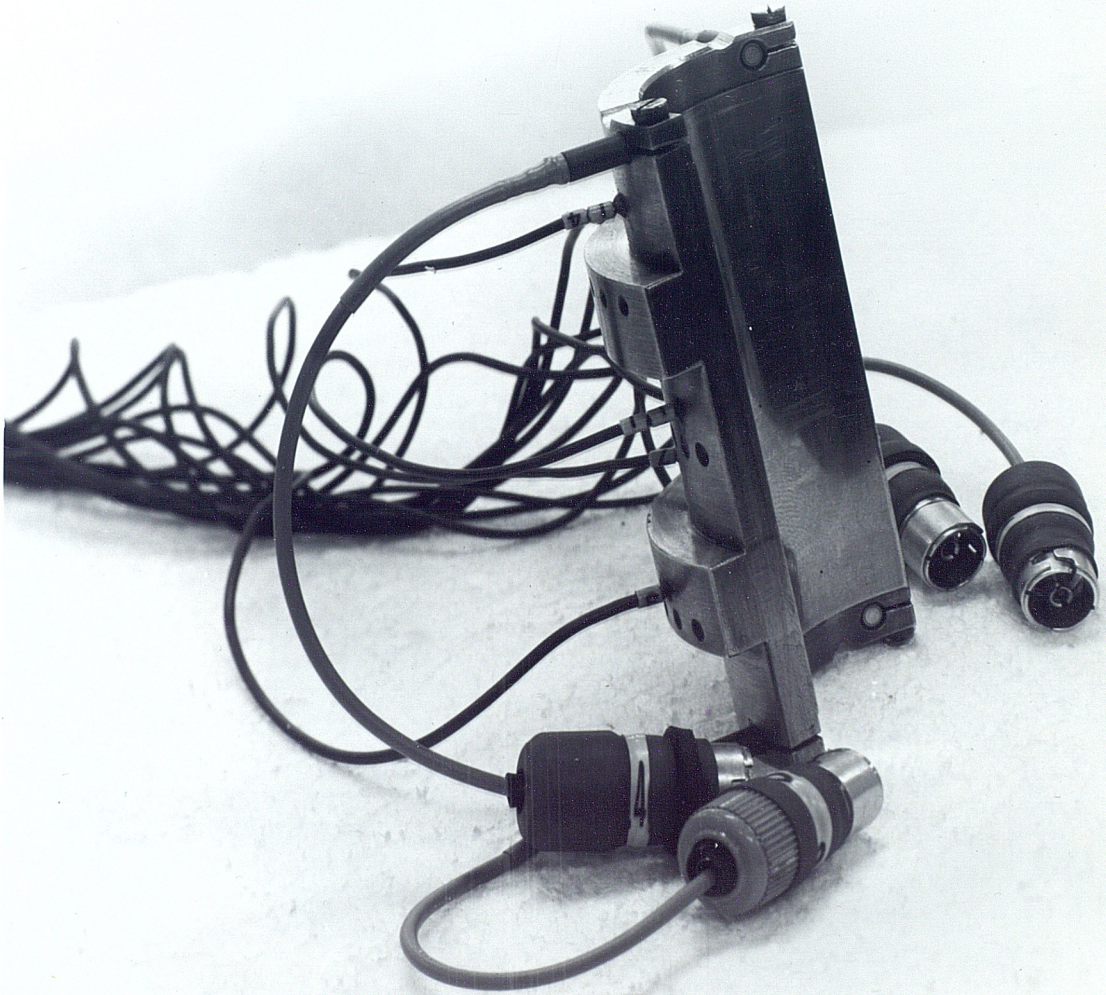

Figure 24. Test Pad

Figure 25. Capacitance Probe

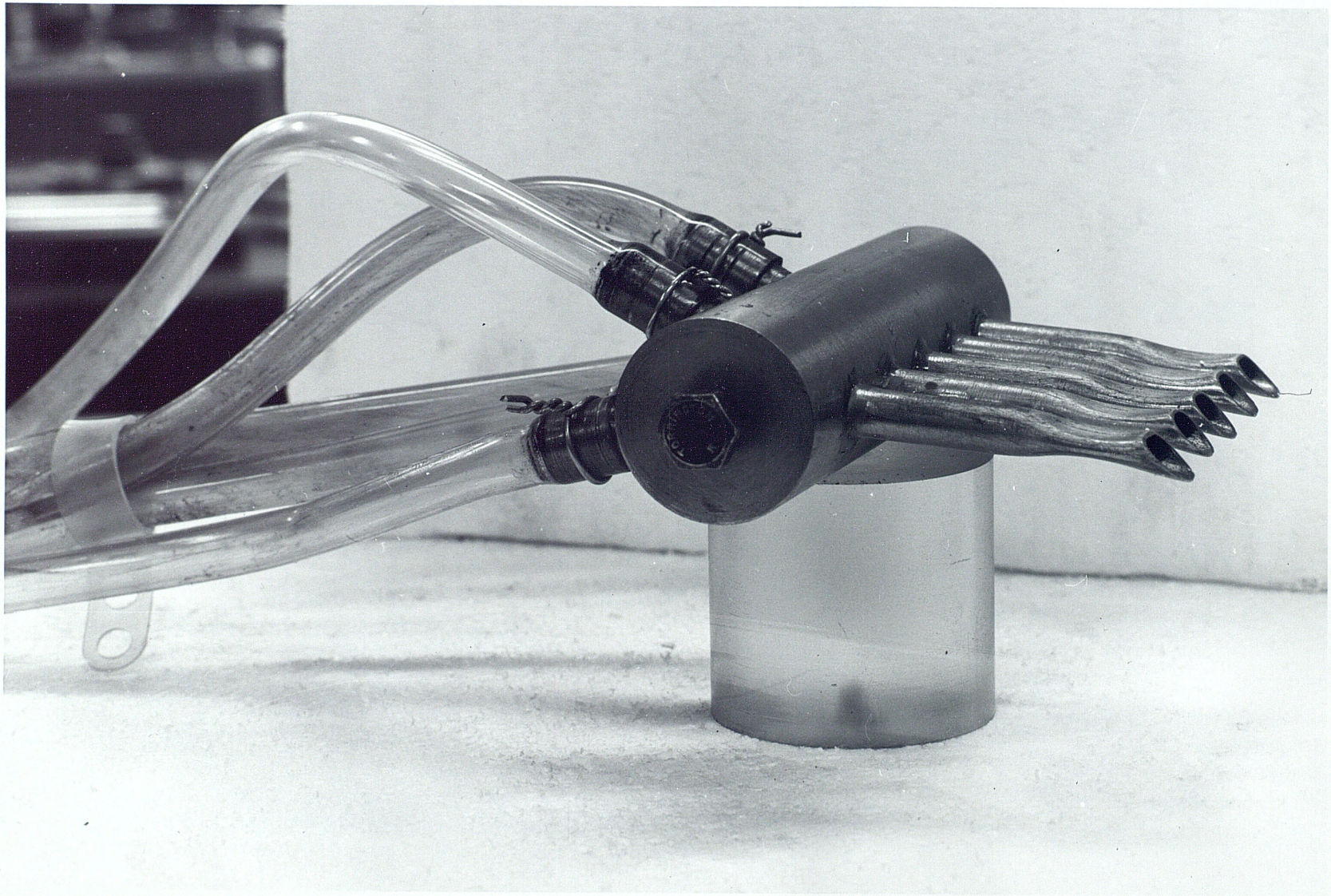

Figure 26. Nozzles

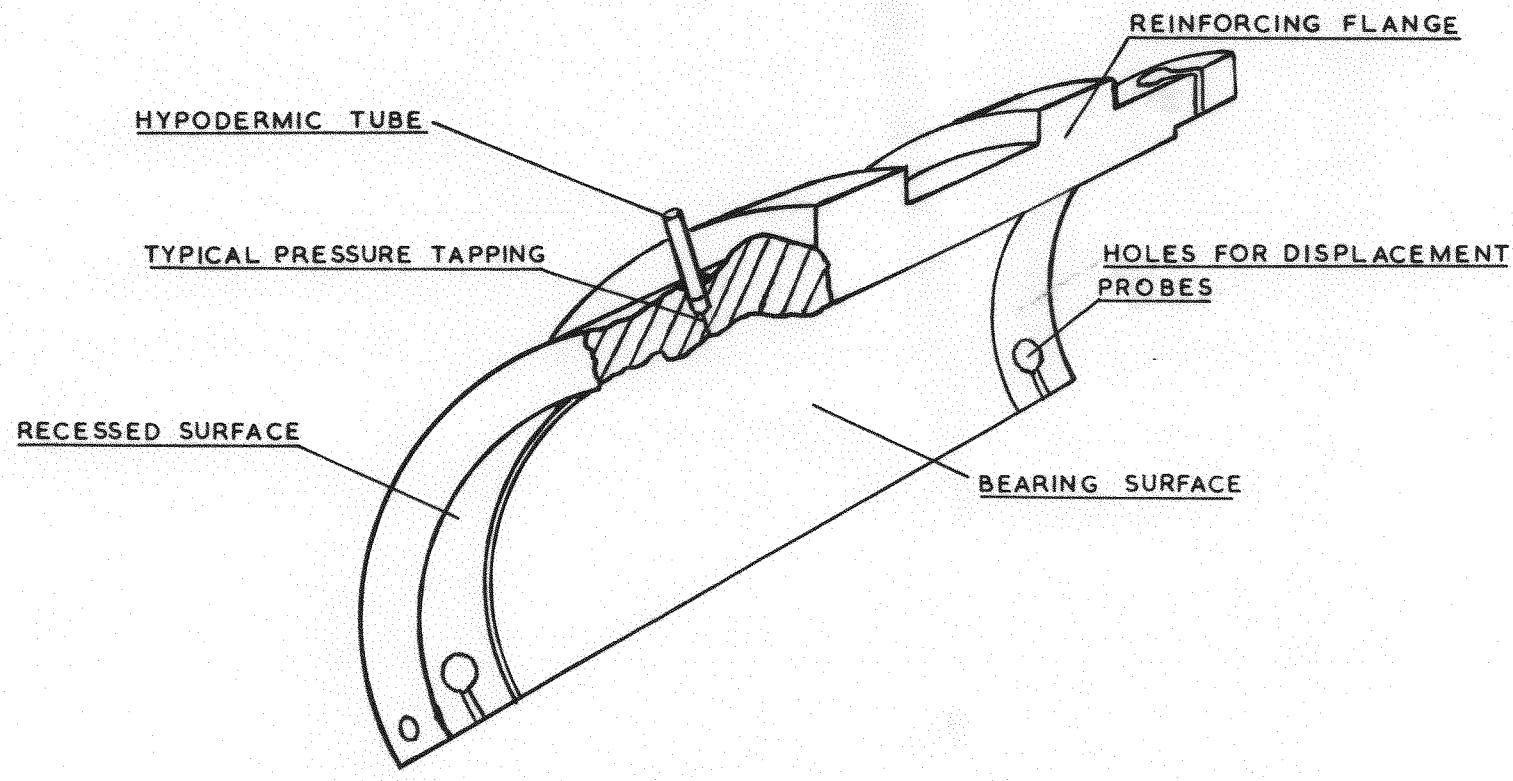

FIG. 27. SECTIONED DIAGRAM OF TEST PAD

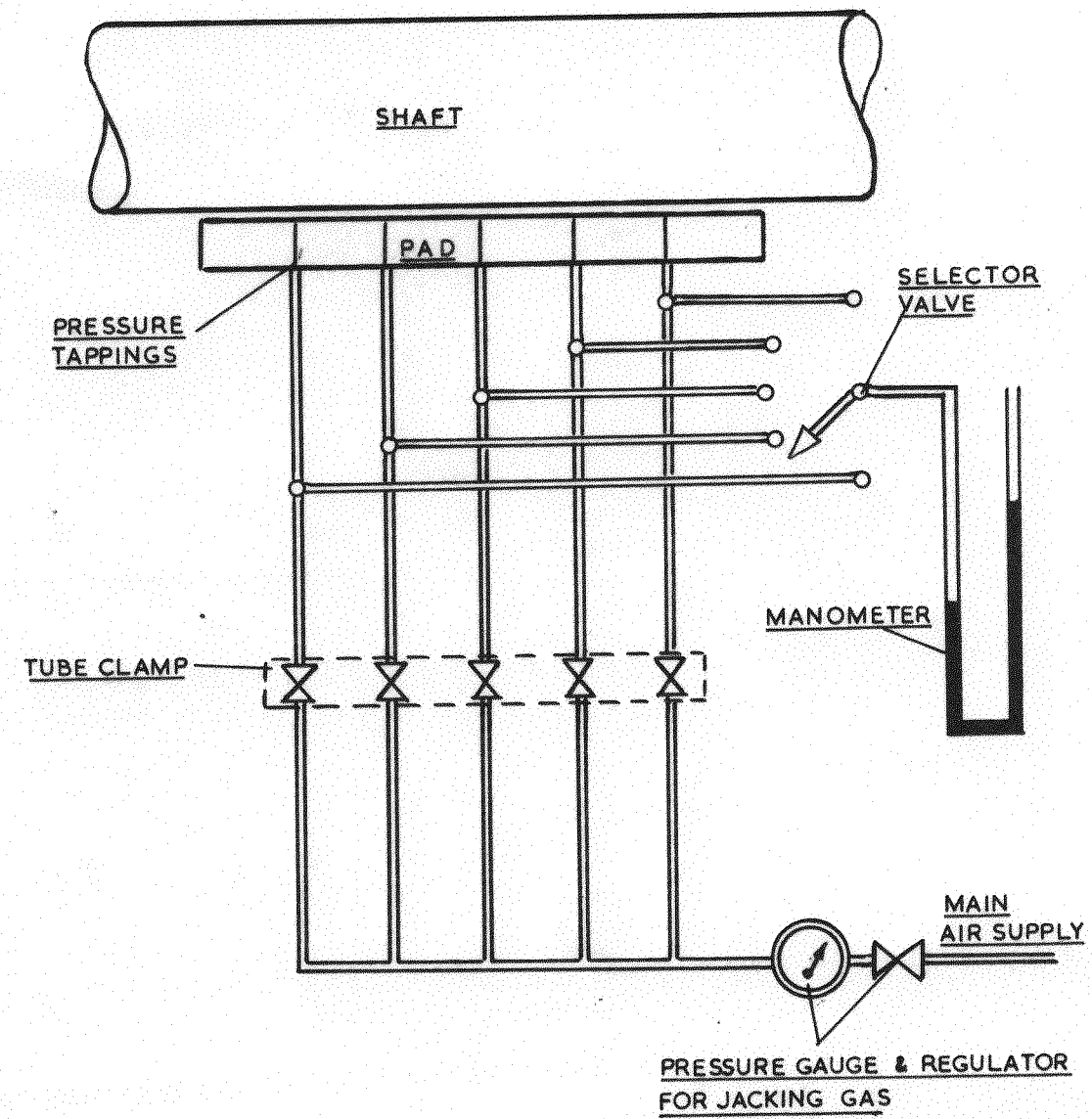

FIG.28. LINE DIAGRAM OF THE JACKING & PRESSURE RECORDING SYSTEM

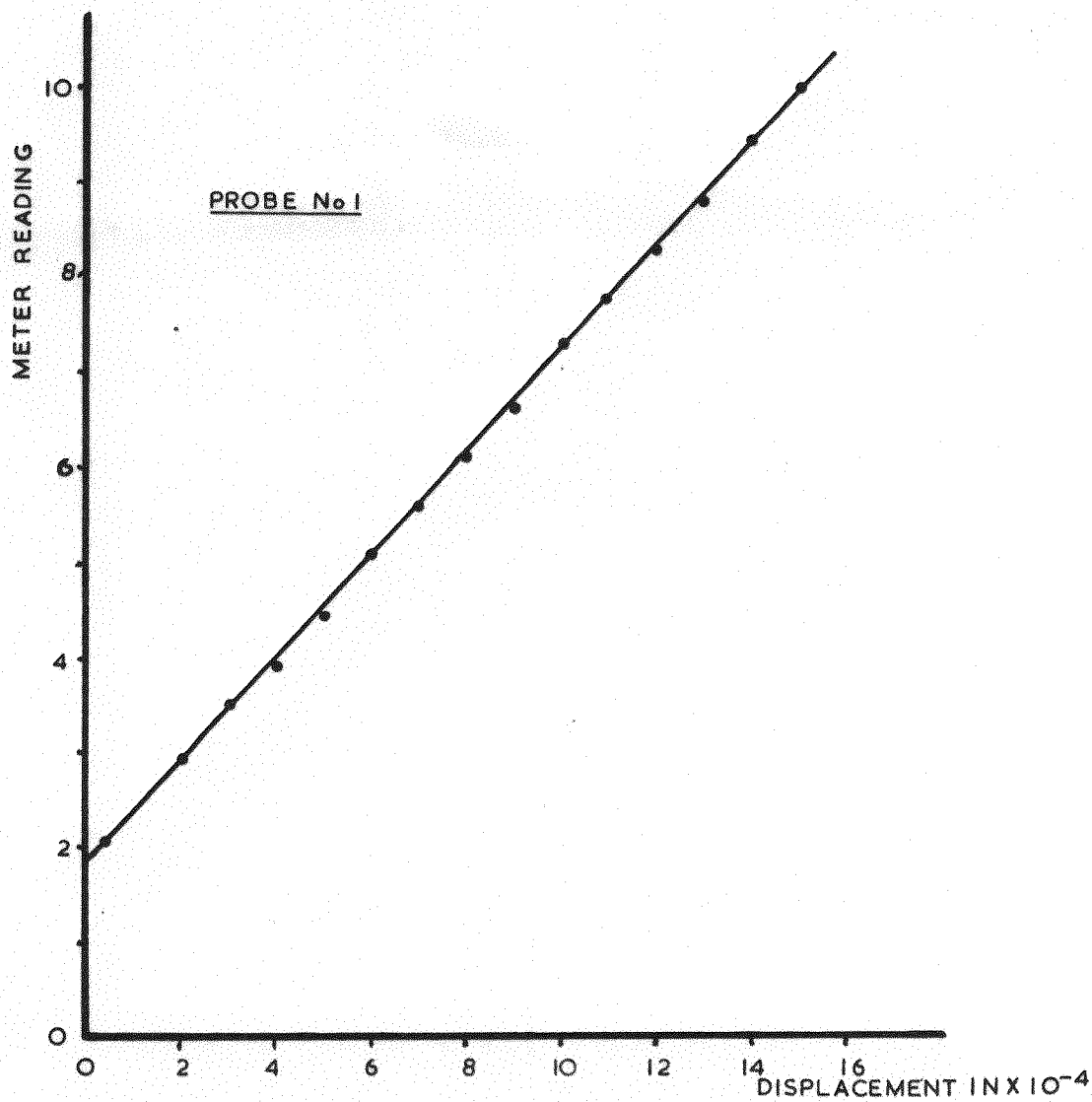

FIG.29. CAPACITANCE PROBE CALIBRATION CURVE

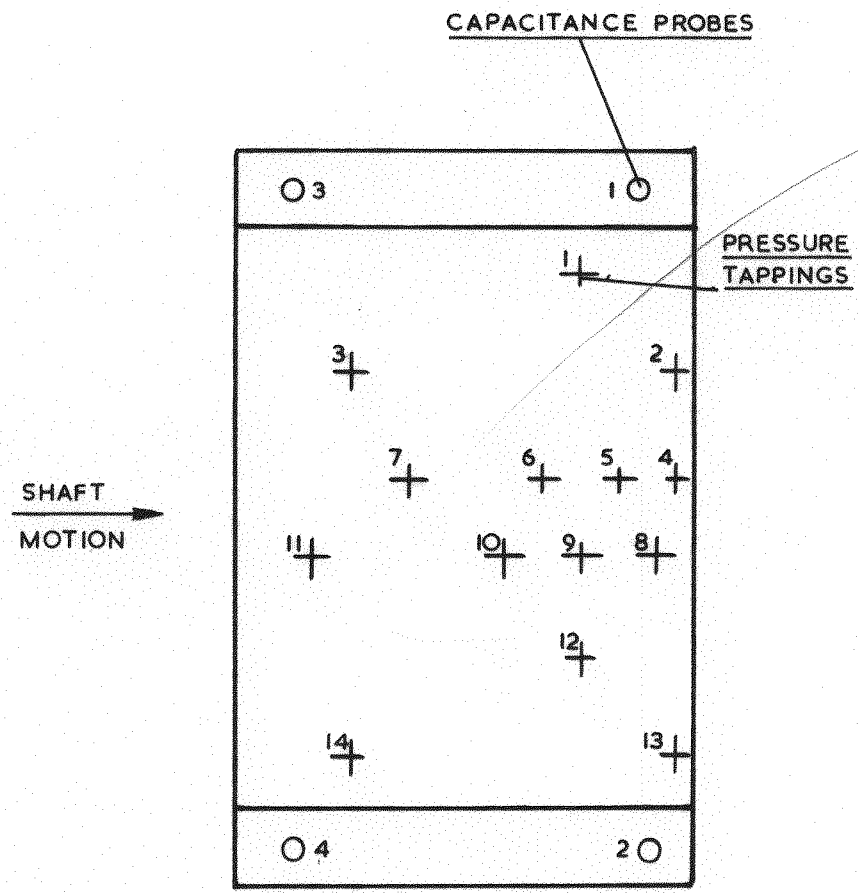

POSITION OF TAPPINGS GIVEN IN THE TABLES OF PRESSURE DISTRIBUTION

FIG.30. LAYOUT OF PRESSURE TAPPING HOLES

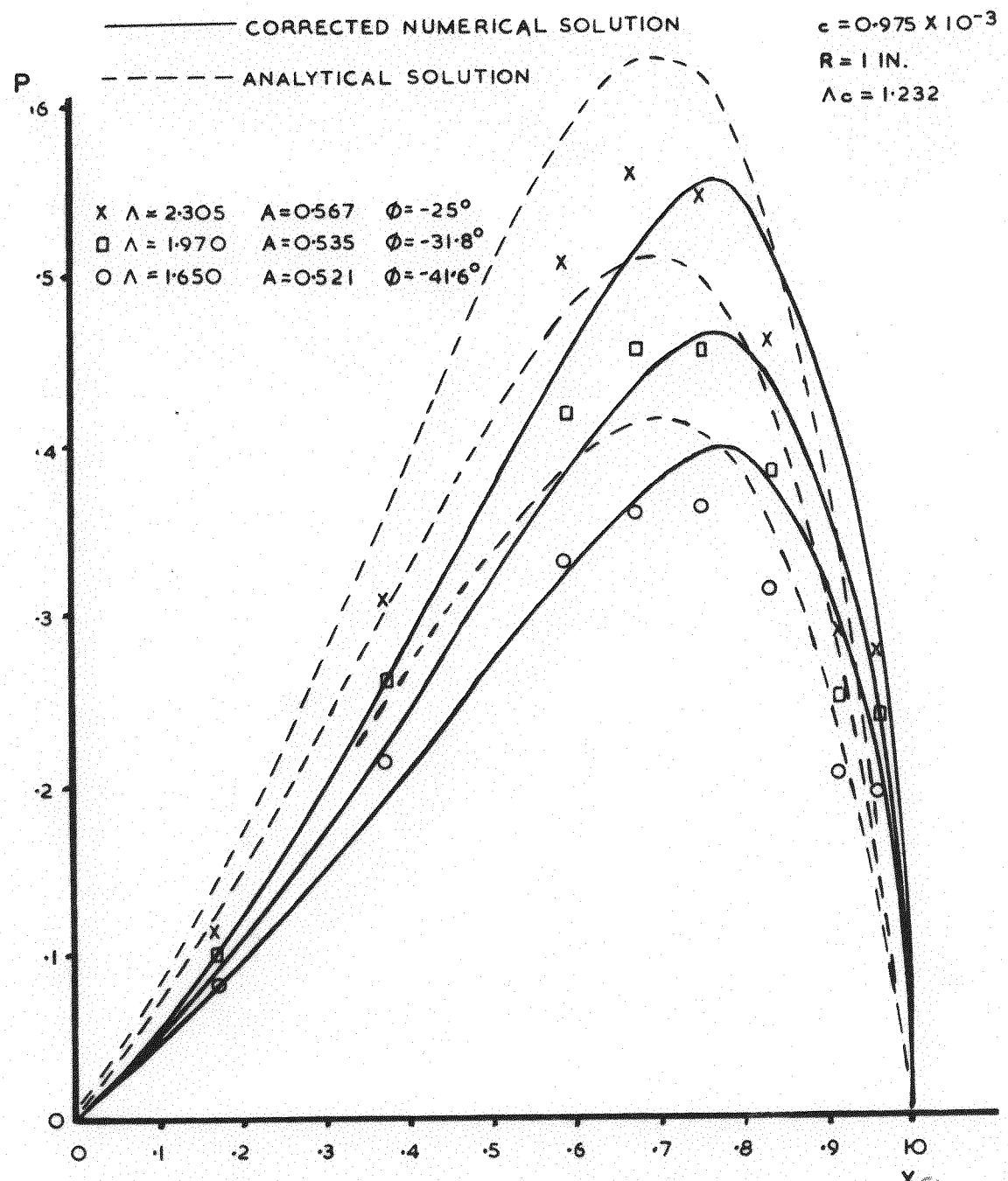

FIG. 31. EXPERIMENTAL & THEORETICAL PRESSURE DISTRIBUTION AT Y = 0·20 Λ_c = 1·232

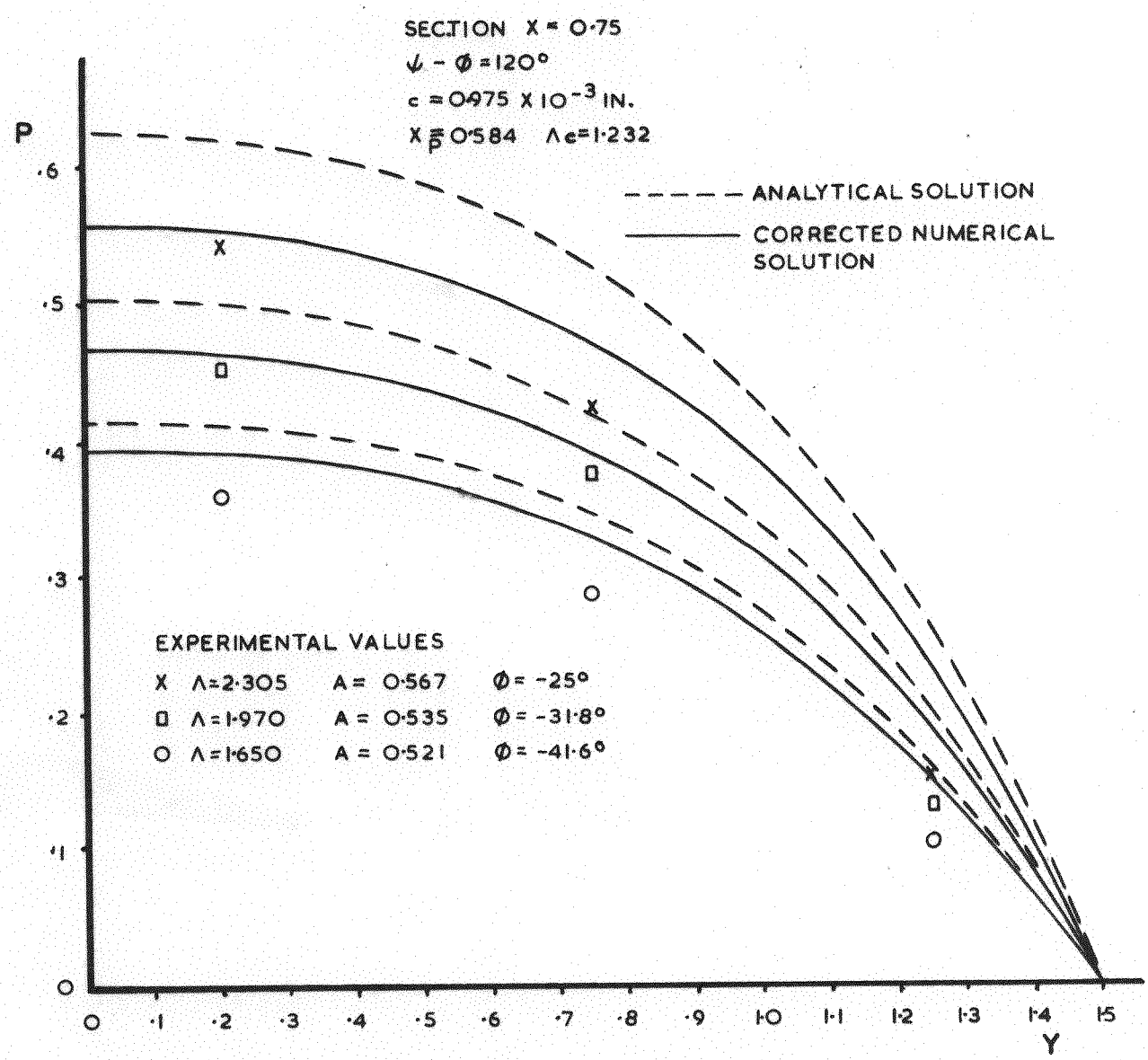

FIG. 32. EXPERIMENTAL & THEORETICAL PRESSURE DISTRIBUTION AT X = 0·75 Λ_c = 1·232

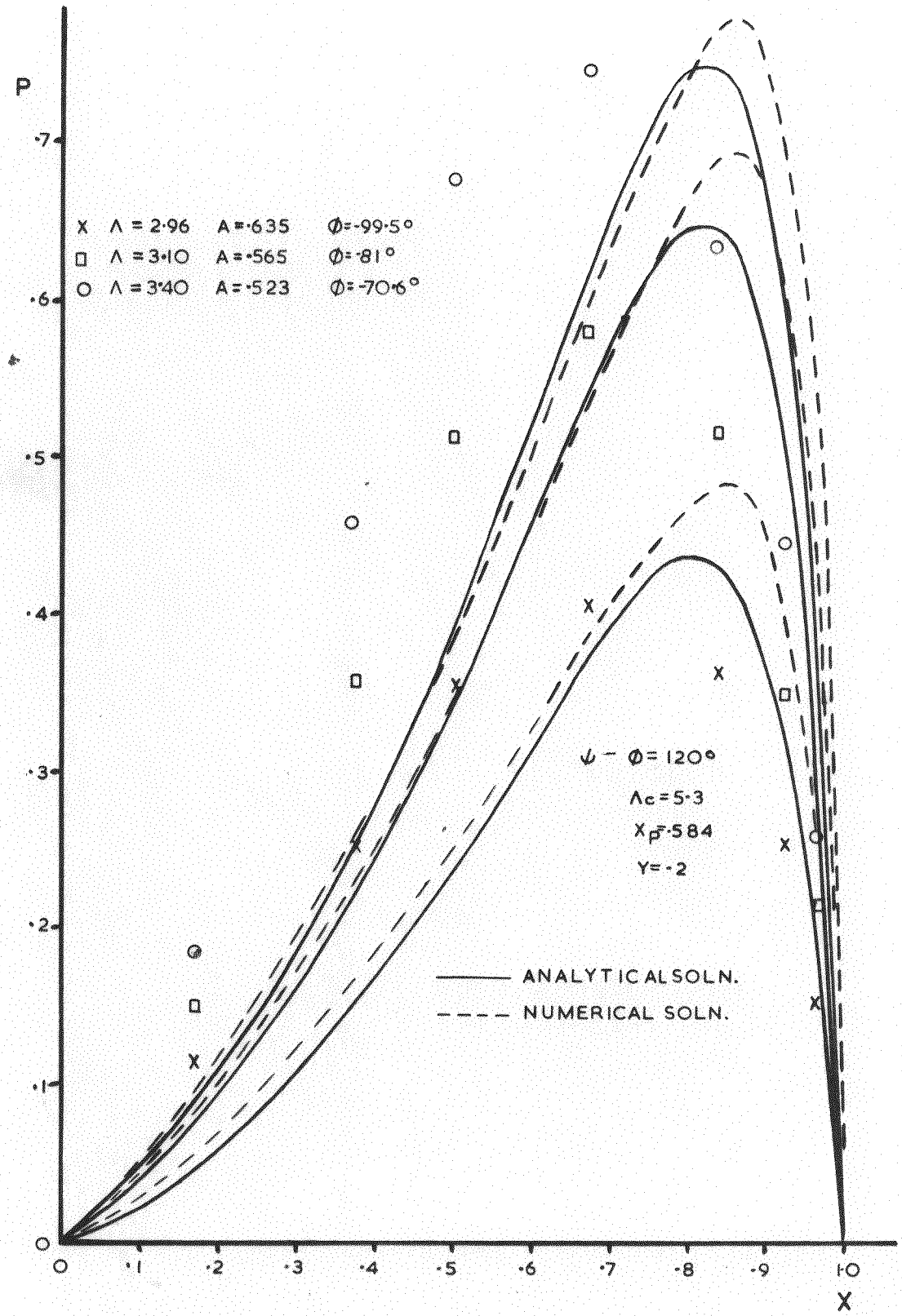

FIG. 33. EXPERIMENTAL & THEORETICAL PRESSURE DISTRIBUTION $\Lambda_c = 5{\cdot}3$

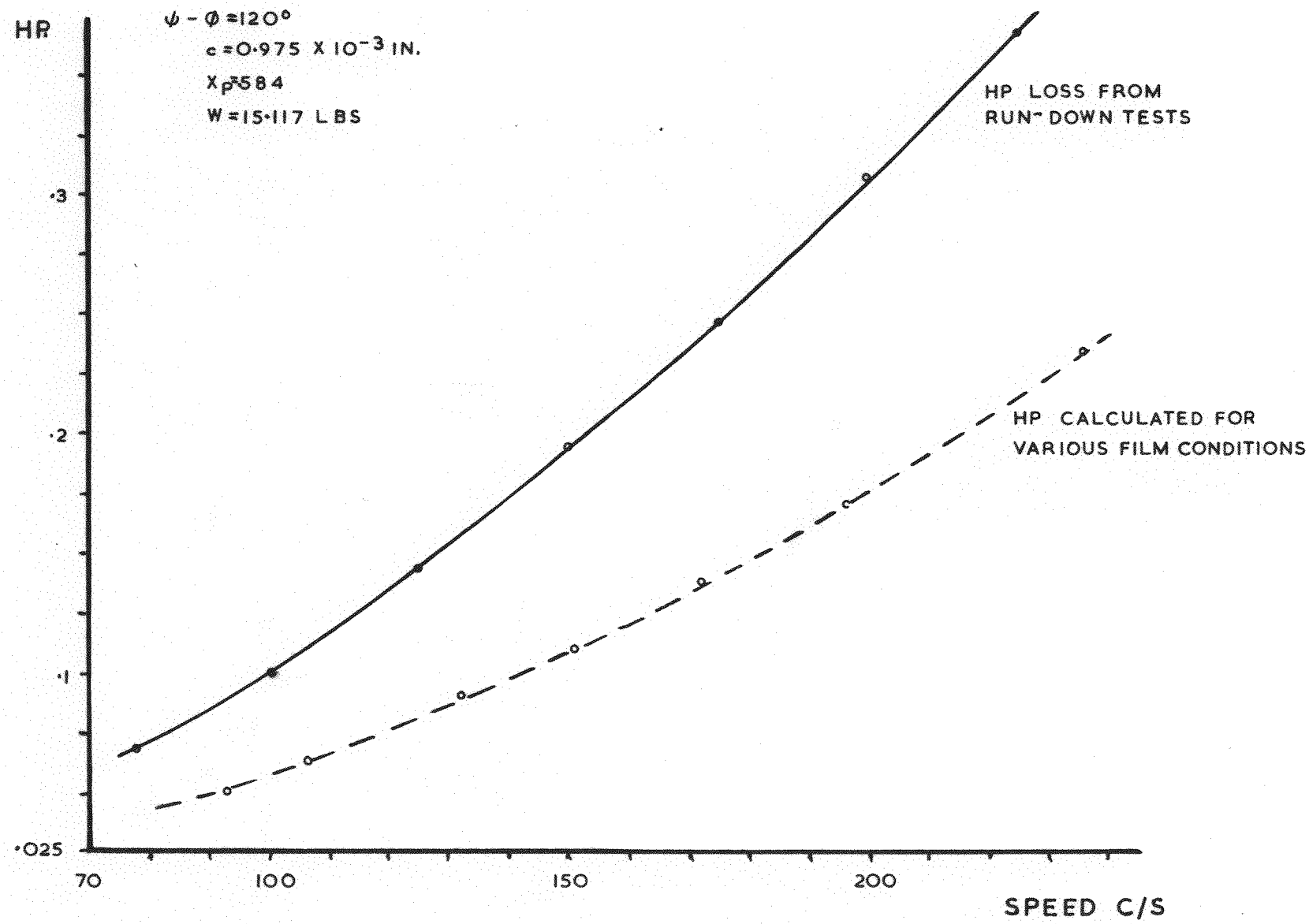

FIG. 34. POWER LOSS DUE TO VISCOUS DRAG

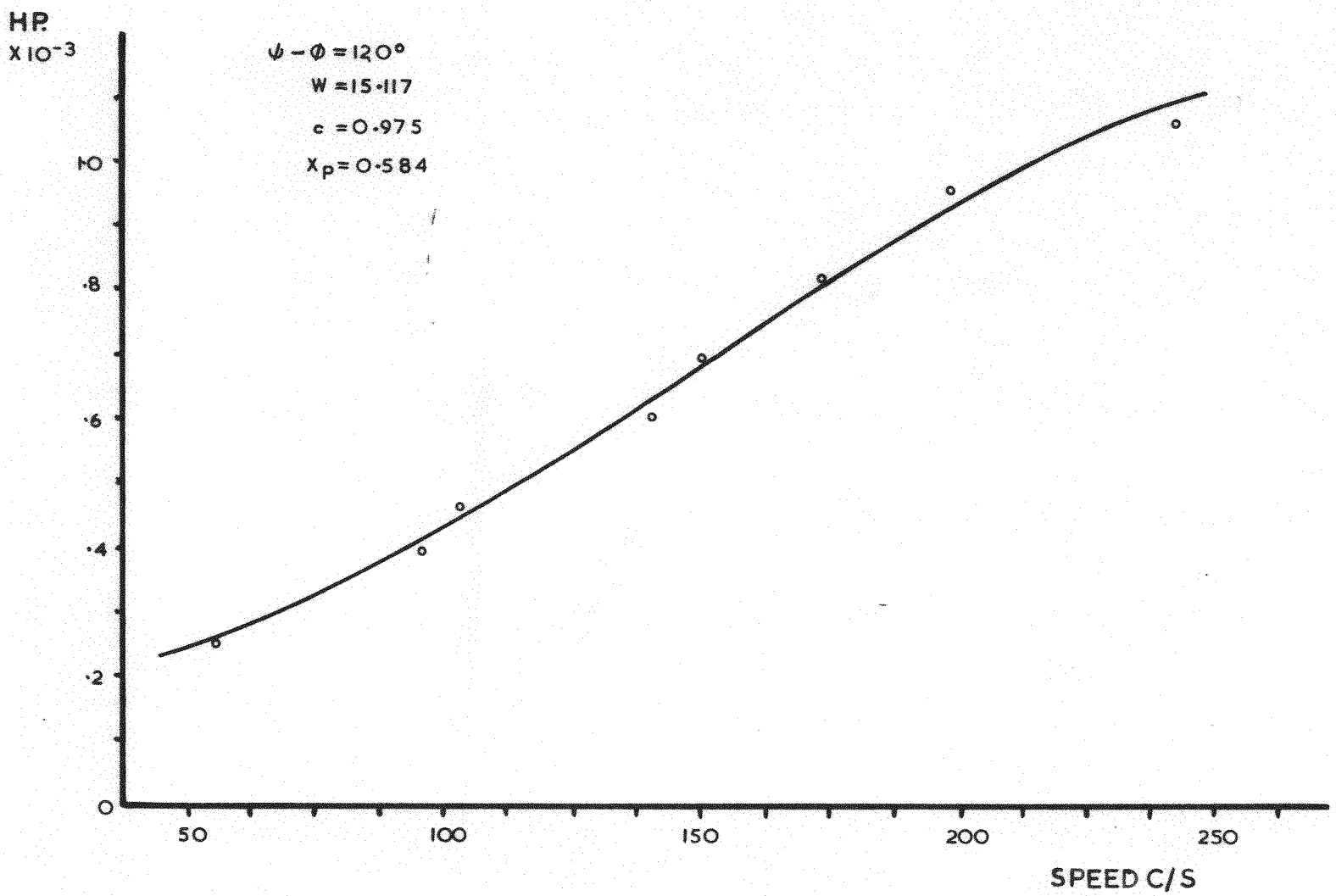

FIG, 35, POWER LOSS DUE TO PAD TILT

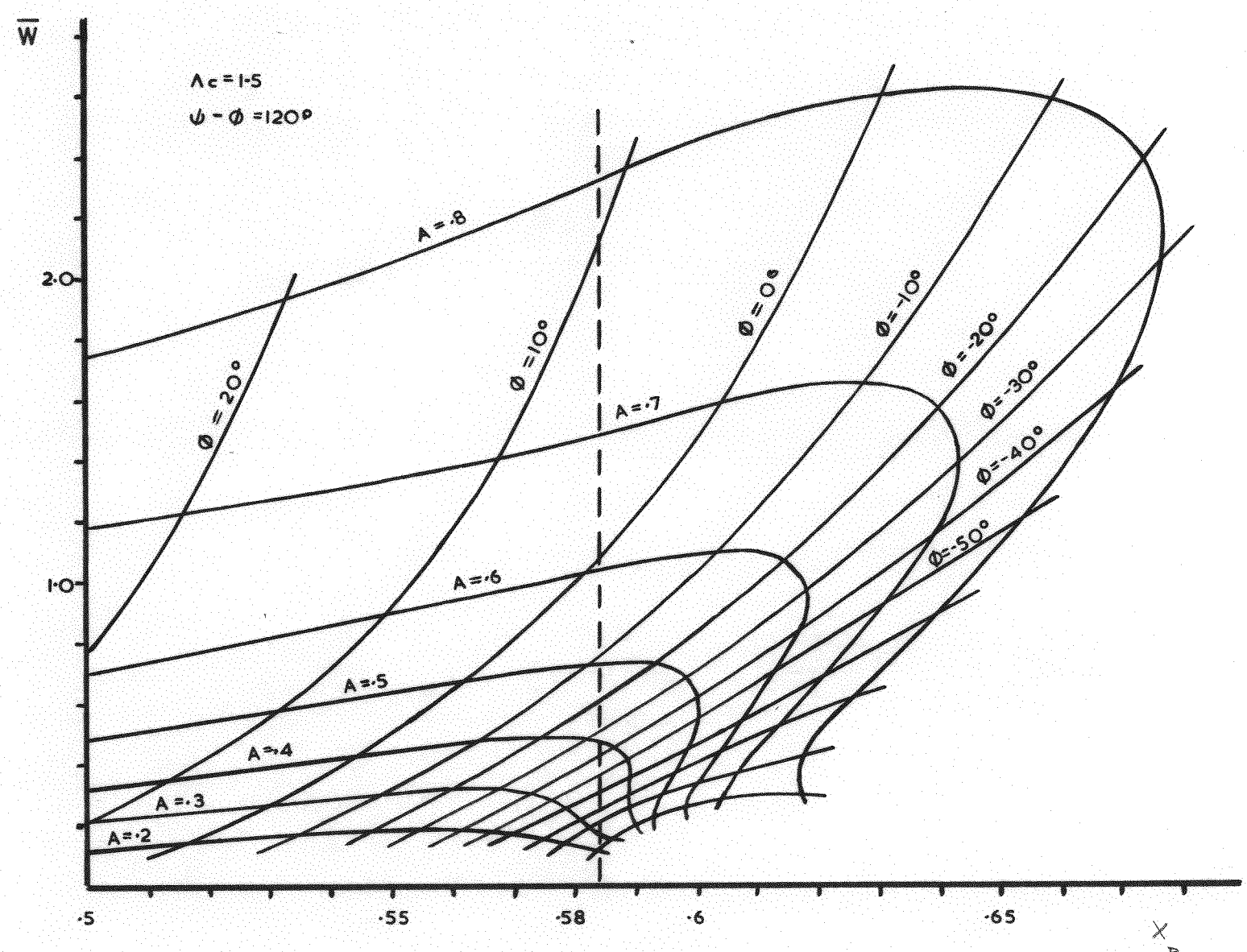

FIG.38. $\overline{W}$ – X_p CURVES FOR OBTAINING STIFFNESS

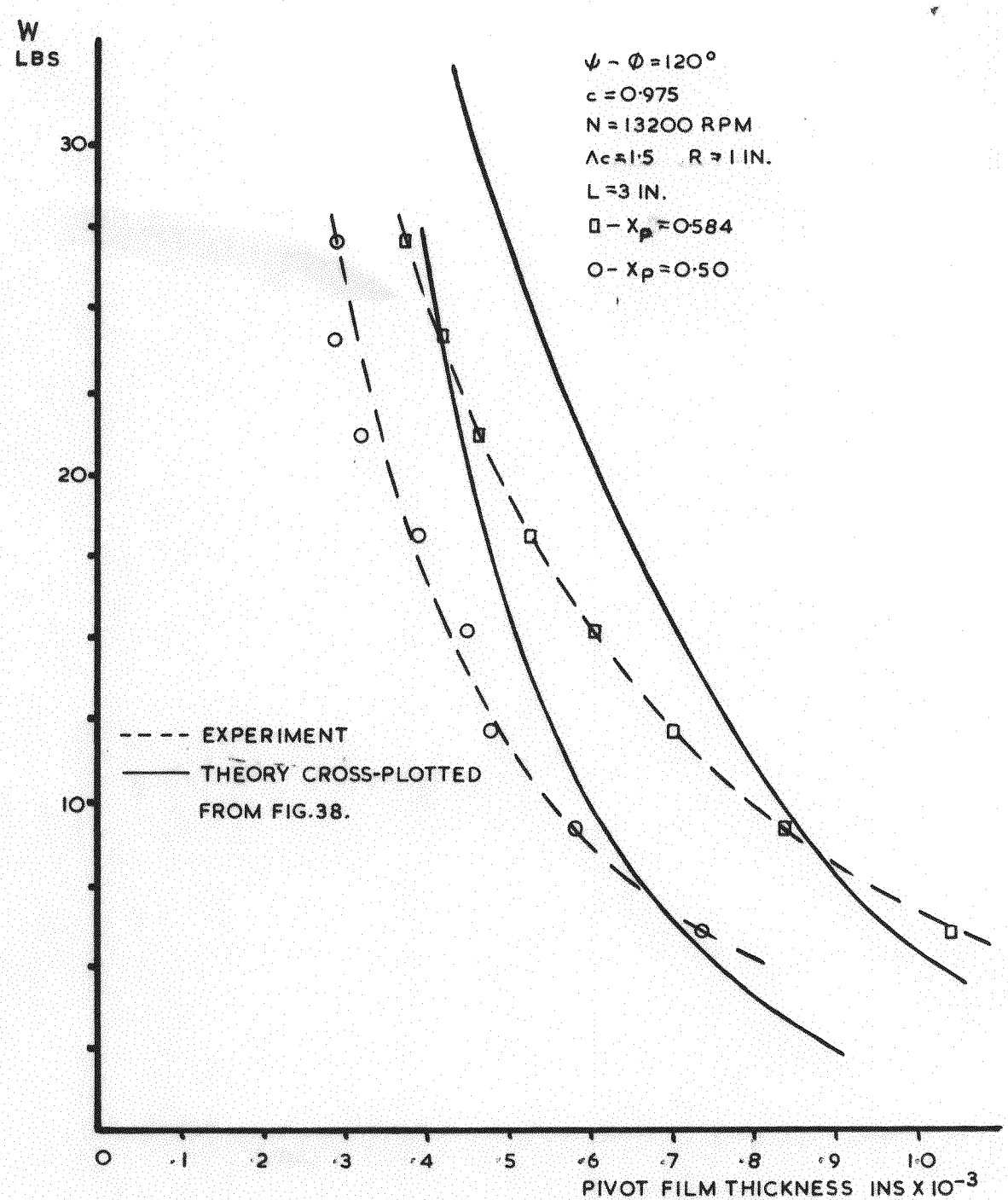

FIG. 39. LOAD - PIVOT CLEARANCE CURVES

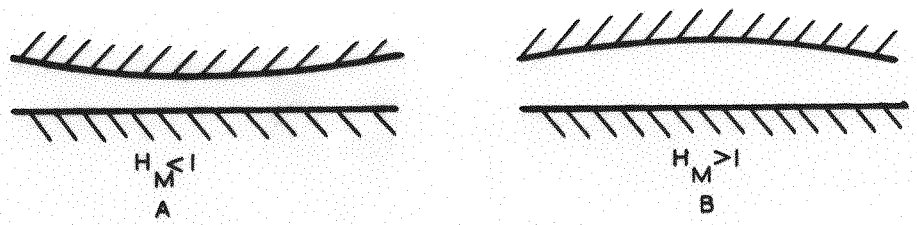

FIG.40. THE EFFECT OF H ON FILM SHAPE

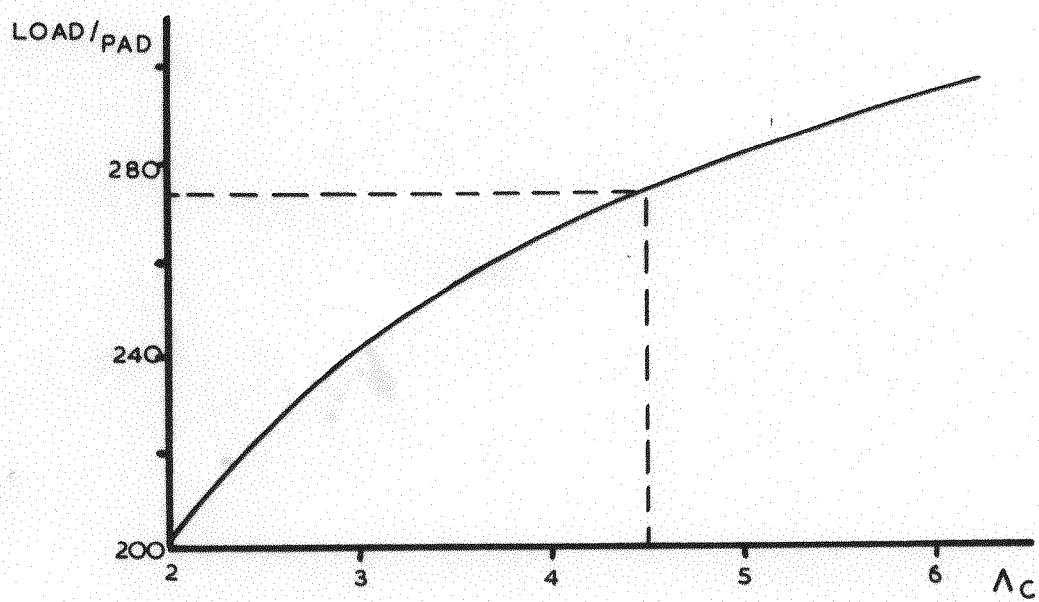

FIG.41. CURVE FOR EXAMPLE.2.

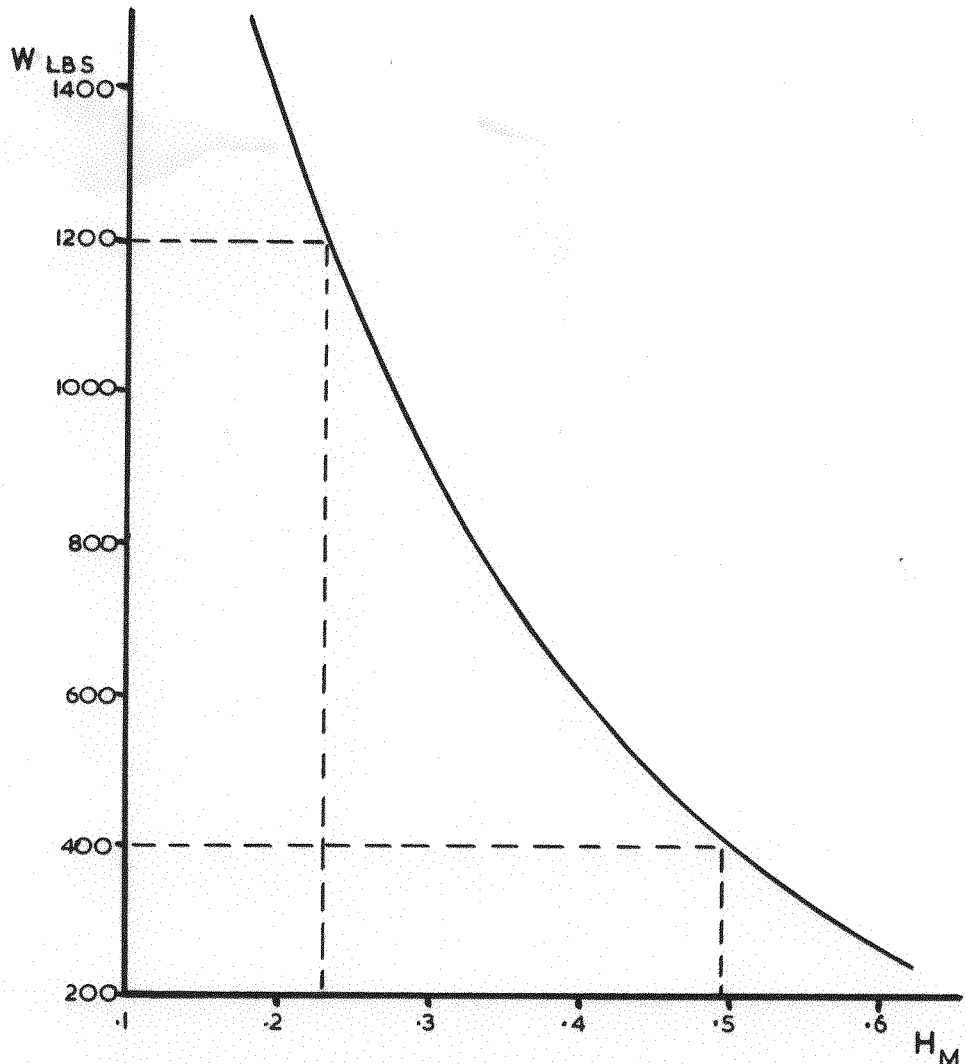

FIG.42.CURVE FOR EXAMPLE.3.

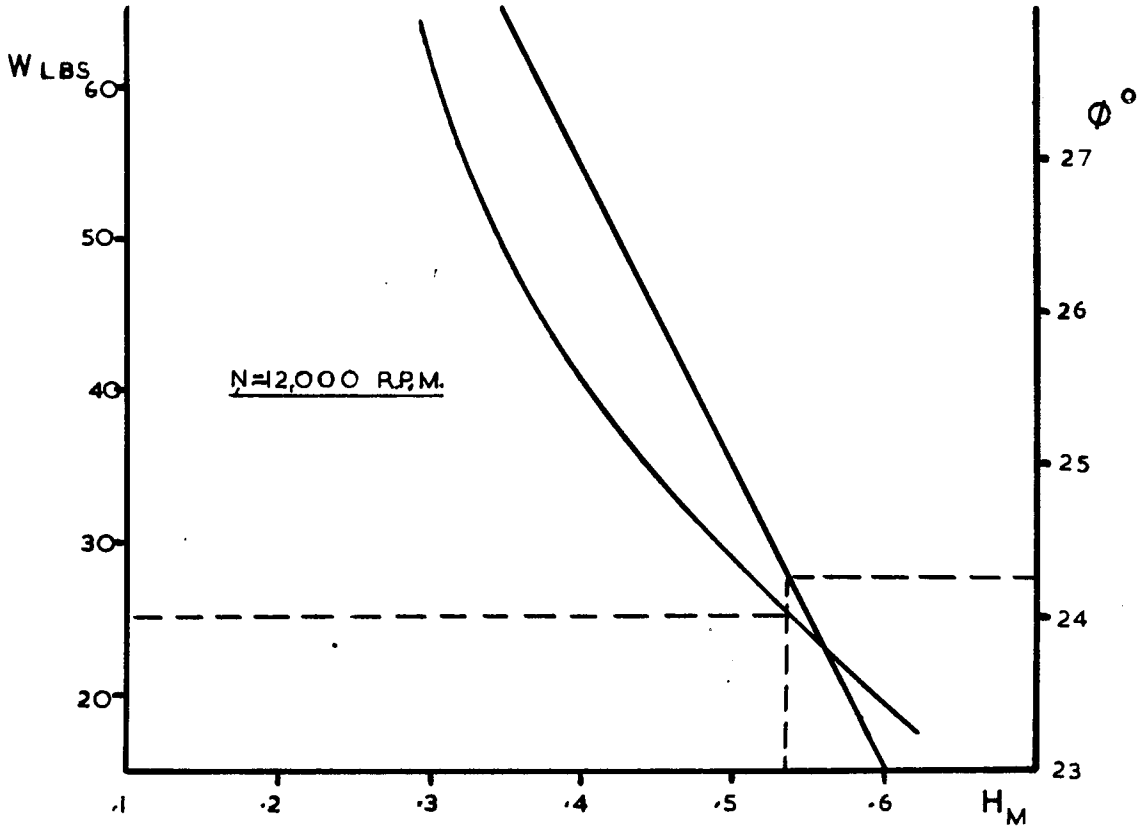

FIG. 43.A. CURVES FOR EXAMPLE. 4.

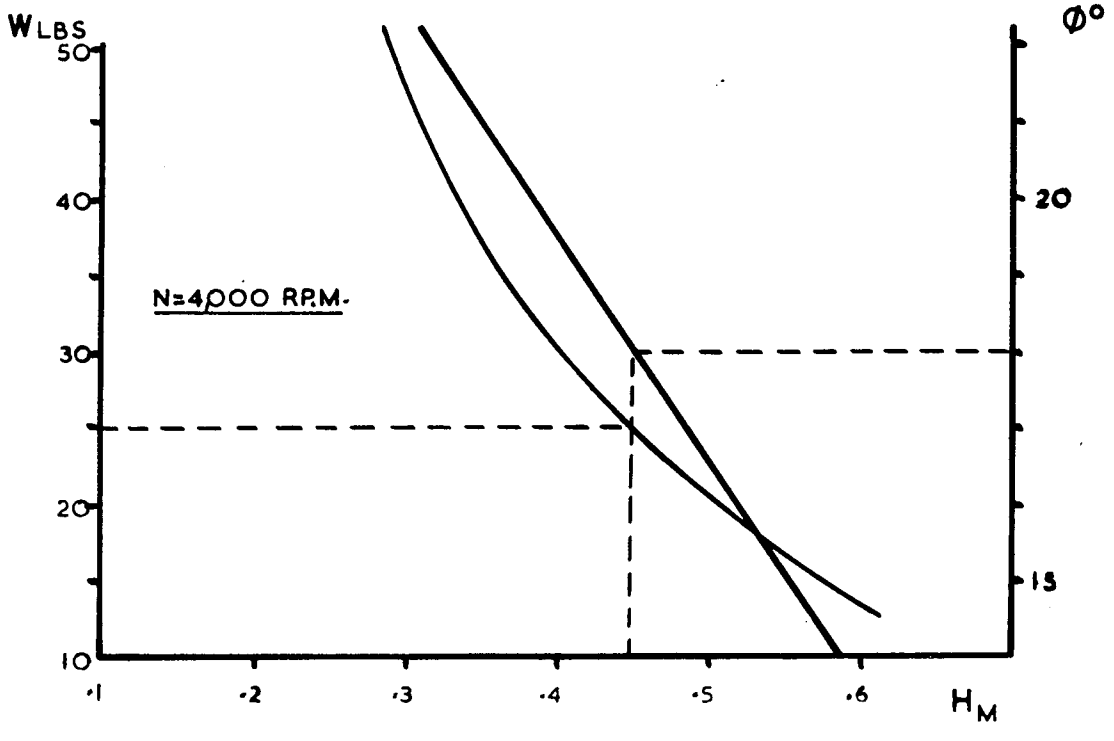

FIG. 43.B. CURVES FOR EXAMPLE. 4.

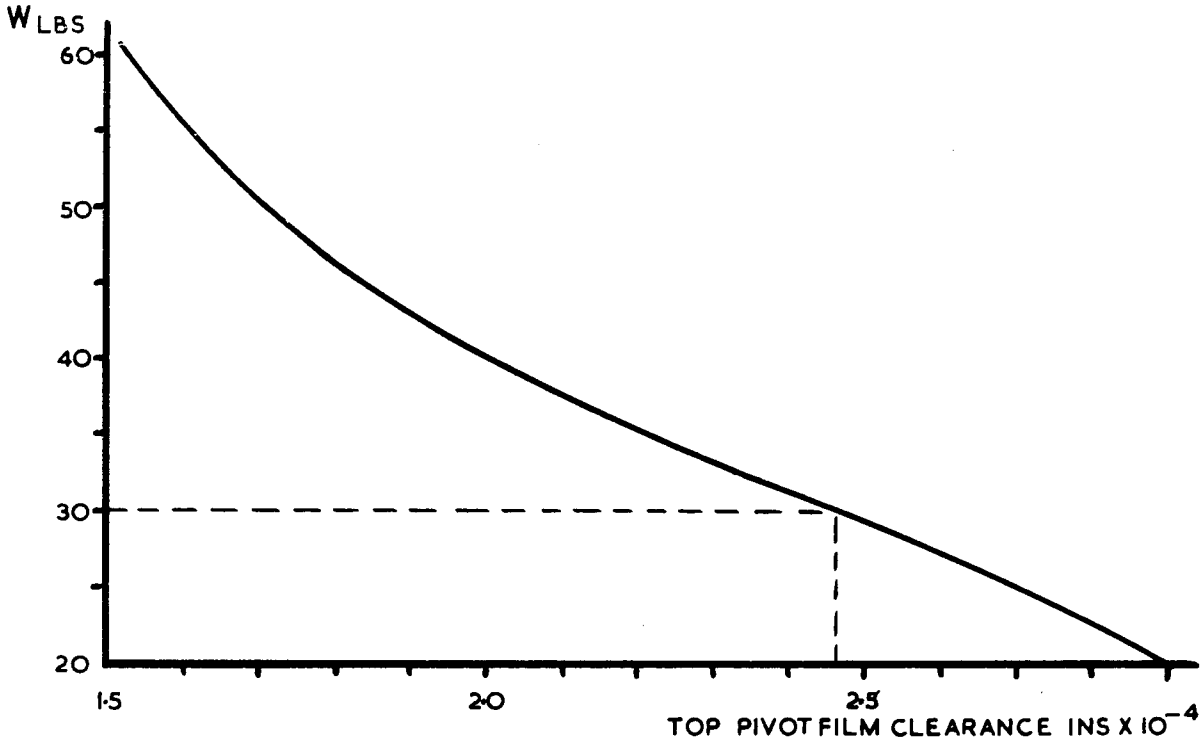

FIG.44.A.CURVE FOR EXAMPLE.5.

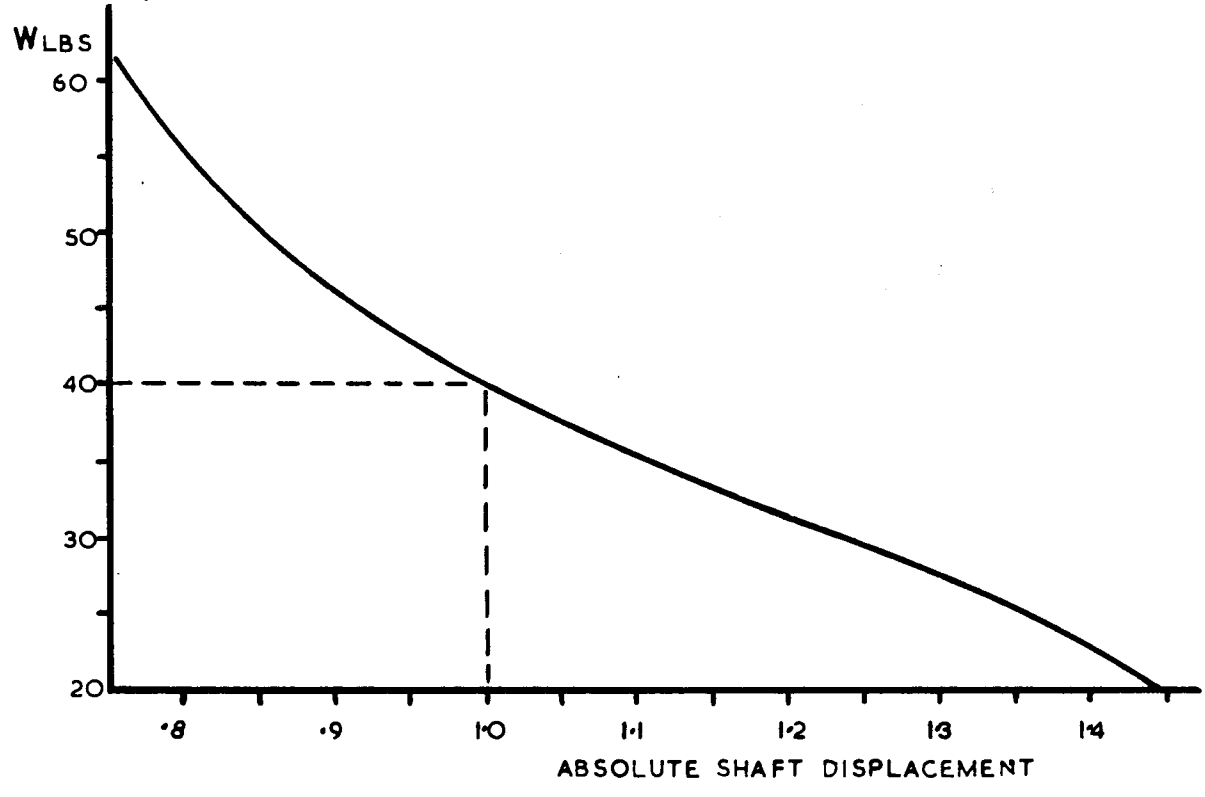

FIG.44.B.CURVE FOR EXAMPLE.5.

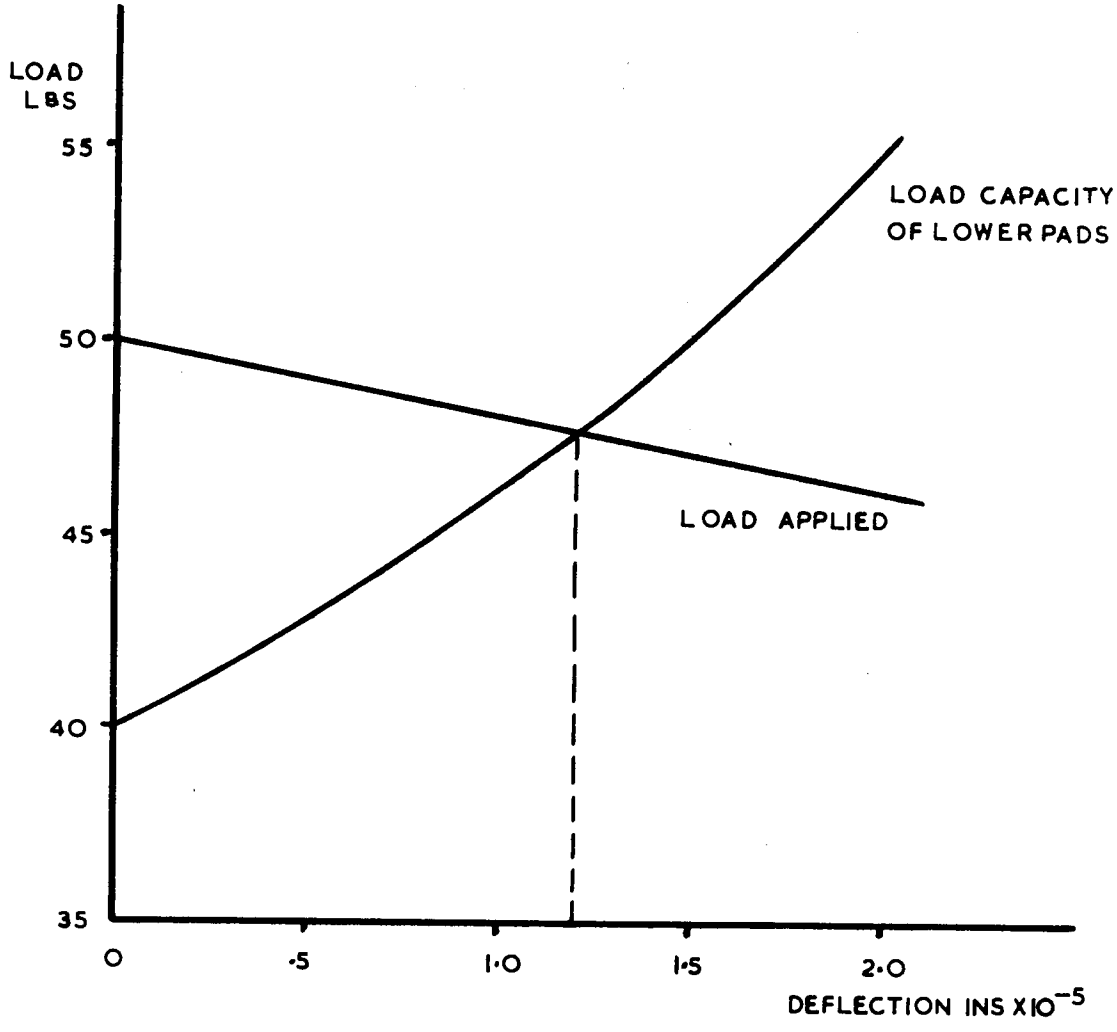

FIG. 44,C, CURVES FOR EXAMPLE.5.

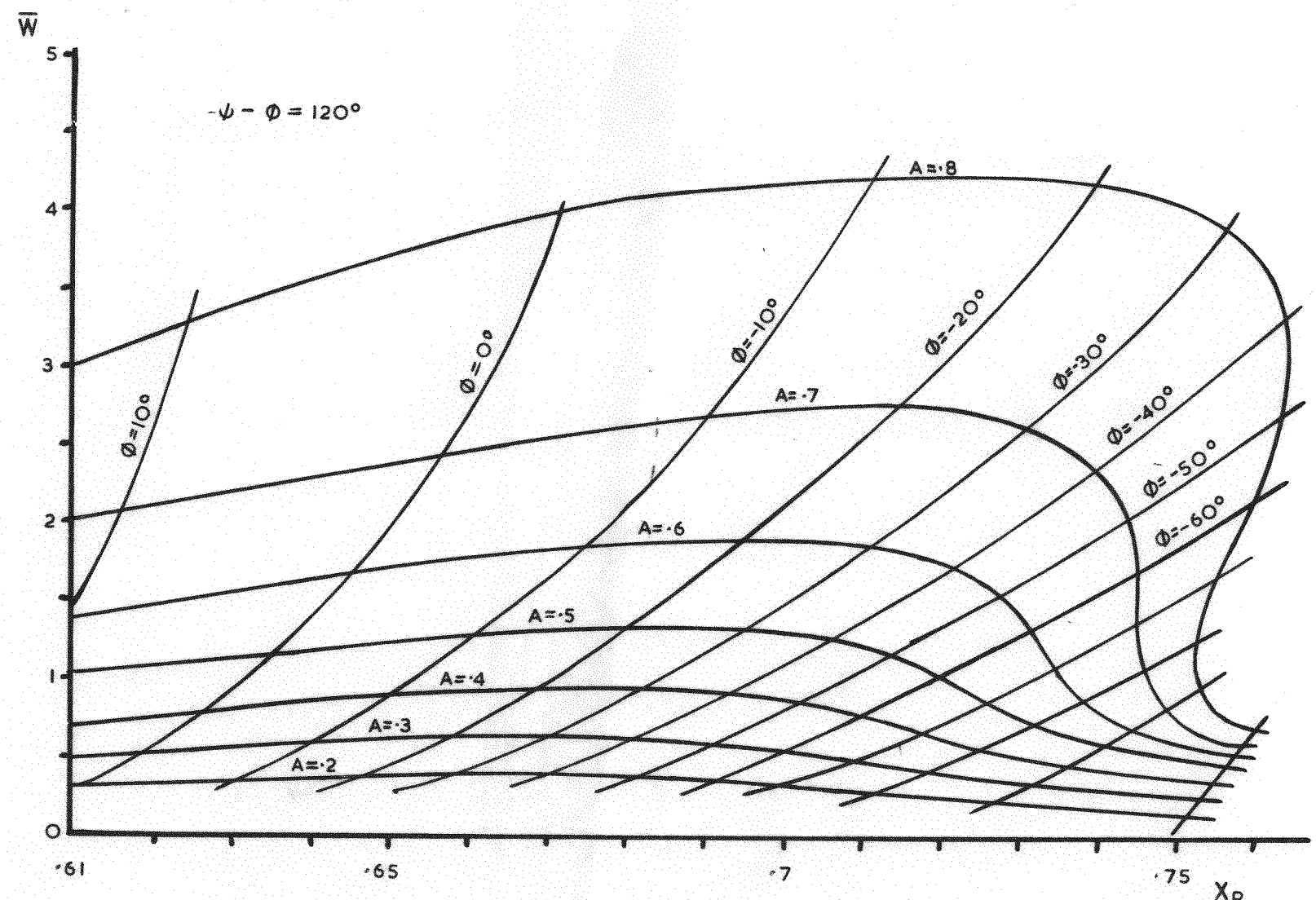

FIG. 45. $\bar{W}$ - PIVOT POSITION GRAPH FOR $\Lambda_c = \infty$

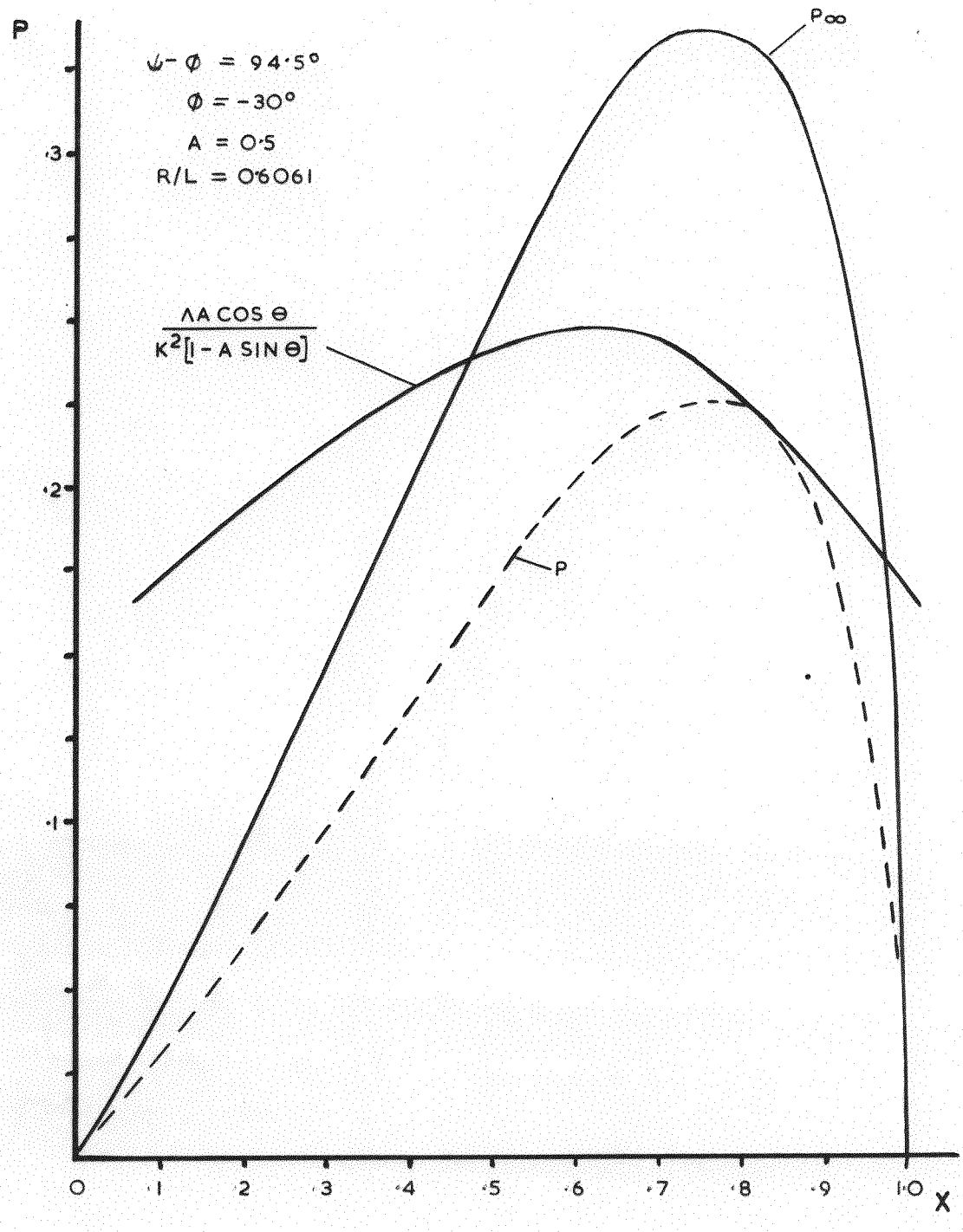

FIG.46. GRAPH TO ILLUSTRATE THE EFFECT OF C_5. – APPENDIX 2.

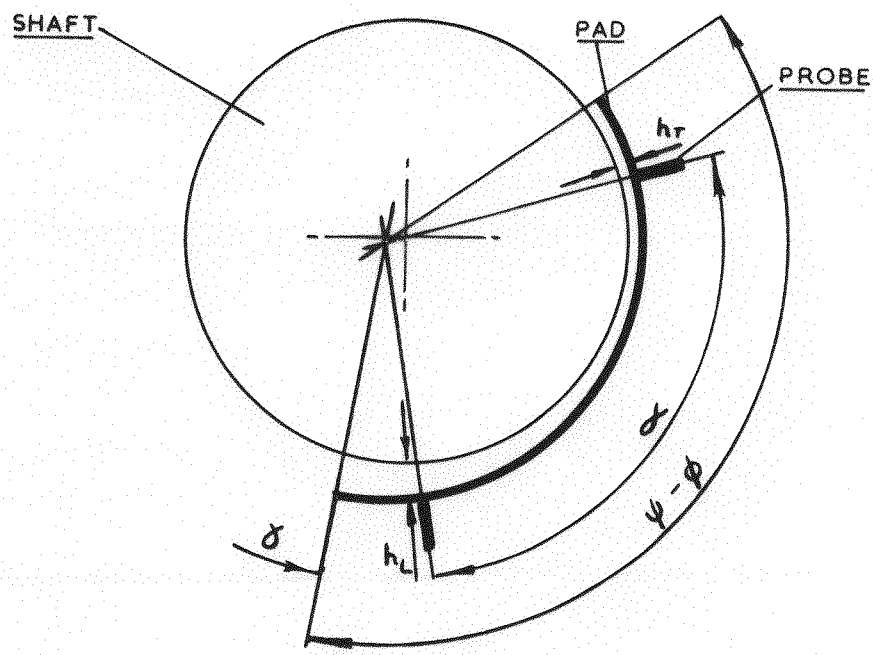

FIG. 47. CAPACITANCE PROBE POSITIONS FOR APPENDIX 4.